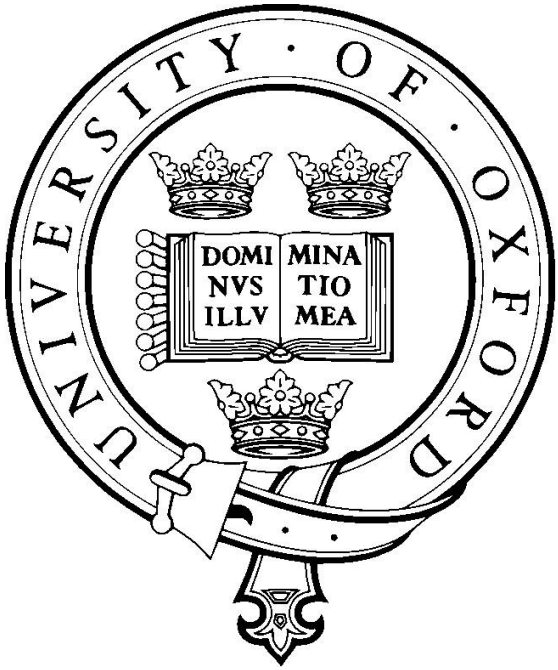
Intrinsic Properties of Double Perovskite Materials Affecting Optoelectronic Devices



Laura Schade

Balliol College

A thesis submitted for the degree of

Doctor of Philosophy

at the University of Oxford

Laura Schade, Trinity 2021

A mamma e papà,

Per aver riso quando piú ne avevo bisogno.

Acknowledgements

In the past four years I've thought about this Acknowledgements Section more than one normally would. I knew finding the right words to acknowledge all the people that supported me during this journey would have been challenging, and no words would ever be enough to express my gratitude to the ones who stayed by my side day by day.

I would like to thank Prof. Paolo Radaelli for believing in me always. Thank you for your constant support and for giving me this chance, it is because of your trust in my abilities that I am here writing this section today. Thank you for giving me a clear direction, for your availability and time, for your sincerity. Your positive and detailed feedback on my work has motivated me during this journey, and your genuine interest in science has been source of inspiration and something that I will always remember with a smile.

I would like to express my gratitude to Prof. Henry Snaith, for the fruitful conversations about my work and for helping me find the right direction for my projects. Thank you for your invaluable advice, your feedback pushed me to sharpen my thinking and was essential to formulate the right research questions.

My gratitude extends to the Engineering and Physical Sciences Research Council (EPSRC) UK and Balliol College, for funding my studies through the EPSRC scholarship EP/S004947/1 and the J. T. Hamilton award. I am particularly grateful for the ongoing economic support from Balliol over the years and especially during Covid-19 times.

To my research colleagues, for accompanying me during this journey. You all contributed to make these years unforgettable, thank you for all the fun times we had together and the memories we made. In particular I would like to thank Grey, for his pragmatic advice and for always being there when I needed him; David, for being really Canadian and supporting me always; Giulia, for teaching me all about thin film fabrication; Suhas, for his constant trust in my abilities. I am deeply grateful to Anna, the first person I spoke to on my first day as a DPhil student. Thank you for remaining a constant throughout my DPhil, becoming one of my closest friends during this journey. To Alice, thank you for being present during the toughest year of my DPhil, and for giving me precious advice.

To Mike, for being by my side during the most challenging days and for proof-reading this thesis. Thank you for your love and support.

Laura Schade, Trinity 2021

To my friends from Balliol college, Stefania and Chelsea, thank you for all the fun memories that we made and for starting and finishing this journey together.

To mum and dad, obviously I wouldn't have made it so far without you – thank you for supporting me in every possible way. You helped me realise that life is more enjoyable if not taken too seriously.

To my sister and to my wider, warm and beautiful family, thank you for being an amazing group, I couldn't have asked for better relatives. I am particularly grateful to Beppe and Giulia, for their warmth and support during these four years. Thank you, Beppe, for always being there whenever I had a mathematical doubt. To my aunt Anna, thank you for your unconditional love and belief in me, it has contributed enormously to the person that I am today. To my cousin Francesco, thank you for giving me the laptop that has seen all of the analysis present in this thesis.

Last but not least, I would like to thank my closest friends. To Marianna, for being there, always. I simply couldn't have made it without you. To Ilenia, for all of your love, warmth, and kindness, thank you for always finding the way to be close despite the distance. To Bea and Feda, for being incredible examples of determination and passion. To Poppy, for believing in "Dr. Physics" from the start.

Abstract

Hybrid halide perovskites have attracted huge attention ever since it was shown that they could be used in highly efficient photovoltaic devices produced via low-cost deposition methods. Their exceptional attributes, including high carrier mobility, an adjustable spectral absorption range, long diffusion lengths, and the simplicity and affordability of fabrication make them one of the most exceptional and market competitive optoelectronic materials for applications in photovoltaic, light emitting diodes, photodetectors, lasers and more. Despite their phenomenal properties, several crucial issues still need to be tackled before their industrial-scale use, including toxicity and instability. Whereas an ever-growing number of studies focus on improving optoelectronic properties, there is still an urgent need for a detailed understanding of these materials at a more basic level. The objective of this thesis is to understand how the intrinsic properties of halide perovskites affect the devices performances. Particular attention is given to double perovskites, as they proved to be particularly stable and they can easily be synthesized without any toxic element. Within this family, $Cs_2AgBiBr_6$ has received increasing attention as a promising candidate for optoelectronic applications. In this study, we explored the relationship between the structural and optical properties of this material. In particular, we discovered the presence of a low-temperature cubic-to-tetragonal phase transition, which influences the optical properties quite dramatically. In fact, we found that the exciton energy is mainly dependent on the new rotational degree of freedom present in the tetragonal phase. Moreover, the temperature-dependent time-resolved photoluminescence measurements revealed the presence of a carrier decay component that is only present in the tetragonal phase, which has been associated with the formation of tetragonal twin domains. $Cs_2AgBiBr_6$ is an indirect band-gap material, with a bandgap energy around ~ 2 eV. The performances of devices using this double perovskite as the absorber layer are still quite low (PCE ~ 2%). To explore the possibility of tuning the optoelectronic properties of this double perovskite, we explored the use of indium (In^{III}) alloying. The structural, optical and electronic properties of $Cs_2AgBi_{1-x}In_xBr_6$ have been explored at room and low temperature. Our structural analysis indicates that the presence of indium shrinks the lattice and shifts the transition temperature towards lower values. Moreover, we found that the structural phase transition in $Cs_2AgBiBr_6$ is very close to a tricritical point and acquires the character of a second-order phase transition when indium is substituted on the bismuth site. Our spectroscopic studies indicate that the presence of indium enlarges the band gap of the material, and at the same time strongly

enhances the photoluminescence intensity. Moreover, the photovoltaic performance improves, demonstrating a higher PCE in the presence of 10% indium. Nevertheless, the PCE is still considerably low, and it is not clear whether these materials will ever be able to perform as well as lead-halide perovskites. Our thermodynamic modelling calculations investigate the fundamental limitations of the system. Significant losses are present in the open-circuit voltage because of a shallow onset of the absorption edge, combined with significant sub-band gap absorption. For this reason, immediate attention is required to understand and mitigate the presence and role of non-radiative sites in the absorber material. Regardless of whether $Cs_2AgBiBr_6$ devices can be optimized, $Cs_2AgBiBr_6$ is an interesting model system for understanding the physics of the wider family of halide perovskites. All these compounds have closely related crystal structures and understanding structure−property relations is highly relevant for materials that are already known and for guiding the design of future compounds.

Table of contents

1. INTRODUCTION **14**

2 BACKGROUND **17**

2.1 Structural properties **17**
2.1.1 The perovskite structure 17
2.1.2 Goldschmidt's tolerance factor and octahedral tilting 17
2.1.4 Phase transitions in perovskites 19

2.2 Phase transitions: Landau theory **23**
2.2.1 Brief introduction to Landau theory 23
2.2.2 First order phase transitions 24
2.2.3 Second order phase transitions 26
2.2.4 Tricritical point 28

2.3 Mean field theory **28**
2.3.1 Critical exponents 28

2.4 Optical properties **29**
2.4.1 Absorption and emission 29
2.4.2 Urbach Energy 30
2.4.3 Defects tolerance 31
2.4.4 Charge transport and recombination 32
2.4.5 Excitons in halide perovskites 34
2.4.6 Polaronic effects in perovskites 37
2.4.7 Huang-Rhys oscillator model 38
2.5.1 Photovoltaic device characterization 39
2.5.2 Detailed balance limit 41
2.5.3 Perovskite photovoltaics 44
2.5.4 What are the challenges? 46

2.6 Double perovskites **46**

3.EXPERIMENTAL METHODS **48**

3.1 Samples synthesis **48**
3.1.1 Powders 48
3.1.2 Single crystals 49
3.1.3 Thin films 50

3.2 Diffraction **51**

3.2.1 Fundamentals 51
3.2.1 X-ray diffraction instrumentation 53
3.2.2 Neutrons diffraction 53

3.4 Heat Capacity 54

3.5 Photoluminescence spectroscopy 55
3.5.1 Steady State Photoluminescence 55
3.5.2 Time-Resolved Photoluminescence 55

3.6 UV-Vis absorption spectroscopy 57

3.7 Device preparation 57

3.8 Device characterization 58
3.8.1 Current Density-Voltage (JV) Measurements 58
3.8.2 External Quantum Efficiency 58
3.8.3 Photoluminescence Quantum Efficiency 58

4.LOW-TEMPERATURE TRANSITION IN $CS_2AGBIBR_6$ DOUBLE PEROVSKITE 60

4.1 Context and summary 60

4.2 Experimental details 61

4.3 Results 61
4.3.1 Room temperature X-ray diffraction 61
4.3.2 Temperature dependent heat capacity 64
4.3.3 Temperature dependent X-ray diffraction 66
4.3.4 Neutron powder diffraction 67
4.3.5 Tetragonal strain 69

4.4. Discussion 71

5.OPTICAL PROPERTIES OF $CS_2AGBIBR_6$ DOUBLE PEROVSKITE 72

5.1 Context and summary 72

5.2 Experimental details 74

5.3 Results 74
5.3.1 Direct gap energy and bond angles 74
5.3.2 Absorption and steady-state PL 78
5.3.3 Time-resolved photoluminescence 79
5.3.4 The nature of PL emission 82

5.4 Discussion 83

6.STRUCTURAL PROPERTIES OF $Cs_2AgBi_{1-x}In_xBr_6$ DOUBLE PEROVSKITE 86

6.1 Context and summary 86

6.2 Experimental details 87

6.3 Results 88
6.3.1 Samples and indium content 88
6.3.2 Room temperature structural characterization 89
6.3.3 Phase transition and tricritical point 94

6.4 Discussion 98

7.OPTOELECTRONIC PROPERTIES OF $Cs_2AgBi_{1-x}In_xBr_6$ AND LIMITATIONS 100

7.1 Context and summary 100

7.2 Experimental details 100

7.3 Results 101
7.3.1 Steady-state photoluminescence and absorption 101
7.3.2 Sub-bandgap absorption 103
7.3.3 $Cs_2AgBi_{1-x}In_xBr_6$ devices 104
7.3.4 The detailed balance 107
7.3.5 Photoluminescence quenching 109

7.4 Discussion 111

CONCLUSIONS AND OUTLOOK 112

REFERENCES 115

List of Abbreviations

DFT	Density Functional Theory
DMSO	Dimethyl sulfoxide
E_F	Fermi level
E_G	Bandgap energy
EQE	External Quantum Efficiency
E_{ex}	Exciton binding energy
FF	Fill Factor
FWHM	Full Width at Half Maximum
J_{MPP}	Current density generated at maximum power point
J_{SC}	Short-circuit density
PCE	Power Conversion Efficiency
PL	Photoluminescence
PLQE	Photoluminescence Quantum Efficiency
PV	Photovoltaic
TRPL	Time-resolved photoluminescence
V_{MPP}	Operating voltage of a solar cell at which maximum power output is obtained
V_{OC}	Open-circuit voltage
XRD	X-ray Diffraction
MHP	Metal halide perovskites

1. Introduction

Energy demand has been one of the driving forces for the past century industrial revolution, and keeps on growing at a steady rate. Humans have used fossil fuels as primary source of energy production because of their low price and high energy density. Non-renewable fossil fuels emit carbon dioxide (CO_2), a common heat trapping greenhouse gas. If the concentration of greenhouse gases in the atmosphere increases, there can be disastrous consequences for the ecosystem of our planet. According to NASA data, 2020 was the warmest year since 1880, continuing a long-term trend of rising global temperatures [1]. The earth's climate has changed throughout history, in the last 650,000 years there have been seven cycles of glacial advance and retreat, attributed to very small variations in the earth's orbit. Nevertheless, for millennia, atmospheric carbon dioxide had never been higher than now, and the current warming trend is extremely likely to be the result of human activity such as burning of hydrocarbon fuels, deforestation, and various industrial processes [2]. The increase rate of the past few decades is unprecedented [3]. This temperature rise may not be noticeable in our everyday lives, but it significantly impacts weather patterns. In recent years, we started to experience melting polar ice caps and glaciers [4], rising sea levels [5], dying coral reefs [6] and extreme weather conditions [7]. Arguably, we have never influenced the environment of our planet more.

To meet the global energy demand and to reduce the CO_2 emissions, an energy revolution will need to take place. Transition from an exhaustible fossil fuel energy era to renewable sources will have to happen, and it is imperative that this change happens sooner rather than later to mitigate the impact of global warming. Among the various solutions that are being taken in consideration, solar radiation represents a vast source of clean, renewable energy [8]. The limitless amount of available energy suggests that solar prices can remain low as demand rises. Assuming that the sun shines 120,000 TW of radiation on the surface of the earth, we can estimate that covering 0.1% of the land on earth with 17% efficient solar cells would produce more than 20 TW of power, which exceeds today's entire world energy consumption [9], [10]. Many materials that are used for photovoltaic modules are abundant and produced in high volume. At the moment, almost all the electricity generated by photovoltaic effect is produced by solar cells based on crystalline silicon. Silicon is an abundant, non-toxic and stable material, with a 1.11 eV band gap at 300K and long charge-carrier lifetimes [11]. Although silicon cells currently dominate the market, they face competition from technologies based on thin-film absorbers [12]. Thin-film materials, and

particularly organic-inorganic perovskite hybrids, have been recognised as very promising candidates to make a significant contribution to the solar technology market. Perovskite materials present almost ideal optoelectronic properties for photovoltaic applications: made with earth-abundant chemicals, they are cheap to produce, simple to process, strongly absorbing, and they have tuneable bandgaps and relatively long diffusion lengths [12]. The PCE of perovskite-based solar cells has rapidly improved within just a few years from the discovery of their potentiality as a photovoltaic material in 2009 from 2.8% [13] to the present 25.5% [14]. Few solar materials have ever improved so much and none have done it so fast. However, in the case of the most commonly studied lead-halide perovskites, two issues still hinder large-scale commercial applications: their instability towards heat, moisture, and other environmental factors [15] and the presence of the toxic element Pb [16]-[17]. The use of lead is highly regulated and restricted in many countries, due to the hazard it poses to the environment and also to its high toxicity level. Substituting lead for other elements proves to be a challenge as Pb is considerably cheaper than its alternatives, is abundant and has a low GWP (Global Warming Potential) [16]. A promising candidate has been identified to be Sn [18], as it has a similar electronic configuration and the presence of a lone pair of electrons in the *s* orbital. However, Sn^{II} easily oxidises to Sn^{IV} due to the instability of its high-energy $5s^2$ orbitals [19]. For this reason, Sn-based perovskites react quickly with air and moisture, deteriorating considerably the photovoltaic efficiency [20].

Double perovskites with formula $A_2BB'B_6$ have been recently proposed as lead-free, highly stable alternatives [21]. Within this class of materials, the double perovskite $Cs_2AgBiBr_6$ has caught the attention of researchers due to its favourable properties. In fact, it has been reported to be highly stable, with a long charge carrier lifetime and low effective masses [21]–[24]. Moreover, it is one of the very few materials in the perovskite class, aside from lead halide perovskites, that showed a reliable, even if still low, device performance [25]. For $Cs_2AgBiBr_6$, with a reported band gap in the range 1.8 – 2.2 eV [23], [26], [27], the thermodynamic limit for the performance under the Schockley-Queisser assumptions [28] is in the range 18.7% - 27.2%. The higher reported band gap in this range (2.2 eV) is non-ideal for application in PV cells, being too wide for optimum use as the top cell in both tandem and even triple-junction solar cells, while the reported lower limit (1.8 eV) indicates that this material might be of use as top layer in multi junction solar cells [29]. Measurements confirming the precise band-gap of this novel material will help understand its best use, while strategies used to move the absorption onset towards lower energies are likely to lead to enhanced performance and utility.

It is clear that further improvements have to be made towards the optimization of devices, but more urgent is the need to understand this material at a fundamental level. In this thesis, we investigate the properties of the $Cs_2AgBiBr_6$ double perovskite and of the alloyed $Cs_2AgBi_{1-x}In_xBr_6$, with a focus on the structural and optoelectronic features.

Chapter 2 introduces the topic and discusses the background and theory. The properties of metal-halide perovskites are briefly described, giving context to the importance of the double-perovskite compositions studied in this thesis. The main techniques used to investigate the material properties are briefly described in Chapter 3. These include X-ray diffraction, photoluminescence spectroscopies and device characterization. Chapter 4 is focussed on the investigation of the structural properties of $Cs_2AgBiBr_6$ double perovskite. We discovered the presence of a low-temperature phase transition at $T_s \approx 122$ K, from a cubic phase (space group $Fm\bar{3}m$) to a tetragonal phase (space group I4/m). This phase transition has been characterized with the use of X-ray and neutron diffraction, as well as with heat capacity measurements. In Chapter 5, we outline the influence of this phase transition on the optical properties of this material. We discover that the exciton energy at the direct band gap is linearly proportional to the tetragonal strain, which arises in the low-temperature phase. Hence, the direct gap energy is mainly dependent on the additional rotational degree of freedom appearing in the tetragonal phase. Moreover, we discovered the presence of three different decay paths in the time-resolved photoluminescence data. One of these appears only in the tetragonal phase, which might be due to the presence of defects at the twinning boundaries.

Chapter 6 investigates the structural properties of $Cs_2AgBi_{1-x}In_xBr_6$ double perovskite. We find that the phase transition in the neat $Cs_2AgBiBr_6$ is very close to a tricritical point and moves to a second-order transition when indium is introduced on the bismuth site. The influence of indium on the optical properties of the neat perovskite material is studied in Chapter 7. We find that a small percentage of indium causes a strong enhancement in the photoluminescence intensity emission. Nevertheless, when these materials are employed as absorbers in n-i-p solar cells, device performance is still low in comparison with their lead-halide counterparts. For this reason, in the final sections of this Chapter, we investigate the origin of these losses through the use of thermodynamic modelling.

2. Background

This Chapter summarizes the structural, optical and electronic properties of the most commonly studied halide perovskites, providing a concise overview of fundamental concepts that are utilized throughout the work in this thesis.

2.1 Structural properties

2.1.1 The perovskite structure

The mineral of calcium titanium oxide $CaTiO_3$, the first perovskite material investigated, was discovered by the Prussian mineralogist Gustav Rose in 1839 in the Urals mountains of Russia. The structure was later characterized by the Russian mineralogist Lev A. Perovski, from which it derived its name [30]. The family of perovskite materials adopt the chemical formula ABX_3, where A and B are cations of dissimilar sizes (R_A>R_B), and X are anions, typically oxygen, halogens, or alkali metals.

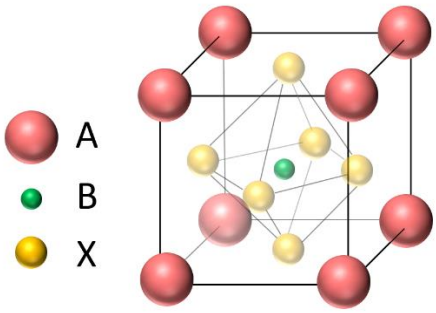


Figure 2.1 Perovskite crystal structure

The ideal cubic structure has the 'B' cation in 6-fold coordination, surrounded by an octahedron of anions, and the 'A' cation in 12-fold cub-octahedral coordination. The structure is pictured as a three-dimensional network of regular corner-linked BX_6 octahedral, as shown Figure 2.1. In this cubic unit cell, the 'A' atom sits at cube corner positions (0,0,0), the 'B' atom sits at body centred positions (1/2,1/2,1/2), and the 'X' atom sits at face centred positions (1/2,1/2,0).

2.1.2 Goldschmidt's tolerance factor and octahedral tilting

The relative ion size requirements for stability of the cubic structure are quite strict, so even a slight distortion can produce several lower-symmetry structures, in which the coordination numbers of A cations, B cations or both are reduced. Deviations from cubic symmetry can

result from several factors, the first being size effect. For this reason, a geometric parameter was developed by Goldschmidt [31] and called tolerance factor *t*:

$$t = \frac{R_A + R_X}{\sqrt{2}(R_B + R_X)} \qquad (2.1)$$

where R_A, R_B, and R_X are the ionic radii of the corresponding ions. Geometrically, for an ideal perovskite, the ratio of d(A-X), the bond length of A-X bond, to d(B-X), the bond length of B-X bond, is $\sqrt{2}$:1. Thus, if the bond length is roughly assumed to be the sum of two ionic radii, the *t* value of an ideal perovskite should be equal to 1. Therefore, this parameter is used to evaluate the structural formability and stability and presents a guideline for tuning of radii sizes relative to cubic symmetry. In general, perovskite structures occur for 0.85 < t < 1.11 for halide perovskites [32]. Cubic symmetry provides optimum electronic properties due to a high degree of ionic bonding. Mismatch of crystal components outside of the ideal tolerance range results in octahedral tilting that can affect electronic properties. Figure shows as an example the structural tilting in $AGaO_3$ oxide perovskite, which results in tetragonal (panel b) and orthorhombic (panel c) structures [33]. If the tolerance factor t<1 usually the B cations have a large size and the A cation is too small, the perovskite cell gets deformed and the symmetry is lowered. If t>1, as a result of a large A or small B, the BX_6 octahedra are unable to maintain connectivity of the lattice around the A cation, and the ions adopt lower-dimensional or hexagonal perovskite-like structures.

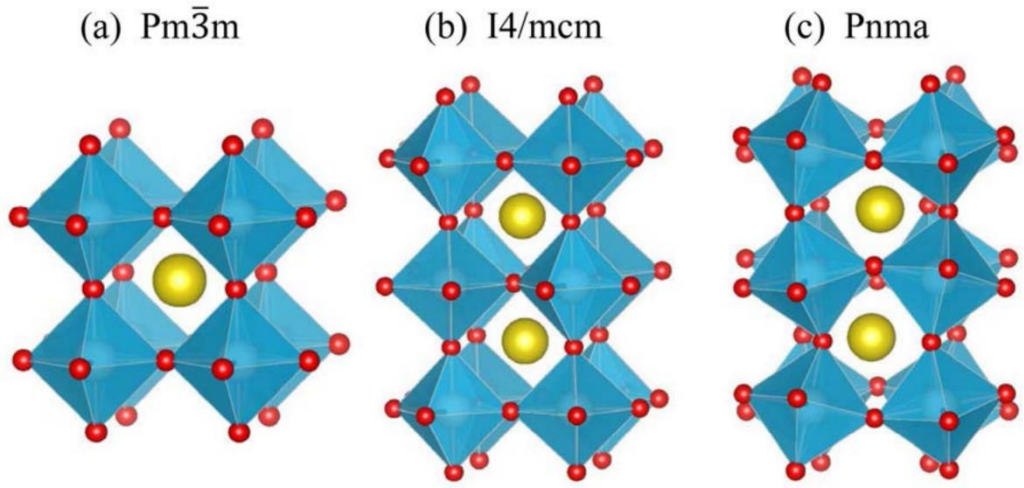


Figure 2.2 The detailed structure of $AGaO_3$ perovskite with various octahedral tilting, (a) Pm$\bar{3}$m cubic without any tilting, (b) I4/mcm tetragonal with $a^0a^0c^-$ tilting, (c) Pnma orthorhombic with $a^-a^-c^+$ tilting. Reproduced with permission from [33].

Goldschmidt's tolerance factor t is not by itself sufficient to predict the formation, or not, of the perovskite structure. Another dimensionless factor that helps predicting the perovskite formability is the octahedral factor μ:

$$\mu = \frac{R_B}{R_X} \tag{2.2}$$

For a perovskite structure to form at all, the B-site cation must be sufficiently large to coordinate octahedrally with the X anions. Goldschmidt postulated that perovskites arrange so that "the number of anions surrounding a cation tends to be as large as possible, subject to the condition that all anions touch the cation" [34]. With basic geometric considerations, the octahedral factor is bound to be $\mu \geq 0.41$ to enable the formation of a perovskite structure. If the B cation is too small the octahedra will be unstable due to the X anions approaching too closely to each other.

There are various perovskite distortions that can happen simultaneously: tilts of the BO_6 octahedral units, A-site cation displacement, distortion of the octahedra and the B-site cation displacement within the octahedra. The majority of distorted perovskites can be derived from the cubic archetype by the rigid tilting of the octahedra around one or more of their symmetry axes, maintaining both the regularity of the octahedra, and their corner connectivity. Such tilting allows greater flexibility in the coordination of the 'A' cation, while leaving the environment of the 'B' cation unchanged. A convenient notation has been created by Glazer [35] in 1972. He described the octahedral tilting in terms of component tilts around the cubic axes of the aristotype. A tilt around one of these axes constrains the tilts in directions perpendicular to this axis, but the successive octahedra along the axis might be tilted in either the same or opposite sense. The notation consists in using symbols $a^{\#}b^{\#}c^{\#}$, in which the letters refer to tilts around the [100], [010] and [001] directions of the aristotype respectively, and the superscript # would be either 0, + or – to indicate no tilt around an axis, or tilts of successive octahedra in the same or opposite sense. As examples, the ideal cubic perovskite, here called aristotype, is $a^0b^0c^0$, the tetragonal perovskite in Figure 2.2b is $a^0a^0c^-$, and the orthorhombic perovskite in Figure 2.2c is $a^-a^-c^+$.

2.1.4 Phase transitions in perovskites

Although there are different kinds of phase transitions, in this thesis we will focus our attention primarily on the basic concepts of structural phase transitions in perovskites, and we will only briefly introduce concepts which are closely related to this research. The structures in the ABX_3 perovskite family have long attracted interest, due to the effects that

structural variations have on important physical properties. The ABO_3 perovskites have been associated with superconductivity, dielectric properties, ferroelectricity and more [36]. As previously stated, the ideal simple perovskite structure is cubic, with space group $Pm\bar{3}m$, and with a close packed arrangement of corner-sharing BO_6 octahedra. Varying the size ratio of the A and B cations leads to distorted phases with lower symmetry. In addition to changes in composition, distorted phases can be induced by variations in external parameters, like temperature [37] or pressure [38].

In most cases a symmetry relationship exists between the two phases of a phase transition, i.e. some of the symmetry operations of the high-symmetry phase are not symmetry operations of the low symmetry one. Therefore, one of the space groups is a subgroup of the other. The breaking of the symmetry operations of the high symmetry phase is an essential characteristic of most phase transitions. Relative to an undistorted cubic perovskite ($Pm\bar{3}m$), Figure 2.3 shows the 15 different space groups of tilted perovskite structures predicted using group theory by Howard and Stokes [39]. Perovskites tend to exhibit analogous phase behaviour. For instance, the prototypical $CaTiO_3$ perovskite upon heating exhibits the phase sequence $Pnma \nrightarrow I4/mcm \nrightarrow Pm\bar{3}m$, and this behaviour is identical, even if at different transition temperatures, for strontium zirconate ($SrZrO_3$). One of the most studied perovskites for photovoltaic applications, $MAPbI_3$, also undergoes phase transitions between the same space groups, as illustrated in Figure 2.4, going from a cubic structure at high temperature, to a tetragonal one upon cooling, and then to an orthorhombic structure upon further cooling [40].

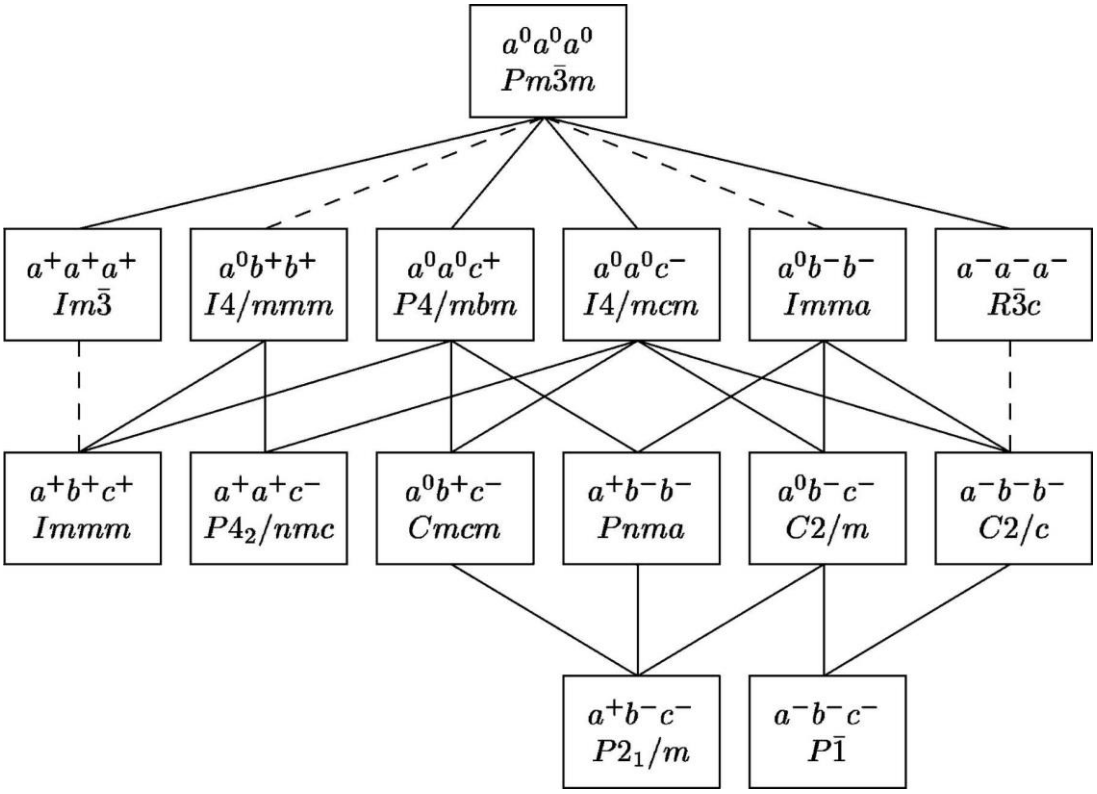


Figure 2.3 A schematic diagram indicating the group-subgroup relationships among the 15 space groups tabulated by Howard and Strokes (1998). Reproduced with permission [39].

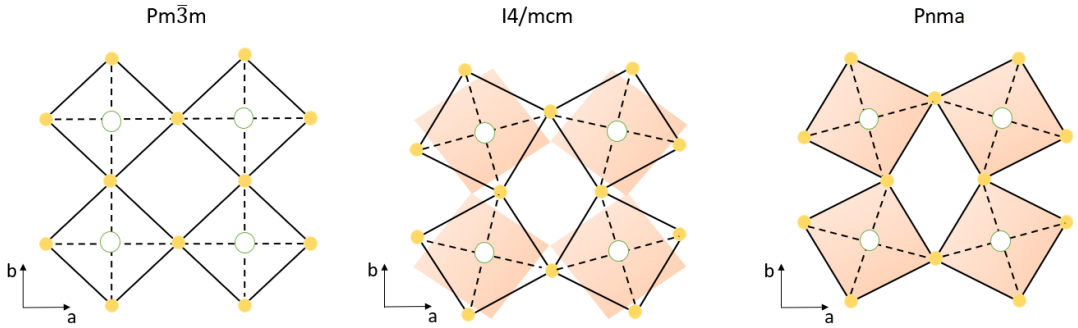


Figure 2.4 The crystal structures adopted by $MAPbI_3$. Adapted from [40].

As temperature induces phase transitions, pressure can also trigger changes in structure. An increase in pressure can lead to compression of the BX_6 octahedra and/or change in octahedral tilting. Another common way to tune the octahedral tilting in a perovskite structure is through varying the size of the atoms, through chemical substitution, which can be considered a form of chemical pressure [41].

This thesis is focused on double perovskites, $A_2BB'X_6$, which are associated with rock-salt ordering. The subgroup of Pm$\bar{3}$m that leaves the ordered double perovskite unchanged is Fm$\bar{3}$m. An analysis of the structures occurring in double perovskites as a result of the cation

ordering in combination with the corner-linked tilting of the BX_6 (or $B'X_6$) octahedral units has been presented by Howard et. al. in 2003 [42]. The group-subgroup relationships found are summarized in Figure 2.5.

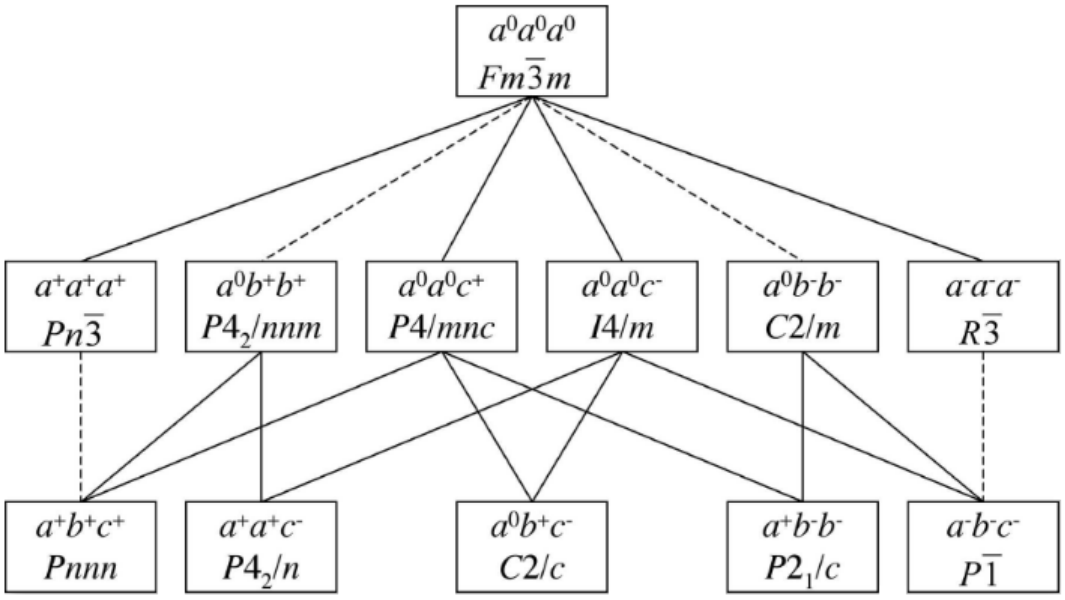


Figure 2.5 Schematic diagram indicating the group-subgroup relationships from the $Fm\bar{3}m$ space group. A dashed line joining a group to its subgroup indicates that the corresponding phase transition is required by Landau theory to be first order. Reproduced with permission from [42].

Phase transitions are divided into two categories by the Ehrenfest classification [43]. He classified phase transitions based on the behaviour of the thermodynamic free energy as a function of other thermodynamic variables. Under this scheme, phase transitions are labelled by the lowest derivative of the free energy that is discontinuous at the transition. First order phase transitions display a discontinuity in the first derivative of the free energy with respect to some thermodynamic variable, while second order phase transitions are continuous in the first derivative (the order parameter, which is the first derivative of the free energy with respect to the external field, is continuous across the transition) but exhibit a discontinuity in the second order derivative of the free energy [44]. The derivative, however, is not enough to explain the full difference between a first and second order phase transition. The Ehrenfest classification may not work for all transitions, and there are different classification systems which can be used.

2.2 Phase transitions: Landau theory

2.2.1 Brief introduction to Landau theory

A different approach to phase transitions was formulated by Landau in 1937 [45]. In order for two crystalline structures to be related by a second-order phase transition, following from the continuity of the structure change, the space groups of the structures must be in a relation of a group and a subgroup. Moreover, the distortion should correspond to a single irreducible representation of the space group of high symmetry.

A temperature-driven phase transition in this scheme is characterized by an order parameter (η), which can characterize an atomic displacement, electric polarization, magnetization, etc. The order parameter is non-zero at low temperature and becomes zero above a certain critical temperature T_c, which is called transition temperature. A transition will be a second order (continuous) phase transition if its order parameter decreases continuously to zero as the high-symmetry phase is approached. A transition is said to be a first order (discontinuous) phase transition if the magnitude of the order parameter changes suddenly at T_c. In Landau theory, the free energy must be invariant with respect to the high-symmetry space group and the Landau free energy can be expanded as a power series of order parameters near the transition temperature. The Landau free energy must be analytic and must obey the symmetry of the Hamiltonian. Given these two conditions one can write, in the vicinity of the critical temperature T_c, a phenomenological expression for the free energy as a Taylor expansion around zero in the order parameter (which is considered to be small near the transition temperature):

$$F(P,T,\eta) = F_0(P,T) + a\eta + b\eta^2 + c\eta^3 + \frac{1}{2}d\eta^4 + e\eta^5 + \frac{1}{3}f\eta^6 + O(\eta^7) \qquad (2.3)$$

The coefficients in this expansion may be temperature and pressure dependent. The conditions for the minimization of this free energy F(P,T,η) with respect to η determine the fundamental restrictions on η, i.e. the possible change of symmetry. If the minimum occurs at η=0, then no distortion occurs, and the phase is expected to retain the original space group symmetry. At some particular temperature and pressure, the minimum of F may occur at some non-zero value of the order parameter η. In this case, a phase transition occurs due to a distortion. In case of a continuous phase transition (η goes to its non-zero value continuously), Landau theory only allows certain isotropy subgroups as possible candidates

for the lower-symmetry phase. However, when discontinuous transitions are considered, any of the isotropy subgroups of the original space group are allowed symmetry phases.

For simplicity, let's consider a one-dimensional order parameter. It is a reasonable approximation to consider the series to fourth order in the order parameter, as long as η is small. Let's also suppose, for simplicity, that we have a symmetry which gives η → - η, then the system can only have even powers of η. In this case the change in Landau free energy becomes:

$$F(P,T,\eta) - F_0(P,T) = b\eta^2 + \frac{1}{2}d\eta^4 + \frac{1}{3}f\eta^6 \tag{2.4}$$

where b is assumed to be strongly temperature dependent, and both d and f are assumed to be constant for $T \sim T_c$. We can now analyse this power series to see under what conditions there is a minimum which moves around as we change the temperature. If we assume that b and d are positive, then all the terms increase the Landau free energy for all values of η, so the minimum occurs when $\eta = 0$. This describes the high temperature phase. In the low temperature phase, one of the parameters must be negative and large enough in comparison with the other terms. For the system to be thermodynamically stable, the coefficient of the highest even power of the order parameter must be positive, so one can assume f>0. As b is temperature dependent in the Landau's assumption, we can take $b=b_0(T-T_c)$ with $b_0>0$. Then the change in Landau free energy becomes:

$$F(P,T,\eta) - F_0(P,T) = b_0(T-T_c)\eta^2 + \frac{1}{2}d\eta^4 + \frac{1}{3}f\eta^6 \tag{2.5}$$

We can have two main situations based on the sign of the parameter d:

- d>0: second order (continuous) phase transition
- d<0: first order (discontinuous) phase transition

2.2.2 First order phase transitions

The transition is first order if d<0. The sixth power term is important in our calculation to restrain the Landau energy from going to minus infinity. In this case, minimizing F we obtain:

$$\frac{\partial F}{\partial \eta} = \eta[2b_0(T-T_c) + 2d\eta^2 + 2f\eta^4] = 0 \tag{2.6}$$

$$\frac{\partial^2 F}{\partial \eta^2} = 2b_0(T-T_c) + 6d\eta^2 + 10f\eta^4 > 0 \tag{2.7}$$

Calculating when $\frac{\partial F}{\partial \eta} = 0$ will provide the values of the order parameters that minimize the free energy. From equation 2.6 one solution clearly is $\eta = 0$. The other part of the equation in squared brackets results in other 4 solutions:

$$\eta^2 = 0, \pm\frac{-d \pm \sqrt{d^2 - 4b_0 f(T - T_c)}}{2f} \tag{2.8}$$

Of the five solutions found for η, at most three are real and stable (two of the solutions are maxima so they don't contribute). The real and stable solution are:

$$\eta = \pm\sqrt{\frac{-d + \sqrt{d^2 - 4b_0 f(T - T_c)}}{2f}} \qquad \text{for } T < T_c \tag{2.9}$$

$$\eta = 0, \pm\sqrt{\frac{-d + \sqrt{d^2 - 4b_0 f(T - T_c)}}{2f}} \quad \text{for } T_c < T < T_1 \tag{2.10}$$

$$\eta = 0 \qquad \text{for } T > T_1 \tag{2.11}$$

where T_1 is the temperature where the two non-zero solutions merge into an inflection point (i.e. correspond to the secondary minima in the non-equilibrium curve in Figure 2.6):

$$T_1 = T_c + \frac{1}{4}\frac{d^2}{b_0 f} \tag{2.12}$$

If we substitute the expressions found for the order parameter into the Landau free energy (equation 2.5), we can find two branches of solutions ($F=F_0$ for $T>T_c$ and another solution for $T<T_1$). Apart from T_c and T_1, there is another temperature which plays an important role, which appears when the free energies of these two phases are equal. With some algebraic calculation, one can find: $T_0 = T_c + \frac{3}{16}\frac{d^2}{b_0 f}$. We can visualize a first-order phase transition in Figure 2.6. The order parameter as a function of temperature is illustrated in Figure 2.7.

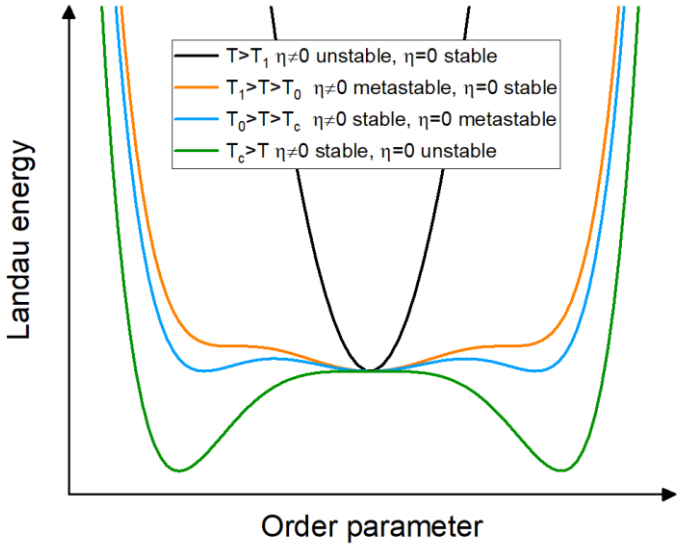


Figure 2.6 Landau free energy for different temperature ranges in a first-order phase transition.

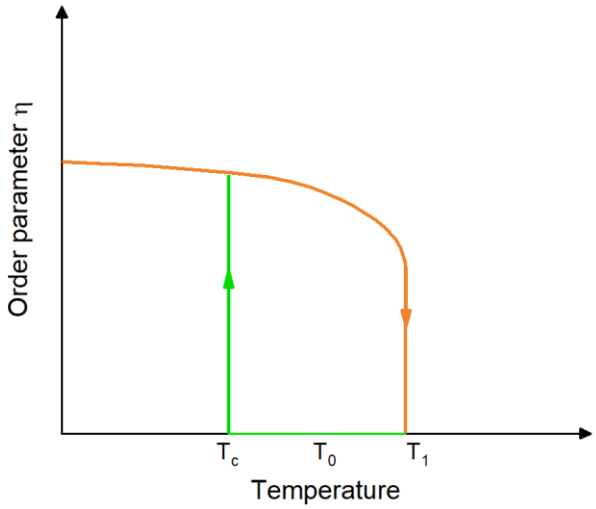


Figure 2.7 Order parameter as a function of temperature in the case of a first-order phase transition.

2.2.3 Second order phase transitions

The transition is second order if d>0. In this case, let's consider a simplified case in which we neglect the sixth power term from our calculation. In this case we have:

$$\varphi(P,T,\eta) - \varphi_0(P,T) = b_0(T - T_c)\eta^2 + \frac{1}{2}d\eta^4 \qquad (2.13)$$

The equations minimizing 2.13 are:

$$\frac{\partial\varphi}{\partial\eta} = 2\eta(b_0(T - T_c) + d\eta^2) = 0 \qquad (2.14)$$

$$\frac{\partial^2 \varphi}{\partial \eta^2} = 2b_0(T - T_c) + 6d\eta^2 > 0 \qquad (2.15)$$

Solution of equation 2.14 is:

$$\eta = 0 \text{ for } T > T_c, \text{ and } \eta = \sqrt{\frac{b_0(T_c - T)}{2d}} \text{ for } T < T_c \qquad (2.16)$$

The first solution represents the low temperature phase ($T<T_c$) and the second one corresponds to the high temperature phase ($T>T_c$), where $T=T_c$ is the critical temperature (transition temperature). This case is illustrated in Figure 2.8. The behaviour of the order parameter as a function of temperature is illustrated in Figure 2.9.

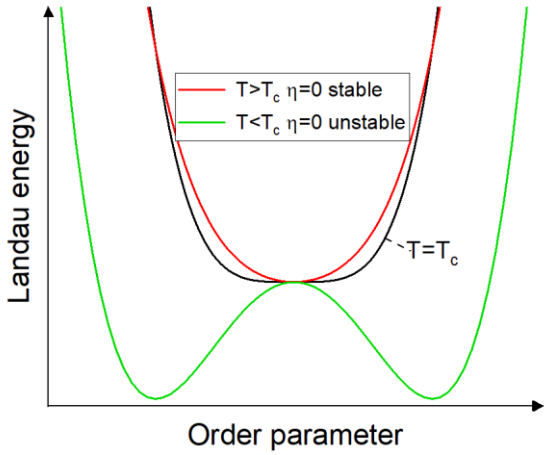


Figure 2.8 Landau free energy for different temperature ranges in a second-order phase transition.

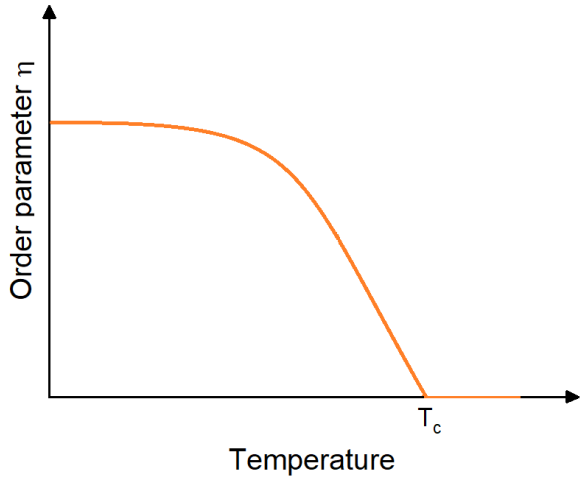


Figure 2.9 Order parameter as a function of temperature in a second-order phase transition.

2.2.4 Tricritical point

A tricritical point is a point where the lines of the first order and second order transitions cross. As we have seen in the previous sub-sections, Equation 2.5 represents a first order phase transition if d<0, and a second order phase transition if d>0. When d=0, we are at the tricritical point. If d is dependent by an external parameter (e.g. alloying, temperature, pressure…), the transition can become tricritical for certain values of this parameter, where d = d(parameter).

In Chapter 3, we assign the low temperature phase transition in $Cs_2AgBiBr_6$ to be second order, or nearly first order. We will then deduce in Chapter 5 that this transition is indeed close to a tricritical point.

2.3 Mean field theory

The detailed description of the mean field theory goes behind the interest of this thesis, and we will only briefly mention the main concepts that will help the reader throughout this text.

2.3.1 Critical exponents

Critical exponents describe the behaviour of physical quantities near continuous phase transitions [46]. We can suppose here for simplicity that the control parameter that drives the phase transition is the temperature. Being interested in the behaviour close to the critical point, we define a reduced temperature: $t = (T-T_c)/T_c$ so that t=0 implies $T=T_c$. If f(t) is a generic function of t, a critical exponent μ associated to this function is defined as:

$$f(t) \sim |t|^{\mu} \quad for\ t \approx 0 \tag{2.17}$$

Thermodynamic parameters have specific critical exponents, for example the specific heat:

$$C_V \sim |t|^{-\alpha} \tag{2.18}$$

And the order parameter of the system:

$$\eta \sim (-t)^{\beta} \tag{2.19}$$

The importance of critical exponents lies on the fact that they are universal, therefore their value does not depend on the details of the system chosen, but only on some of its general features.

2.4 Optical properties

We do not discuss the fundamentals of semiconductors theory, as it is assumed that most readers would be already conversant with these topics.

2.4.1 Absorption and emission

Metal halide perovskites (MHPs) have been used as absorber materials in photovoltaic devices because of their properties, delivering outstanding device PCEs [14]. MHPs possess high absorption coefficients ($\sim 10^5$ cm^{-1} [47]) across the visible spectrum [48], their absorption spectra have a clear onset [49], [50], and their composition can be varied to achieve the optimal bandgap for single- or multi-junction solar cell applications.

In a semiconductor, electrons at the top of the valence band may be excited into the conduction band when absorbing a photon, leaving a hole (electron vacancy) in the valence band. The emission of an electron, after the excitation of a photon, can only occur if the energy of the photon is equal or greater than the band gap of the material. This means that for each material there is a threshold frequency at which light absorption is possible:

$$h\nu \geq E_g \tag{2.20}$$

Otherwise, visible light simply passes through the material, and the photon cannot transfer its energy to the electron or the lattice. The excited electron relaxes down towards the minima of the conduction band by losing its energy through carrier-carrier and carrier-phonon scattering [51]. This thermalisation process, which occurs in the femtosecond regime, represents a loss in energy:

$$E_{th,loss} = h\nu - E_g \tag{2.21}$$

The electron in the conduction band will be able to recombine with a hole and release its energy by emitting a photon (photoluminescence) or in the form of lattice vibration. This process is slower than that of thermalisation, in fact it occurs in the microsecond regime. If the semiconductor is used as absorber layer in a solar cell, then the electron in the conduction band is transported to the electrode via drift or diffusion currents. Inter-band absorption is strongly dependent on the band structure of the solid, and on the direct or indirect character of the band gap.

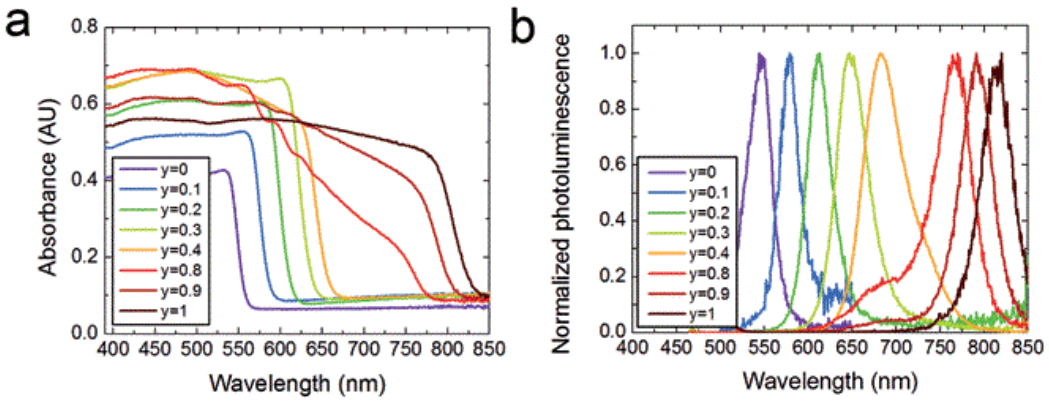


Figure 2.10 Tunability of the $FAPbI_yBr_{3-y}$ perovskite system. (a) UV-Vis absorbance of the $FAPbI_yBr_{3-y}$ perovskites with varying y, measured in an integrating sphere. (b) Corresponding steady-state photoluminescence spectra for the same films. Reproduced with permission from reference [38].

Absorption and emission characteristics of perovskite materials help us understand why these compounds show high performances. The most commonly studied iodide-based perovskite semiconductors ($FAPbI_3$ and $MAPbI_3$) strongly absorb light over a wide range, with an onset that varies depending on their bandgap [52] (an example is shown in Figure 2.10). The generated charge carriers in this process relax towards the conduction band minimum and valence band maximum then producing a bright and narrow emission via radiative recombination.

2.4.2 Urbach Energy

In 1953, Franz Urbach discovered that the absorption coefficient of AgBr depends exponentially on the energy of the photons [53]. Generally, this relationship can be represented with the formula [54]:

$$\alpha(\hbar\omega, \mathrm{T}) = \alpha_0 e^{-\sigma(E_0-\hbar\omega)/k_BT} = \alpha_0 e^{(\hbar\omega-E_0)/E_U} \qquad (2.22)$$

where α is the absorption coefficient, $\hbar\omega$ is the photon energy, α_0 and E_0 are constants, and $E_U=\sigma/k_BT$ describes the steepness of the absorption edge. Urbach's first observation of the logarithmic onset of the absorption coefficient α as a function of energy is shown in Figure 2.11. It is clear from the figure that α follows a $1/k_BT$ linear relationship.

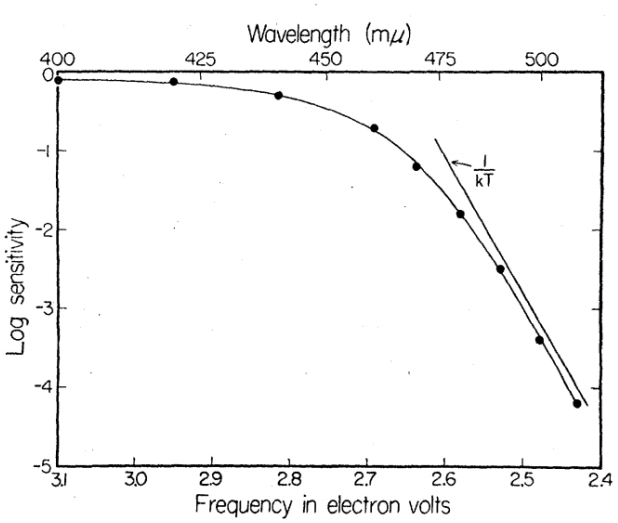


Figure 2.11 Temperature dependence of absorption of an AgBr crystal. The straight line represents the $1/k_BT$ slope at temperature T. Reprinted with permission from reference [39]. Copyright 1953 American physical society.

Thomas et. al. [55] observed that absorption below the band-gap can be associated with the excitation of an electron in the valence band by a photon with energy lower than the band-gap with assistance of a phonon. This kind of absorption depends on the strength of the electron-phonon interactions.

The Urbach energy E_U has been associated with the amount of local disorder in a solid [55]. In fact, the increase of this disorder will increase the absorption edge smear through the appearance of spatially separated local band gaps. This disorder can arise from defects [56]–[58], thermal lattice vibrations [56], [57], or composition [59], [60]. We will realise throughout this thesis that $Cs_2AgBiBr_6$ double perovskite possess a large Urbach energy (~60 meV), indicative of a high local disorder. This disorder may be related to the intrinsic properties of the absorber, or to the presence of defects boundaries in the thin film layers. In the second case, the Urbach energy may be reduced through meticulous optimization of the deposition process.

2.4.3 Defects tolerance

Defects have historically been divided in two categories: shallow and deep. Electrically active defects have different characteristics, depending on the location of their energy states relative to the conduction or the valence band. Deep defects typically reside within the middle third of the energy gap, while shallow defects have energy levels within a few tens of millielectronvolts from the band edges. To be more accurate, deep defects present well

localized wave functions, while shallow defects' wave functions are as extended as the Coulomb potential.

The ideal model for a solid requires an uninterrupted translational symmetry, and the electronic band structure E(k) can be calculated in this approximation. However, in reality defects within semiconductors are an important feature to consider. Although most solids maintain their essential properties upon introduction of small amount of external atoms, some semiconductor characteristics such as conductivity, free carrier mobility, and carrier lifetime change dramatically with the introduction of defects and impurities at a high enough concentration. For this reason, pure and structurally perfect crystals have to be prepared with precise crystallization methods (if required, these materials are then doped to change the electronic function of the crystal).

This is where perovskite materials distinguish themselves. Perovskites have a very high defect tolerance, as their main semiconductors properties do not seem to be affected by the presence of a high quantity of impurities (their conductivity, free carrier mobility and carrier lifetime are still high). A wide range of studies have associated this behaviour with the fact that these materials mostly form point defect states, which reside outside the electronic gap and are therefore less prone to form deep defects [61], [62].

2.4.4 Charge transport and recombination

Metal halide perovskites exhibit excellent charge-transport properties. The charge-carrier diffusion length, L_D, is a good quantitative representation of the quality of the semiconductor:

$$L_D = \sqrt{\frac{\mu k_B T}{e R_T}} \tag{2.23}$$

where T is the temperature, k_B the Boltzmann constant, μ is the charge-carrier mobility, e is the elementary charge, and R_T is the total charge-carrier recombination rate [48]. L_D represents the average distance that the excess carriers can cover before they recombine. For a solar cell we need L_D to be as high as possible, since the photogenerated charge carriers need to be able to reach the boundary of the absorber material, and finally the external circuit [63]. For efficient charge collection the diffusion lengths should exceed the absorption depth, as the thickness of the active layer is usually larger than the absorption depth to optimize the number of photons absorbed. The absorption depth in $MAPbI_3$ has been reported to be of the order of hundreds of nanometers [64], and the hole diffusion lengths

of several micrometers [65], [66]. For $MAPbI_3$ and $FAPbI_3$, the charge-carrier mobility has been measured to be of the order of 10 $cm^2V^{-1}s^{-1}$, which is relatively low if compared with common inorganic semiconductors. The slow recombination rate in metal halide perovskite films compensates this deficiency in mobility, as the lifetimes (the inverse of the total recombination rate) of charge carries have been reported to be of the order of several μs [67].

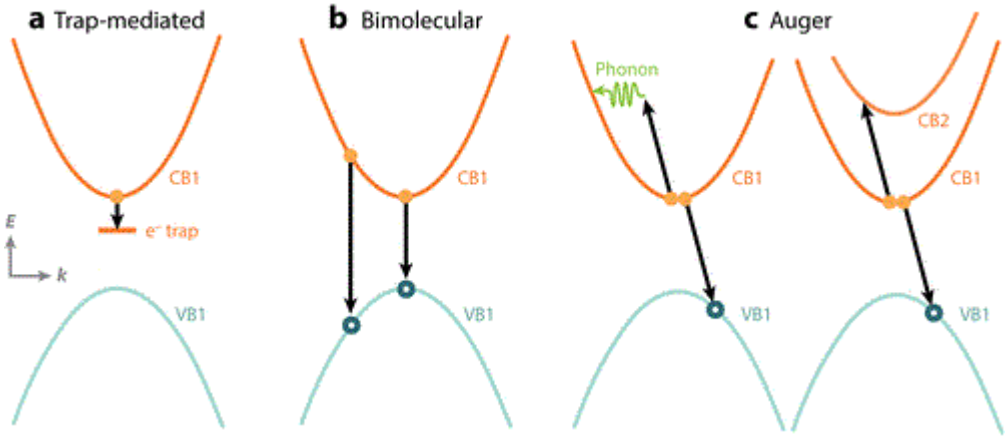


Figure 2.12 Schematic diagram indicating recombination mechanisms active in organic-inorganic metal halide perovskites. (a) Trap-assisted, (b) bimolecular (c) and Auger recombination. Abbreviations: CB, conduction band; CBM, conduction band minimum; VB, valence band; VBM, valence band maximum. Reproduced with permission from Annual Reviews via the Copyright Clearance Center. from reference [68].

Understanding the recombination processes that take place in semiconductor devices is fundamental to improve the performance of devices. The dynamics of charge-carrier recombination can be described by the following equation:

$$\frac{dn}{dt} = -k_3n^3 - k_2n^2 - k_1n = -R_T(n) \qquad (2.24)$$

Where *n* is the charge-carrier density, k_1 is the decay constant for first-order decay processes (monomolecular), k_2 is the second order (electron-hole, bimolecular) recombination rate constant and k_3 is the Auger recombination rate constant (trimolecular) [48]. These processes are shown in Figure 2.12. Bimolecular recombination involves intrinsic electron-hole recombination, and it is radiative. This process can be associated to the inverse process of absorption [68], [69]. Monomolecular recombination involves one charge carrier, it is usually mediated by traps, and can be radiative or non-radiative [70]. Finally, Auger recombination involves a third charge carrier: when the electron recombines with a hole, the excess energy is transferred to another electron, which is excited [48]. This third charge

carrier then releases back to the edge of the band and transfers its energy to lattice vibrations. This interaction becomes significant when the carrier density is very high, and it is relatively unimportant at charge carrier densities involved in photovoltaic applications [48]. Lead-based metal halide perovskites have been extensively studied with the use of photoluminescence measurements. These direct band-gap semiconductors emit just below the absorption edge, as shown in figure 2.10. Various transient PL studies proved that the recombination mechanisms of photoexcited charge carriers are strongly dependent on the fluence used [71]. At lower excitation densities, monomolecular recombination dominates.

2.4.5 Excitons in halide perovskites

In Section 2.4.1 we explained how the absorption of photons by an interband transition creates an electron in the conduction band and a hole in the valence band. These oppositely charged particles can attract each other through their mutual Coulomb interaction. If the right conditions are satisfied, a bound electron-hole pair can be formed. This neutral bound pair is called an exciton. There are two main types of excitons: Wannier-Mott excitons, also called free-excitons, and Frenkel excitons, also called tightly bound excitons. Wannier-Mott excitons are mainly observed in semiconductors, while Frenkel excitons are found in insulators and molecular crystals. In semiconductors, the dielectric constant is generally large, and the electric field screening tends to reduce the Coulomb interaction between electrons and holes. For this reason, free excitons have a radius larger than the lattice spacing, and they are delocalized states that can move freely throughout the crystal. Frenkel excitons, by contrast, have a much smaller radius which is comparable to the size of the unit cell. This makes them localized states which are tightly bound to specific atoms or molecules. Stable excitons will form only if the attractive potential is strong enough to protect them from collisions with phonons. Since the maximum energy of a thermally excited phonon is k_BT at temperature T, we have that $E_{ex} > k_BT$ has to be satisfied, where E_{ex} is the exciton binding energy. Wannier-Mott excitons have binding energy of the order of 0.01 eV (e.g. Silicon has an exciton binding energy of about 0.015 eV [72]), and at room temperature $k_BT \cong 0.025$ eV. For this reason, these excitons are usually only observed clearly at cryogenic temperatures. On the other hand, Frenkel excitons have larger binding energies, which makes them stable at room temperature.

In a free exciton, since the electron-hole separation is large, we can consider the particles as moving in an average uniform dielectric material and model the free exciton as a hydrogenic system. In this approximation, the radius of the electron-hole orbit is:

$$r_n = \frac{m_0}{\mu}\epsilon_r n^2 a_H \tag{2.25}$$

where a_H is the Bohr radius of the hydrogen atom, *n* refers to the principal quantum number, μ is the reduced mass and ϵ_r is the dielectric constant.

The free exciton model that leads to equation 2.25 breaks down when the predicted radius becomes comparable to the interatomic spacing. This typically occurs for large band gap materials with small dielectric constants and large effective masses. The theoretical treatment of Frenkel excitons requires the use of the tight binding approach since the excitons in this case are related to atomic or molecular states. In addition, the coupling between the excitons and the lattice is typically strong and self-trapping effects could occur. In this case the exciton produces a local distortion of the lattice, which enhances the localization of the exciton wave functions.

The exact value of exciton binding energies in metal-halide perovskites sees a significant spread for reported values in literature [73]–[79]. The fraction of excitons which thermally dissociate into free electrons and holes is an essential information for the understanding of solar cell performances, as it gives rise to the free-charge carrier transport. The Coulomb correlations between electrons and holes affect the operation of photovoltaic cells because the resulting bound state presents a binding energy that needs to be overcome to dissociate in free charge carriers. If $E_B < k_B T$, the thermal energy might be enough to dissociate the exciton at room temperature. Wannier-Mott excitons are expected to be present in halide perovskites [80]. Absorption measurements are the most straightforward method to determine the exciton binding energy. The absorption spectrum of a direct-bandgap semiconductor with hydrogen-like excitonic effects can be described with the Elliot formula [81], which contains a term describing the absorption of continuum states enhanced by the Coulomb interaction (Sommerfeld term) and one relative to the discrete excitonic state absorption that lies below the bandgap edge. The band edge absorption onset in an ideal semiconductor is shown in panel a of Figure 2.13, while an example of fitting of the low temperature absorption spectrum of $MAPbI_3$ is shown in panel b.

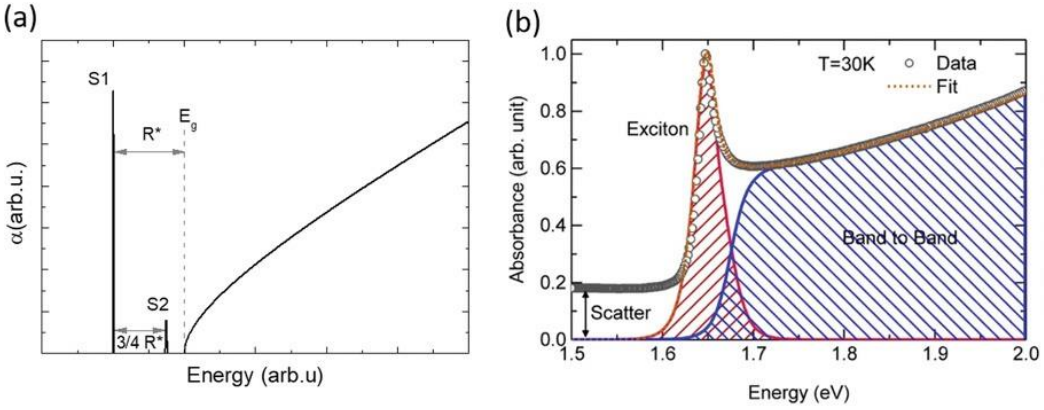


Figure 2.13 a) Idealized absorption spectra of semiconductor with excitonic effects. Example of the fitting of the absorption spectra of $MAPbI_3$ at 30 K using Elliott's formula with the excitonic and band-to-band contribution. Adapted with permission from reference [72] and [80].

In polycrystalline thin films of $MAPbBr_3$, we can only see the 1s exciton state, merging with a continuum of states. This is due to the fact that the absorption resonances are strongly broadened even at very low temperatures. For this reason, in the case of perovskite semiconductors the extrapolation of the exciton binding energy from absorption measurements is not as easy as it could be.

A more reliable technique in this case is related to magneto-optical studies. The shift in energy of the exciton transition in a magnetic field is easier to track. Recent magneto-optical measurements have predicted the exciton binding energy in $MAPbI_3$ and $MAPbBr_3$ to be in the range of 10-15 meV at low temperatures. Exciton binding energies extracted at room temperature are generally smaller than those obtained at cryogenic temperatures [80]. This is understandable if one takes in account the dual nature of metal-halide perovskites. In fact, it is believed that at low temperatures these materials behave like an ordinary semiconductor crystal, however, at higher temperatures they assume a crystal-liquid behaviour, with an enhanced dielectric screening[82], [83]. This behaviour refers to the fact that the high-temperature cubic phase of hybrid-halide perovskites is similar to a crystalline lattice with long-range translational order but local rotational disorder. For this reason, these materials present a crystalline-like response in coherent band transport of charge carriers, and liquid-like response in phonon activities. Due to enhanced screening, the exciton binding energy is reduced to a few meV at room temperature, partially justifying the excellent perovskite device performances. In fact, efficient thermal dissociation of excitons happens at room temperature (k_BT~25 meV).

The strength of excitons not only depends on the value of the binding energy, but also on the structural properties of the material. Depending on structural characteristics, excitons can be more or less confined. When excitons interact with phonons, self-trapping can occur depending on the strength of the interaction. If the coupling is weak, as in Si or GaAs semiconductors, excitons are scattered by the phonons. However, if the coupling is strong, especially in combination with a soft lattice, excitons can become self-trapped. This happens when the excitons are dressed with a dense cloud of virtual phonons, which suppresses the ability of excitons to move across the crystal, and the lattice undergoes a local deformation around the exciton. In alkali halides, photogenerated holes are self-trapped by two adjacent halogen ions approaching one another [84]. In the self-trapping process, the exciton will lose some energy and at the same time the energy of the ground state will rise because of lattice deformation. For this reason, the emission of self-trapped excitons is characterized by a large Stokes shift.

2.4.6 Polaronic effects in perovskites

The electron mobility in semiconductors can be greatly affected by the formation of polarons. Lead halide perovskites are soft ionic semiconductors, which means that the electronic and longitudinal optical phonon states are coupled, and we should discuss the possibility of polarons in the lattice. A polaron is a charge carrier dressed by the local lattice polarization, which results from the Coulomb interaction between charge carriers and the ionic lattice. We can classify two kind of polarons, depending on the spatial extent of the lattice deformation. If the polarization cloud extends over less than a single unit cell, we have the formation of a small polaron. On the other hand, if the extension covers distances much greater than the unit cell, we are in the presence of a large polaron.

Recent measurements have demonstrated that lead halide perovskites present large polarons features [80]. The large polarons might explain the low mobility of carriers in perovskites, which is surprising given that the carrier effective mass has been reported to be quite low . Despite these findings, the large polarons seem to not be significantly detrimental to lead halide perovskites photovoltaic applications, only causing some partial coupling to the lattice but at the same time allowing for efficient charge extraction [85].

As we will see in Chapter 7, double perovskite $Cs_2AgBiBr_6$ is believed to present a strong localization, which results in a highly Stokes-shifted emission, several hundreds of meV lower than the absorption energies. This happens because the deformation of the lattice and the change in kinetic and potential energy of the charge carriers result in large energetic losses.

In this case, the small polarons may substantially limit the charge-carrier mobility and lead to charge-carrier self-trapping and fast non-radiative recombination, which are detrimental for photovoltaic applications.

2.4.7 Huang-Rhys oscillator model

The Huang-Rhys model is a first-order perturbative theory on optical transitions, which can be applied whenever there is absorption or emission involving localized defects or impurity centres, due to electron-phonon coupling.

Because of vibrational coupling, the shape of absorption and emission spectra depends on the temperature. In fact, at cryogenic temperatures we are able so observe fine structure, which is lost at room temperature because of broadening effects. The energy difference between the maxima of the absorption and emission spectrum relative to an electronic transition is called Stokes shift.

We assume that the reader will be familiar with the Franck-Condon principle, which explains the intensity of vibronic transitions. The energy potential associated with an ion in a solid is in a first order approximation harmonic. When developing a quantum mechanical description of this energy potential we find the occurrence of vibrational states, which hold an energy $(n+1/2)\hbar\omega$. A schematic diagram is shown in Figure 2.14.

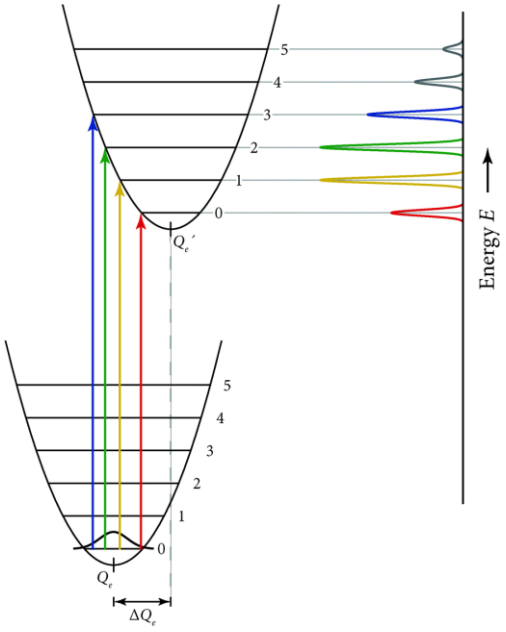


Figure 2.14 Configuration coordinate diagram of two electronic states with S=2. Multiple transitions are possible in the absorption process, as shown by the arrows, giving rise to a structured absorption

band at cryogenic temperatures, and a broad band at room temperature. Reproduced with permission from reference [86].

When an electronic transition occurs, there can be a change in the vibrational state. A fine structure spectrum arises, with lines of intensity corresponding to the square of the overlap between the vibrational wavefunctions. When the temperature increases, these peaks broaden and the fine structure disappears. This broad band will have an energy maximum that depends on the displacement ΔQ_e between the harmonic potentials in the ground and excited state. This difference relates to the different equilibrium geometries in these two states, which can be associated to changes in bonding resulting from a different electronic configuration. ΔQ_e is related to the so-called Huan-Rhys parameter by: $S = \frac{1}{2}\alpha(\Delta Q_e)^2$ with $\alpha=\mu\omega/\hbar$ where μ is the reduced mass of the vibrating system [87]. The S factor is a measure of the strength of the electron-phonon coupling and can be associated with the average number of phonons involved in a particular electronic transition. From quantum-mechanical calculations, the Stokes shift can be expressed as $E_{Stokes}=(2S-1)\hbar\omega$, while other works use the relation $E_{Stokes}=2S\hbar\omega$ [88].

2.5 Perovskite solar cells

We do not discuss the fundamentals of semiconductor junctions here, as it is assumed that most readers would be already familiar with these topics.

2.5.1 Photovoltaic device characterization

Solar cells are typically described in terms of current density dependence under an applied voltage and light bias. By sweeping the voltage applied to the solar cell we can extract the current density-voltage (J-V) characteristics, along with its critical parameters (open circuit voltage V_{OC}, short-circuit current density J_{SC}, voltage at maximum power point V_{mpp}, current density at maximum power point J_{mpp}, and fill factor FF). To model the current, we can first consider a solar cell in the dark. In this case, the cell behaves like a rectifying diode, producing a dark current under bias described by the ideal diode equation:

$$J_{dark}(V) = J_0\left(e^{\frac{qV}{k_BT}} - 1\right) \tag{2.26}$$

where J_0 is the dark saturation current and V the applied bias. When the cell is exposed to light, a photocurrent (J_{SC}) that flows in the opposite direction of the dark current is generated and equation 2.26 becomes:

$$J_{light}(V) = J_0\left(e^{\frac{qV}{k_BT}} - 1\right) - J_{SC} \tag{2.27}$$

The open-circuit voltage V_{OC} is the maximum voltage available from a solar cell, and this occurs at zero current. Setting the net current equal to zero in equation 2.27 we obtain:

$$V_{OC} = \frac{k_BT}{q}\ln\left(\frac{J_{SC}}{J_0} + 1\right) \tag{2.28}$$

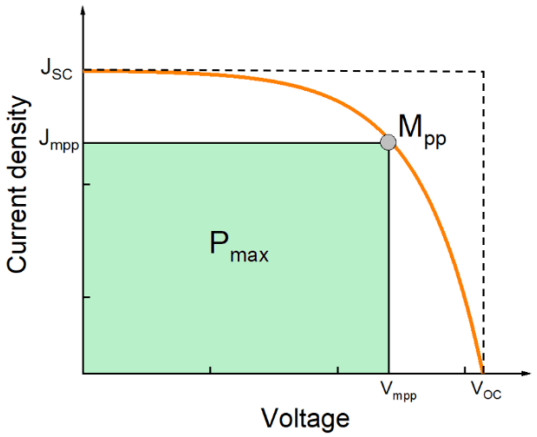


Figure 2.15 General current density – voltage characteristic curve of a solar cell device under sun illumination.

The open-circuit voltage V_{OC} and the short-circuit current I_{SC} are the maximum current and voltage respectively, however at both of these operating points the power from the solar cell is zero. The fill factor (FF) determines the maximum power from a solar cell in conjunction with V_{OC} and I_{SC}, and is defined as:

$$FF = \frac{J_{mpp}V_{mpp}}{J_{SC}V_{OC}} \tag{2.29}$$

Graphically, the FF is a measure of the "squareness" of the solar cell and is also the area of the largest rectangular fit to the J-V curve, as illustrated in Figure 2.15.

The long-time stability of solar cells is an important requirement for commercialization of PSCs [89], and various factors are responsible for the degradation of perovskite and other constituents of perovskite solar cells. Factors can be both intrinsic or extrinsic (environmental), and a lot of effort is being put towards stability and reliability testing [12], [15], [20], [89]–[93].

2.5.2 Detailed balance limit

In 1961, William Shockley and Hans Queisser published an article that describes the physics of an absorbing semiconductor solar cell using the thermodynamic principles of the detailed balance. They predicted the maximum power conversion efficiency of a single p-n junction. This is known as the Shockley Queisser (SQ) limit or alternatively the detailed balance limit [28]. According to a re-visited model, the maximum efficiency is obtained for a material with a bandgap of E_g=1.34 eV, which finds a balance between the thermalization losses of the absorbed photons with energy higher than E_g, and the number of solar photons available at E_g [94]. So far, only a few materials have a bandgap close to the ideal one, e.g. gallium arsenide (GaAs), $CuIn_xGa_{1-x}Se_2$ (CIGS), and certain perovskite materials (this is where the high tunability of the perovskite bandgap has an important role). The limit can be exceeded with a variety of techniques such as hot-carrier extraction, producing multiple carriers per absorption of a photon, and using multi-junction solar cells [95]. Nevertheless, the detailed balance limit remains the main reference for solar efficiency comparisons as it provides a systematic mathematical method that can effectively model the performance of a solar cell.

The two main principles used to calculate the SQ limit are the principle of the detailed balance and Planck's law. Additionally, the model assumes that all the incident photons with energy higher than the band-gap are absorbed, and that each absorbed photon generates one electron-hole pair. Other assumptions are that the recombination processes are all radiative, and the charges are transported to the external circuit without losses. The idealized SQ solar cell is described through its bandgap and its temperature. The bandgap E_g defines the threshold for light absorption, which is assumed in this case to be zero below the bandgap and maximum above it (every photon is absorbed above E_g). The photogenerated current density J_{sc} under illumination from the photon Ω_{sun} will be:

$$J_{sc} = q\int_0^\infty a(E)\Omega_{sun}(\mathrm{E})\mathrm{dE} = q\int_{E_g}^\infty \Omega_{sun}(E)dE \qquad (2.30)$$

where q is the elementary charge and the absorptance a(E) is assumed to be a step function around E_g.

Because of the detailed balance principle, the photon flux in and out of a device are equal in equilibrium. Therefore, the amount of radiation that is absorbed is equal to the amount that is emitted if the environment and device have the same temperature, e.g. they are in thermal equilibrium. The absorbed flux will then simply be the one radiated from a blackbody at temperature T, following Planck's law. When the cell is illuminated with

sunlight, the thermal equilibrium is disturbed, and the electron and hole quasi fermi levels are separated by a chemical potential qV. In this case we can use the generalized Planck's law that was introduced by W$\ddot{u}$rfel [96]. The emitted photon flux Ω from the ideal diode under applied bias voltage V will then be:

$$\Omega(\mathrm{V},\mathrm{E}) = \frac{2\pi E^2}{h^3 c^2} \frac{a(E)}{\left[\exp\left(\frac{E-qV}{k_B T}\right) - 1\right]} \tag{2.31}$$

where h is the Planck constant, c the speed of light in vacuum, a(E) the absorptance of the solar cell and $k_B T$ the thermal energy.

If $E-qV >> k_B T$, when the emitted photon energies are greater than the voltages, we can approximate the Bose-Einstein term by a Boltzmann distribution obtaining:

$$\Omega(\mathrm{V},\mathrm{E}) = \mathrm{a}(\mathrm{E})\Omega_{bb} \qquad where \quad \Omega_{bb} = \frac{2\pi E^2}{h^3 c^2} \exp\left(-\frac{E}{k_B T}\right) \tag{2.32}$$

Which is equal to the equilibrium black-body emission times a scaling factor $e^{\frac{qV}{k_B T}}$.

If we keep the cell at a bias voltage V and under illumination, using Equation 2.30, the deficit current density will be:

$$J_{sc} - J(V) = q \int_{E_g}^{\infty} \Omega(E) dE = e^{\frac{qV}{k_B T}} q \int_{E_g}^{\infty} \Omega_{bb}(E) dE = e^{\frac{qV}{k_B T}} J_0 \tag{2.33}$$

where J_0 is the dark saturation current.

The open-circuit voltage will be obtained simply setting the total current J=0:

$$V_{oc} = \frac{k_B T}{q} ln\left(\frac{J_{sc}}{J_0} + 1\right) \tag{2.34}$$

and the efficiency of the cell will be:

$$\eta = \frac{J_{sc} V_{oc} FF}{P_{opt}} \tag{2.35}$$

where FF has been defined in the previous Section, and P_{opt} is the optical power density for the incoming radiation. For an unconcentrated AM1.5G spectrum, the maximum efficiency is around 33%, as shown in Figure 2.16. In actual devices, the efficiencies are lower due to other non-radiative recombination mechanisms and losses in parasitic resistances.

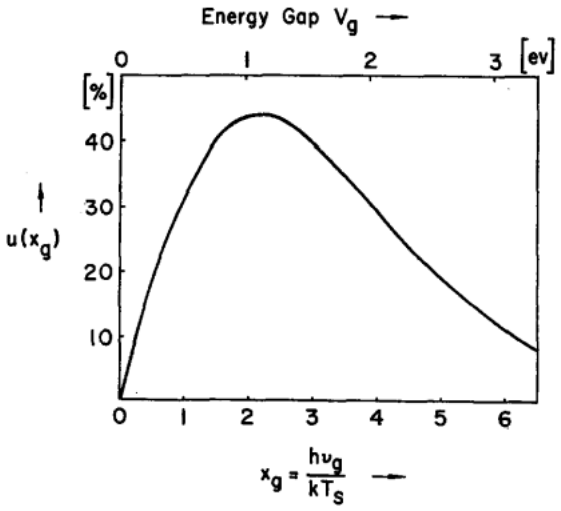


Figure 2.16 Dependence of the efficiency $U(x_0)$ of a solar cell upon the energy gap V_g of the semiconductor. Reproduced with permission from [75].

For bandgaps greater than ~1.45 eV, there are too many unabsorbed low energy photons, while for bandgaps smaller then ~ 1 eV the lower energy per electron/hole pair leads to a decrease in V_{oc} and efficiency, despite the higher values of photocurrent.

Figure 2.16 shows the record efficiency of solar cells of different materials against their bandgap, in comparison to the SQ limit [97]. The best perovskite cells approach the best silicon solar cells in efficiency, despite being in the research community for a shorter time.

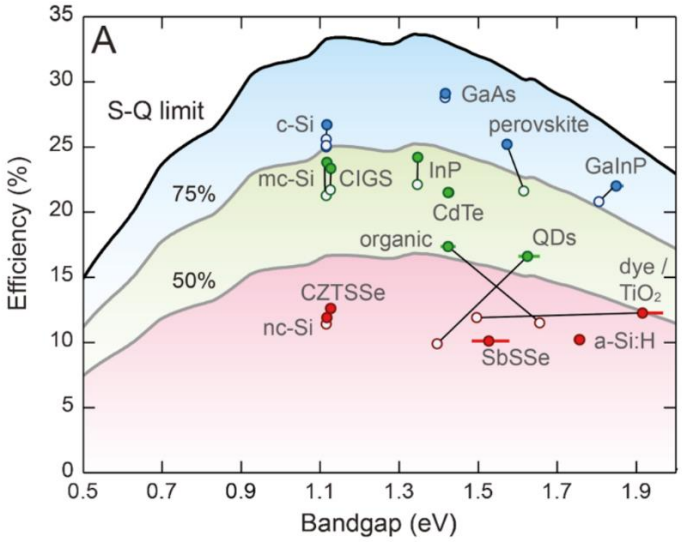


Figure 2.16 Record efficiency of solar cells of different materials against their bandgap, in comparison to the SQ limit (top solid line). Reproduced with permission from [97]. Copyright 2020, American Chemical Society

2.5.3 Perovskite photovoltaics

Photovoltaics using organic-inorganic lead halide perovskite materials as absorber layer have shown tremendous improvement in solar cell performance, surpassing the highest efficiencies of semiconductor compounds such as CdTe and CIGS in only 12 years, and approaching the highest values achieved with crystalline silicon solar cells [14]. Moreover, the low-cost and low-temperature solution-based processes used for device fabrication makes perovskite solar cells (PSCs) promising for potential commercialization due to the scalability and compatibility with large scale manufacturing processes.

In 2009 Miyasaka and co-workers were the first to show the use of $CH_3NH_3PbI_3$ halide perovskite as light absorbing material in dye-sensitized solar cell (DSSC) architecture, reaching 3.8% PCE [13]. In this configuration, a mesoporous titania (TiO_2) layer provides a physical scaffold for the thin layer of dye (in this case a thin layer of perovskite) as well as immediate collection of electrons generated in the light-absorbing layer. The charge balance is achieved by a redox couple in the electrolyte, and the perovskite crystallises as nanocrystals within the pores of the titania scaffold. Despite the discovery, the rapid degradation of the perovskite absorber due to its dissolution in the liquid electrolyte hindered remarkable device performances. This problem was eventually solved by using a solid-state architecture with doped materials such as Spiro-OMeTAD as a solid hole-transporting layer, achieving efficiencies over 9% [98], [99]. In 2012, Lee et al. achieved 10.9% in power conversion efficiency with the remarkable discovery that an insulating mesoporous oxide scaffold Al_2O_3 would lead to devices that performed equally to those using the semiconducting TiO_2 scaffold, which is essential for electron extraction in DSSCs [100]. This suggested that charge-diffusion lengths were long enough to reach their respective electrodes. Electron-hole diffusion lengths were later quantified with the use of time resolved photoluminescence measurements to be of the order of 1 μm in thin film $MAPbI_3$ perovskite [101]. This long diffusion length allowed for the evolution of planar heterojunction devices with n-i-p and p-i-n architectures.

Organic-inorganic halide perovskite show semiconductor properties that qualify them as an excellent material for solar cells. In fact, they have exceptionally high electron and hole mobilities of around 10 $cm^2V^{-1}s^{-1}$[48], a short absorption depth of the order of 100 nm [64], as well as low radiative and non-radiative recombination rates [67]. Charge recombination rates are slow, which means that the open circuit voltage is close to the ideal limit set by the radiative limit approximation [102]. Urbach energies, which qualitatively measure the

electronic disorder in the material, are reported to be as low as 15 meV for the $MAPbI_3$ perovskite [49], which indicate high achievable voltages. A fundamental property for semiconductor materials in photovoltaic applications is the exciton binding energy (E_{ex}). E_{ex} is the energy required to split the electron-hole charge pair apart and can vary dramatically from a few meV to about 100 meV in halide perovskite publications [80]. A low exciton binding energy is required to achieve highly efficient solar cells, so that we can assume that most photoexcited carriers are present as free charges, finally contributing to the current of the device. Miyata et al. performed rigorous magneto-optic measurements which confirmed an exciton binding energy of only a few meV at room temperature [82]. Since this value is lower than the thermal energy $k_BT \approx 25$ meV at room temperature, we can assume that free carriers are the main photoexcited carriers in lead-halide hybrid perovskites. Another particularly important property of perovskites is the possibility to tune the bandgap by changing their chemical structure. This feature allows for the band gap to vary from 1.24 to 2.3 eV.

In 2020, 138.2 gigawatts (GW) of new photovoltaic capacity was installed worldwide [103]. A very large majority of these modules use monocrystalline and multi-crystalline Silicon [104]. The next step for solar technology would be to drop the value of LCOE (Levelized Cost of Energy). However, with the only use of Silicon solar cells a further cost reduction is unlikely, or at least very challenging. The cost of installed solar panels comprise the solar module itself, the balance of systems (BoS) which regards all the costs associates with the installation, and the cost of operation. BoS and fabrication costs have been effectively managed to the lowest possible values, and the improvement in cost reduction will likely soon reach a plateau in the coming next years. In this scenario, working on the efficiency of the modules seems to be the best pathway for cost reduction, as the energy yield would increase while maintaining the same fabrications and BoS costs. The practical efficiency limit of silicon single-junction devices is ~29% [104]. At the end of 2020, the certified efficiency of perovskite-silicon tandems reached 29.52%, which would suggest that the use of perovskite tandems is an approachable pathway to LCOE cost reduction. Further reductions might be achieved through all-perovskite tandems. In the meanwhile, the PCE of single-junction solar cells reached ~25%, and is likely to reach the highest certified PCE of crystalline silicon solar cells (26.7%) soon [105].

2.5.4 What are the challenges?

Substantial losses are present in halide perovskite materials due to deep trap-assisted recombination. Charge carriers combine non-radiatively to the trap without contributing to device performance. This can happen, for example, at grain boundaries [106]. There is still a certain level of uncertainty over the exact nature of the defects that might be causing the trap clusters [107]. Moreover, the management of interfaces still limits the open-circuit voltage, fill-factor and stability of the devices, by introducing additional non-radiative pathways and energy barriers, or inducing perovskite deprotonation [108]. A possible route to solve this problem is passivation of the interfaces [93].

Stability is also one of the main factors which will need to be taken in account for commercialization. It is well-known in literature that $MAPbI_3$ is thermodynamically unstable, and many efforts have been going towards developing more stable halide perovskites compositions [91], [92], [109]. In addition, the toxicity of lead causes some concern about risks associated with the perovskite lifecycle [110]. Beyond the hazards associated with lead, the solvents used in perovskite processing (e.g. N,N-dimethylformamide) can be just as hazardous, if not even more. Further effort must be put into discovering solvent-free methods or benign solvents.

2.6 Double perovskites

As we have discussed in the previous sections, lead-halide perovskites feature remarkable optoelectronic properties, with long diffusion lengths >1μm, strong optical absorption of the order of 10^5 cm^{-1}, and high photoluminescence quantum efficiencies. However, the toxicity of the lead content and limited air-stability of some compositions has motivated researchers to investigate new lead-free and stable materials. The investigation of lead-free perovskites is currently one of the most popular research directions in the field. Various non-toxic alternatives, such as replacing Pb^{2+} with Bi^{3+} or Sb^{3+} have been explored [111]–[115]. However, these material present poor thermal and air stability and low performance. Halide double perovskites with general formula $A_2B'B''X_6$ have a flexible composition due to a large range of possible B' and B'' site elements. Volonakis *et. al.* in 2016 computationally designed the family of Pb-free inorganic halide double perovskites $Cs_2B'B''X_6$ with B'= Cu, Ag or Au, B''= Bi or Sb, and X= Cl, Br, or I [21]. Using first-principle calculations they showed that this family has very promising optoelectronic properties, such as tunable band gaps in the visible range and low carrier effective masses (which is an indication of high carrier mobility [116]).

Along with the computational calculations, they synthesized the $Cs_2AgBiCl_6$ compound, which they assigned to belong to the $Fm\bar{3}m$ space group (rock-salt ordering structure). Other groups in the same year independently reported the synthesis and optoelectronic properties of elpasolites Cs_2AgBiX_6 (with X being Cl^- and Br^-) [117]. These compounds are all predicted to have an indirect bandgap [21], which implies weak oscillator strengths for absorption and radiative recombination. A solution would be to use a thick absorber layer, as it is done with silicon [118], which is undesirable in thin film solar cells applications if the charge carrier mobilities are low [119]. The performances of these materials are still quite low, as they present a modest PCE of ~2% in the case of $Cs_2AgBiBr_6$ [25]. Nevertheless, there is a lot of research still yet to be conducted in order to understand these materials and optimise them for various optoelectronic applications. Moreover, it has been proven that in contrast to lead-halide perovskites $Cs_2AgBiBr_6$ is highly stable. This constitutes a strong reason to further study the intrinsic properties of this double perovskite in order to be able to optimize its use in optoelectronic devices.

3. Experimental methods

In this chapter we introduce the experimental techniques forming the foundation of this thesis. The first section describes the synthesis of single crystals and polycrystalline powders. X-ray diffraction has been used extensively during this work to investigate the structural properties of the samples. Heat capacity measurements have been used to detect the presence of phase transitions, while neutron diffraction at the ISIS Neutron and Muon source (UK) has been used to characterize the low-temperature phase of the compounds. The optical properties have been investigated with the use of photoluminescence spectroscopy, UV-Vis spectroscopy and other techniques performed by our collaborators (where explicitly stated). Lastly, the device fabrication procedure and characterization techniques are described in detail. The work presented in the next chapters has been performed by the author of this thesis, unless stated otherwise.

3.1 Samples synthesis

This thesis focuses on the properties of the double perovskites $Cs_2AgBiBr_6$ and $Cs_2AgBi_{1-x}In_xBr_6$. In this section, we will explore the methods that have been used to synthesize these samples.

3.1.1 Powders

Perovskite materials in the powder form exhibit high stability [89] and allow for easy production of large quantities. $Cs_2AgBiBr_6$ powder samples, shown in Figure 3.1, were synthesised through precipitation: the chemicals AgBr (2 mmol, 99.5% purity), CsBr (4 mmol, 99% purity), and $BiBr_3$ (2 mmol, ≥98% purity) were dissolved in ~4 mL of DMSO (dimethyl sulfoxide) and then precipitated with acetone, producing ~2 g of powder after drying. Full structural characterization of the material will be described in the next Chapter.

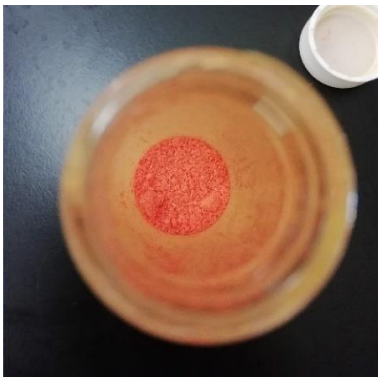


Figure 3.1 Photograph of polycrystalline $Cs_2AgBiBr_6$ double perovskite in a glass vial.

3.1.2 Single crystals

The ability to grow semiconductors in the form of single crystals has a fundamental role in solar cell research. Single crystals reflect, as close as possible, the intrinsic properties of a semiconductor. Moreover, they usually exhibit better electronic characteristics, as they display exceptionally low trap densities (about six orders of magnitude lower than their polycrystalline films counterparts) [120].

Single crystals of $Cs_2AgBiBr_6$ double perovskite have been previously synthesised using hot HBr (hydrobromic acid) [23] exploiting a solution temperature lowering (STL) method. The difference in solubility of the perovskite precursors in the solvent under different temperatures allows for the synthesis. The perovskite precursors are dissolved into the solvent at higher temperatures, then the temperature of the solution is gradually reduced to reach a supersaturated state which results in the growth of single crystals. Reproducing this route was not possible due to the lack of complete solubility of the salts in hot HBr solution, therefore we added another step to the process. We first precipitated the polycrystalline powder, and then we dissolved the compound (~1g) in ~10 mL of 9 M HBr, heating it at 110°C. When the sample was cooled to room temperature at a rate of 0.5 degrees per hour, we obtained ~1mm size single crystals. A photograph is shown in Figure 3.2. The complete characterization is discussed in the next Chapter.

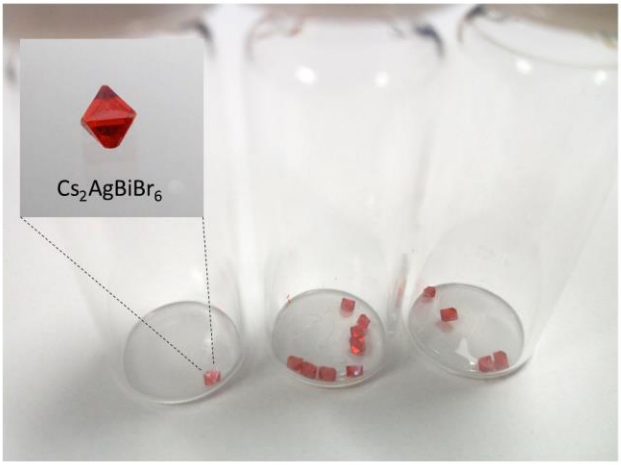


Figure 3.2 Photograph of $Cs_2AgBiBr_6$ single crystals grown by the solution process described in the main text. The insert on the top-left corner zooms on a single crystal showing its symmetric shape.

For the synthesis of $Cs_2AgBi_{1-x}In_xBr_6$ single crystals, we followed a modified version of this synthesis route. We synthesised $Cs_2AgBiBr_6$ polycrystalline powder as described before, and then dissolved the as-synthesized powder in hot HBr (~ 110°C) with the addition of $InBr_3$ in

different proportions for each vial. Upon cooling the solution to room temperature at a rate of half a degree per hour, we grew single crystals with a diverse range of indium contents. The full characterization of these compounds is described in the next chapter. Figure 3.3 shows the compounds with no indium and 25% of indium, respectively. We can notice the colour getting lighter with the increased indium concentration.



Figure 3.3 Photograph of $Cs_2AgBiBr_6$ (left, SC0) and $Cs_2AgBi_{0.9}In_{0.1}Br_6$ (right, SC25) single crystals.

3.1.3 Thin films

Planar thin films solar cells that use a perovskite layer to provide light absorption, ambipolar charge transport and charge generation require a high-quality thin film of perovskite. When using solution processing methods, the perovskite layer is typically deposited by spin-coating: a small amount of solution is applied on the centre of the substrate, which is either spinning at low speed or not spinning at all. The substrate is then rotated at speed up to a certain rpm (rotation per minute) to spread the coating material by centrifugal force.

For the perovskite $Cs_2AgBi_{1-x}In_xBr_6$ layer we dissolved the precursors: AgBr (99%), $BiBr_3$ (>98%), $InBr_3$ (99.998%) and CsBr (99.9%) in DMSO (0.3M). The solution has been spin-coated at 4000 rpm (with an acceleration of 4000 rpm/s) for one minute in air and then heated at 285°C for 5 minutes. A photograph of thin films on quartz substrates is shown in Figure 3.4.

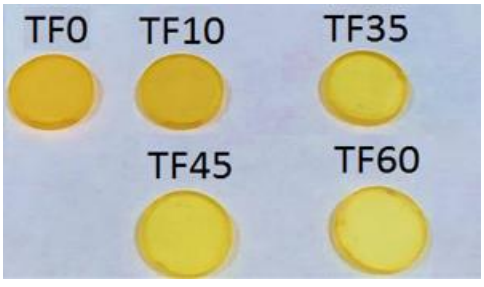


Figure 3.4 Photograph of $Cs_2AgBi_{1-x}In_xBr_6$ thin films on a quartz substrate. From the top left, thin film with 0% indium (TF0), 10% (TF10), 35% (TF35), 45% (TF45) and 60% (TF60).

3.2 Diffraction

3.2.1 Fundamentals

In 1913 W. H. and W. L. Bragg discovered that crystalline materials gave remarkably characteristic patterns of reflected X-radiation, quite unlike those produced by liquids [121]. In crystalline materials, for certain sharply defined wavelengths and incident directions, intense peaks of scattered radiation (Bragg peaks) were observed. These peaks carry information that can be used to deduce structural details of the material.

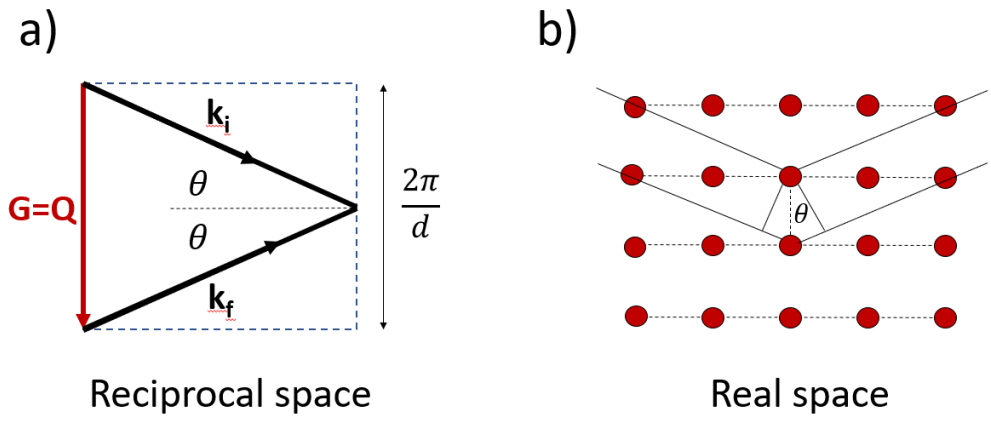


Figure 3.5 a) Laue condition and b) Bragg's law representation in a two-dimensional square lattice.

Rays specularly reflected from adjoining planes are shown in Figure 3.5. The X-rays (or neutrons) with wavevector $\mathbf{k}_i$ and energy $\hbar\omega_i$ are scattered by a crystalline sample into a state with final wavevector $\mathbf{k}_i$ and energy $\hbar\omega_f$. The change in wavevector will be the scattering vector:

$$\boldsymbol{Q} = \boldsymbol{k}_f - \boldsymbol{k}_i \tag{3.1}$$

In the case of elastic scattering, we have $|\mathbf{k}_i|=|\mathbf{k}_f|$, and thus the module of the scattering vector will be:

$$|\boldsymbol{Q}| = \frac{4\pi sin\theta}{\lambda} \tag{3.2}$$

To obtain constructive interference of the scattered X-rays (or neutron), the Laue condition has to be true [11]:

$$\boldsymbol{Q} \cdot \boldsymbol{R}_n = 2\pi n \tag{3.3}$$

Where $\mathbf{R}_n$ is any lattice vector locating the origin of the n^{th} unit cell ($\mathbf{R}_n=n_1\mathbf{a}+n_2\mathbf{b}+n_3\mathbf{c}$ where **a**, **b**, and **c** are the basis vectors of the lattice). The vectors that satisfy this equation are reciprocal lattice vectors ($\mathbf{Q}=\mathbf{G}$), such that the scattering vector must coincide with a reciprocal lattice point for constructive interference to be observed. Considering $d=2\pi/|\mathbf{G}|$ and with straightforward calculations we can derive the scalar part of Laue's condition [11]. This is called Bragg's law, and is given by:

$$n\lambda = 2dsin\theta \tag{3.4}$$

where n is an integer, λ the wavelength of the incident radiation, and d is the spacing between the family of atomic planes associated with the corresponding diffraction peak.

In a diffraction experiment, the scattered intensity $I(\mathbf{Q})$ is measured as a function of the scattering angle (and hence **Q**, from eq. 3.2). To predict the intensity of Bragg scattering, we have to consider the rate of scattering S for a given scattering vector, which depends on the Fourier transform of the interaction potential $H_{int}(\mathbf{r})$ between the radiation and the material:

$$S \propto \left| \int_{material} d\boldsymbol{r}\, e^{i\boldsymbol{Q}\cdot\boldsymbol{r}} H_{int}(\boldsymbol{r}) \right|^2 \delta(E_f - E_i) \tag{3.5}$$

Here the delta function ensures that the energy is conserved. The interaction potential, which is useful in the general case of particle scattering and in particular of neutrons diffraction, is substituted with the electron density in the case of X-ray diffraction. In fact, in the case of X-ray diffraction, the rate of scattering is calculated using classical relations.

We can re-express the general position, considering a crystalline material, as $\mathbf{r} = \mathbf{R}_n + \mathbf{x}$, where **x** is a position within the unit cell. Substituting this into Eq. 3.5 and using the periodicity of the potential $H_{int}(\mathbf{R}_{int}+\mathbf{x})$, we have:

$$S \propto \left| \left[\sum_n e^{i\boldsymbol{Q}\cdot\boldsymbol{R}_n} \right] \left[\int_{cell} d\boldsymbol{x} e^{i\boldsymbol{Q}\cdot\boldsymbol{x}} H_{int}(\boldsymbol{x}) \right] \right|^2 \delta(E_f - E_i) \tag{3.6}$$

The first term in this equation will sum up to zero unless the terms add up coherently, due to the nature of $\mathbf{R}_n$. This happens only if the Laue condition (Eq. 3.3) is respected. For constructive interference to occur, we require the scattering vector to be a reciprocal lattice vector, so we can re-write the first term in brackets as:

$$\left[\sum_n e^{i\boldsymbol{Q}\cdot R_n} \right] = \frac{(2\pi)^3}{V_{cell}} N_{cell} \delta^{(3)}(\boldsymbol{G} - \boldsymbol{Q}) \tag{3.7}$$

where N_{cell} is the number of unit cells contributing to the scattering process.

In equation 3.6, the second term in squared brackets is called structure factor, which we can call F(**Q**). This term determines the relative intensities of the diffraction peaks and it depends on the charge distribution in the unit cell of the material. We can re-express one of the position vectors as: $x = x_n + x'$ where x_n is the position of an atom inside the unit cell. The structure factor then becomes:

$$F(\boldsymbol{Q}) = \sum_{n}^{cell} \int_{atom} e^{i\boldsymbol{Q}\cdot\boldsymbol{x'}} H_{int}(x_n + x') e^{i\boldsymbol{Q}\cdot\boldsymbol{x_n}} = \sum_{n}^{cell} f_n(\boldsymbol{Q})\, e^{i\boldsymbol{Q}\cdot\boldsymbol{x_n}} \qquad (3.8)$$

where $f_n(\mathbf{Q})$ is known as the atomic form factor. This factor differs in base of the type of scattering radiation. X-rays are scattered by the electron cloud of the atoms and hence the scattering amplitude increases with the atomic number Z of the atoms in a sample. As a result, X-rays are not very sensitive to light atoms, and there is very little contrast between elements adjacent to each other in the periodic table. The case of neutrons is different, since they almost exclusively interact with nuclei. In this case, the form factor will depend mainly on the nuclear properties of the isotopes present in a material.

3.2.1 X-ray diffraction instrumentation

Powders and thin film samples were characterized using a Panalytical X'pert powder diffractometer with Cu anode X-ray source (Cu-Kα1 ≈ 1.54060 Å). Measurement at low temperatures have been performed employing an Oxford Cryosystems PheniX cryostat. Symmetry analysis was performed using the Isotropy Suite [122].

Single crystal X-ray diffraction has been performed using an Agilent Supernova diffractometer with Mo-Kα radiation. Symmetry analysis was performed using the same Isotropy Suite [122]. Crystal structures were visualised and XRD patterns simulated using the 3D visualization program VESTA.

3.2.2 Neutrons diffraction

Neutron powder diffraction has been performed using the time-of-flight diffractometer POLARIS (a high flux, medium resolution diffractometer) at the ISIS Spallation Neutron Source [123]. A ~5 g powder sample was loaded into a 6mm diameter cylindrical vanadium can. Room temperature data were collected for 350 μA.hours integrated proton beam current to the ISIS target, corresponding to ~2 hours beamtime. The sample was then removed from the sample changer and placed in a helium flow "orange" cryostat and cooled slowly from room temperature to 30K. The low temperature data set was collected for 450 μA.hours (corresponding to ~2.6 hours beamtime).

3.4 Heat Capacity

The heat capacity has been measured with the use of a Quantum Design Physical Properties Measurement System (PPMS), varying the temperature of the samples (a 5.2 mg single crystal). The system measures the heat capacity at constant pressure:

$$C_p = \left(\frac{dQ}{dT}\right)_p \tag{3.9}$$

The Quantum Design Heat Capacity option controls the heat added to and removed from a sample while monitoring the resulting change in temperature. During a measurement, a known amount of heat is applied at constant power for a fixed time, and then this heating period is followed by a cooling period of the same duration.

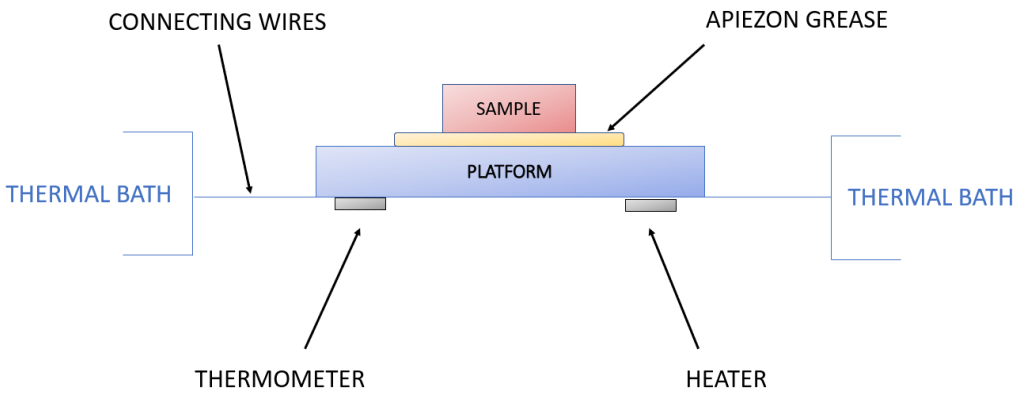


Figure 3.6 Thermal Connections to Sample and Sample Platform in PPMS Heat Capacity Option.

As illustrated in Figure 3.6, a platform heater and a platform thermometer are attached to the bottom side of the sample platform. Small wires provide the electrical connection to the platform heater and platform thermometer and provide the thermal connection for the platform. A sufficient vacuum is created with the use of a pump, which ensures that the conductance between the sample platform and the thermal bath is entirely dominated by the conductance of the wires.

3.5 Photoluminescence spectroscopy

3.5.1 Steady-State Photoluminescence

Steady-state photoluminescence was measured by exciting single crystals and polycrystalline powders with a fibre-coupled 405 nm laser. The signal has been detected from the top surface via a fibre bundle (Ocean Optics QR600-7-SR125BX) coupled with a spectrometer (QE Pro, Ocean Optics).

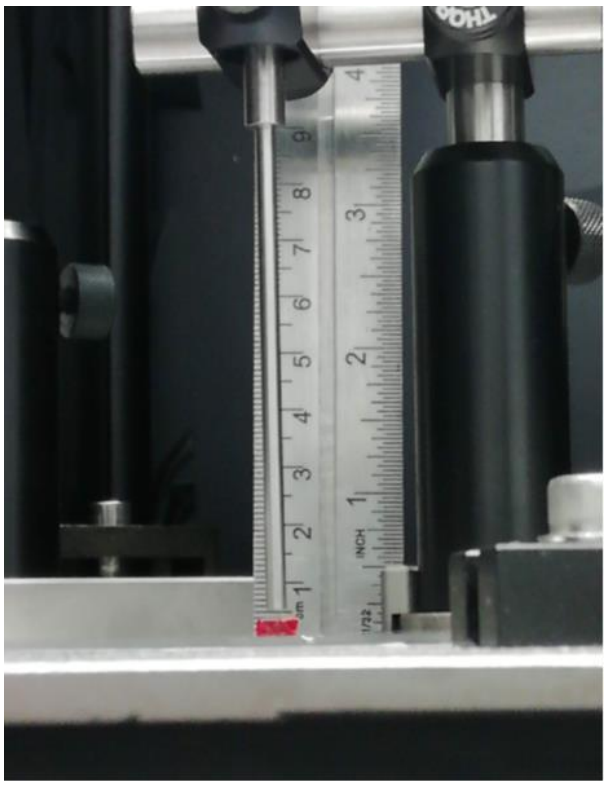


Figure 3.7 Photograph of a single crystal and the fibre bundle used to collect steady-state photoluminescence spectra.

3.5.2 Time-Resolved Photoluminescence

A luminescent decay is characterized by the fall-off of the luminescence intensity i(t) at times $t \geq 0$ having been switched off at time t=0. Knowledge of the temporal behaviour of the luminescence signal carries valuable information contributing to the characterization of the recombination process and the nature of the luminescence centres. Time-resolved photoluminescence spectroscopy (TRPL) is used to study carrier dynamics in photoluminescent materials by collecting time-dependent emission data. A laser pulse emitted at fixed frequency is used to perturb the sample, and a fast detector is used to determine the emission of the material as a function of time after excitation.

A TRPL set-up includes a pulsed laser source, a triggering system, an optical path, light correcting optics, optical filters, and a detector. To achieve a good temporal resolution (on a picosecond timescale) the sample emission is strongly attenuated before reaching the detector. In any given collection interval, the probability of collecting a photon at the detector is low, and a photomultiplier tube amplifies the signal. The low probability of a single photon collection is balanced by the frequency of the detector collector, which ranges between 500 kHz to a few MHz. The signal histogram is built over a sampling period of minutes, where every current pulse at the output of the photomultiplier corresponds to the impact of one photon on the photocathode, accompanied by the emission of a photoelectron. The number of pulses registered per unit time is then proportional to the number of photons hitting the photocathode during the same interval, i.e. to the incident light flux or intensity. This technique is known as time-correlated single photon counting (TCSPC). Measurements were recorded using a time-correlated single photon counting (TCSPC) setup (FluoTime 300 PicoQuant GmbH).

TRPL decays were fitted with a stretched exponential model summed to a monoexponential:

$$I(t) = Ae^{-t/t_1} + Be^{\left(-t/t_2 b\right)} \tag{3.10}$$

I(t) is the PL intensity at time t, t_1 and t_2 are the characteristic lifetimes and *b* is the stretching exponent.

The monoexponential function is commonly used to fit PL transients [124], [125], and arises from neglecting the bimolecular and Auger terms in Eq. 2.24. A biexponential function may also be used to account for two decay components, attributable to separate populations of charge carriers [120], [126]. The stretched exponential function has been used to phenomenologically account for the presence of a local distribution of monoexponential decay rates [52], [127]. The distribution coefficient, which is bound to be between 0 and 1, accounts for a more heterogeneous distribution of decay rates. The average lifetime of a stretched exponential is usually given as:

$$t_{av} = \frac{t_2}{b}\Gamma\left(\frac{1}{b}\right) \tag{3.11}$$

Where Γ is the gamma function [128].

3.6 UV-Vis absorption spectroscopy

Absorption spectra were collected with a Varian Cary 1050 UV Vis Spectrometer. The transmittance and reflectance were measured with a Perkin Elmer Lambda 1050, equipped with a 100 nm integrated sphere. Absorption is a closely related process to emission, and provides complementary information to PL spectroscopy. This technique measures the wavelength-dependent absorption characteristics of a material, and it can be used to find the energies associated with excitonic and band gap transitions.

3.7 Device preparation

Devices were fabricated in the n-i-p structure: ITO/SnO_2 nanoparticles/$Cs_2AgBi_{1-x}In_xBr_6$/Spiro-OMeTAD/Ag. Pre-cut glass/ITO substrates were cleaned by sequential sonication in soap, water, acetone and isopropanol. After being dried with an N_2 gun, the substrates were further cleaned with O_2 plasma for 10 minutes. Tin oxide nanoparticles were prepared using 0.178 mL SnO_2 dispersion (15% in H_2O) in 0.822 mL of milliQ water. For the perovskite $Cs_2AgBi_{1-x}In_xBr_6$ layer we dissolved the precursors: AgBr (99%), $BiBr_3$ (>98%), $InBr_3$ (99.998%) and CsBr (99.9%) in DMSO (0.3M). The solution was spincoated at 4000 rpm (with an acceleration of 4000 rpm/s) for one minute in air and then heated at 285°C for 5 minutes. The hole transport material (Spiro-OMeTAD, Lumtec) was dissolved in chlorobenzene (85 mg/mL) and doped with 20 µl of LiTFSI (500 mg/ml in BuOH) and 30 µl of tert-butylpyridine. The solution was then deposited on the active layer by spin-coating in air at 2000 rpm (2000 rpm/sec) for 45 sec. The devices were then left overnight in a desiccator in air atmosphere, and then completed by the evaporation of 100 nm silver contacts. All the characterization were performed in air.

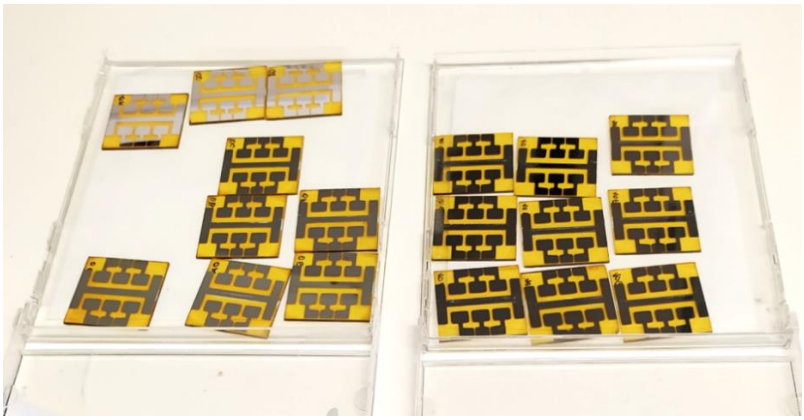


Figure 3.8 Photograph of n-i-p devices samples, where the absorber is $Cs_2AgBi_{1-x}In_xBr_6$, prepared as described in the main text.

3.8 Device characterization

3.8.1 Current Density-Voltage (JV) Measurements

All the J-V characteristics have been measured under AM1.5 illumination generated by a WAVELABS SINUS-220 solar simulator. Each full device stack is divided into 6 pixels of 0.25 mm^2 area, inside a 30x30 mm square mask.

Double perovskite $Cs_2AgBiBr_6$ solar cells are characterized by significant hysteresis [129]. For this reason, voltage scans are not always a good indication of solar cell performance, as the shape of the J-V curve will depend on the direction and speed of the scan. Therefore, for each measurement we also perform steady state V_{OC}, J_{SC}, and maximum power point (MMP) scans. During these scans the voltage is kept constant around V_{OC}, 0 V, or V_{MPP} for 30 seconds to let the system stabilise. The stabilised values are reported at the end of the scan, giving a more solid indication of solar cell performance. J-V curves are measured with a time step of around 43 ms and a voltage step a hundredth of the full range, which means, for example, 14 mV steps for the range from -0.2 to 1.2 V.

3.8.2 External Quantum Efficiency

External quantum efficiency was acquired with a custom build Fourier transform photocurrent spectrometer utilizing a Bruker Vertex 80v Fourier Transform Interferometer. Devices were calibrated to a Newport-calibrated silicon reference solar cell with known external quantum efficiency, and illuminated with an AM1.5 filtered solar simulator. Device active areas were masked with a metal aperture, having an active area of 0.0919 cm^2.

3.8.3 Photoluminescence Quantum Efficiency

For the measurement of the photoluminescence quantum efficiency (PLQE), a CNI Low Noise Violet Blue 405 nm 200 mW laser is used with an integrating sphere and an Ocean Optics Maya2000 Pro spectrometer. A calibration halogen lamp from OceanOptics is used to calibrate the system, including the sphere, fibre and spectrometer. The PLQE is calculated according to the method developed by De Mello et. al in 1997 [130].

PLQE can be interpreted as the ratio of radiative to non-radiative recombination under open-circuit conditions. Radiative recombination is strongly related to absorption, while non-radiative recombination is a purely parasitic process, therefore the higher the PLQE, the better the achievable performance of the solar cell [131]. Each order of magnitude decrease

in PLQE causes a V_{OC} loss of 60 mV in the thermodynamic limit, as shown with the use of thermodynamic modelling [132], [133].

4. Low-temperature transition in $Cs_2AgBiBr_6$ double perovskite

The work presented in this chapter has been published in:

Schade, L.; Wright, A. D.; Johnson, R. D.; Dollmann, M.; Wenger, B.; Nayak, P. K.; Prabhakaran, D.; Herz, L. M.; Nicholas, R.; Snaith, H. J. and Radaelli, P. G "Structural and Optical Properties of $Cs_2AgBiBr_6$ Double Perovskite" *ACS Energy Lett.* **2019**, 4, 1, 299-305.

DOI: 10.1021/acsenergylett.8b02090

Direct link: https://doi.org/10.1021/acsenergylett.8b02090

Reproduced with permission from ACS Energy Lett. 2019, 4, 1, 299-305. Copyright 2019 American Chemical Society

4.1 Context and summary

Organometal lead halides perovskites have been extensively investigated due to their outstanding optoelectronic properties such as a tunable bandgap, impressive tolerance to defects, high carrier mobilities, strong absorption coefficient, and long exciton diffusion length. Up to now, PSCs power conversion efficiencies reached an impressive 28% [14]. Nevertheless, these hybrid materials suffer from degradation of the organic component under exposure to environmental conditions, limiting the operating life-times of the devices. For this reason, researchers have recently focused their attention on all inorganic perovskites, which have proved to show a higher thermal stability [22]. $CsPbI_3$ has been one of the mostly studied compounds for this purpose, however to date it has proven highly challenging to stabilize the room-temperature crystalline polymorph of this material [134]. At the same time, the discovery of the impressive functionality of lead halide perovskites had driven the attempt from the research community to discover new metal-halide semiconductors with improved properties.

Double perovskites with general formula $A_2^{1+}M^{1+}M'^{3+}X_6$ have been recently proposed as all-inorganic alternatives. Among them, $Cs_2AgBiBr_6$ is one of the few materials which have delivered substantial photovoltaic performance since the discovery of lead halide perovskite solar cells. While stability has proven to be one of the main challenges of lead halide perovskite materials [135], $Cs_2AgBiBr_6$ is highly stable, both structurally and chemically [22].

Additionally, this material has been predicted to have relatively low carrier effective masses [21], and it has shown long carrier recombination lifetimes [23]. When this work was carried out, Greul et al. [24] and Gao et al. [25] had incorporated $Cs_2AgBiBr_6$ thin films into working devices for the first time, achieving a 2.23% of power conversion efficiency. Although this value is significantly lower than the PCE of hybrid perovskites devices, this family of materials is also much less mature in terms of device technologies and has significant potential for applications, as demonstrated by the discovery of highly efficient neat white light emission from the $Cs_2AgInCl_6$ double perovskite [115]. Furthermore, they represent a good model system to understand deficiencies and to optimize the search for new compounds in the same family.

While some effort was made to improve the performances of the material, very little was known about its intrinsic properties, and particularly how the structural properties impact the optoelectronic characteristics. This information is fundamental in order to improve this family of double perovskite, and also to design new compounds with improved or complementary properties.

This Chapter focuses on the structural properties of the $Cs_2AgBiBr_6$ compound, with the characterization of both single crystals and powders samples. Low-temperature dependent XRD measurements resulted in the discovery of a low-temperature phase never reported before. A complete structural solution for the new phase is also detailed in this Chapter.

4.2 Experimental details

Single crystals and powders were synthesized according to the procedure described in subsection 3.1. Experiments were carried out and analysed by the author of this thesis unless stated otherwise. Neutron-diffraction data were collected by Ron Smith at the ISIS Pulsed Neutron and Muon Source, supported by a beamline allocation from the Science and Technology Facilities Council under the Xpress programme.

4.3 Results

4.3.1 Room temperature X-ray diffraction

On the basis of X-ray diffraction measurements, McClure et al. [117] determined the ambient-temperature crystal structure of $Cs_2AgBiBr_6$ to be cubic with a=11.2711(1) Å and space group $Fm\bar{3}m$, which accounts for the Ag/Bi ordering on a rock-salt superstructure. We

characterized our single crystals and powders with the use of X-ray diffraction. The single crystal data were fit with the established cubic crystal structure [117] giving outstanding goodness-of-fit, which demonstrated excellent crystal quality. The complete single crystal XRD pattern is shown in Figure 4.1. Figure 4.2 shows the plot of F^2_{calc} versus F^2_{obs}, along with a plot of the x=y function (red dashed line) as a guide for the eye. The data points perfectly follow the line, indicating outstanding crystal quality.

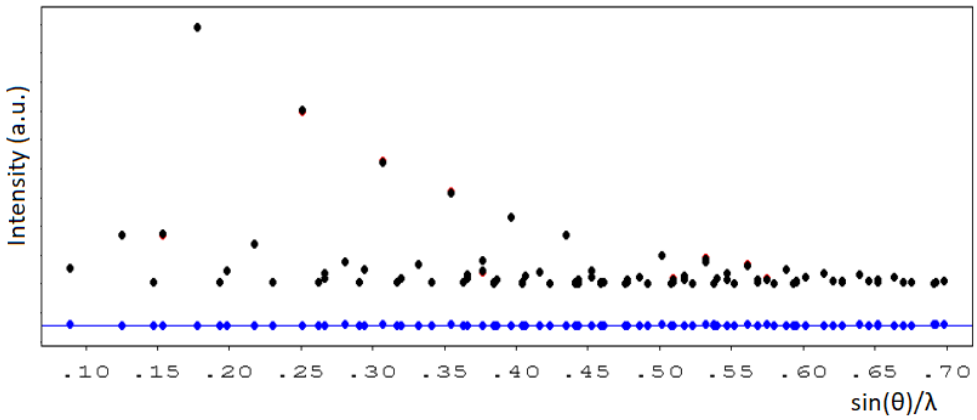


Figure 4.1 – Single crystal XRD pattern and least-square fitting. The red circles (which are almost completely hidden by the fitting) are the experimental data points, the black ones the fitting ones, and the blue ones the residuals.

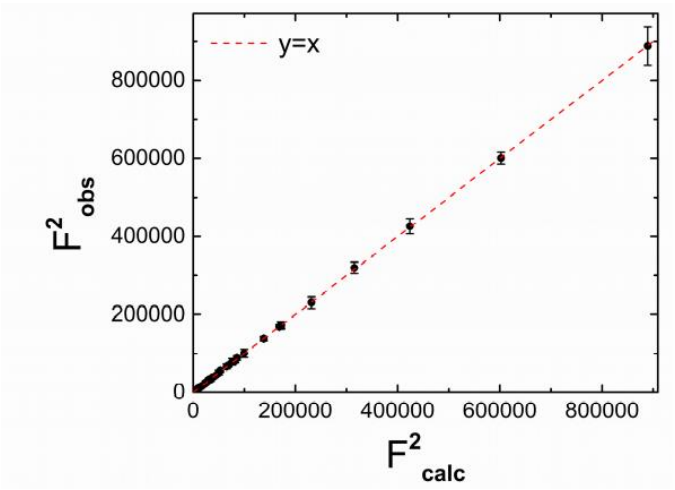


Figure 4.2 Plot of F^2 calc versus F^2_{obs} for the structural refinement of a $Cs_2AgBiBr_6$ single crystal. The red line is a guide to the eye. The data points perfectly follow the line, indicating excellent crystal quality.

Structural information for the single crystals is detailed in table 4.1. Lattice parameters differ from the ones previously reported in [117] by a 0.027%.

Cell parameters

Space group:	$Fm\bar{3}m$
Z = 4	
a	11.2741(2)
$V_{f.u.}$	358.250(1)

Refinable atomic fractional coordinates

Atom	x	y	Z
Br	0.25093(2)	-	-

Anisotropic atomic displacement parameters (x100 [Å²])

Atom	U_{11}	U_{22}	U_{33}
Cs	4.86(1)	4.86(1)	4.86(1)
Bi	1.76(7)	1.76(7)	1.76(7)
Ag	2.50(2)	2.50(2)	2.50(2)
Br	1.69(1)	7.13(2)	7.13(2)

Data collection

measured reflections: 363
independent reflections: 35
Data reduction R_{int} : 5.33%
(Criterion for observed reflections: $I > 3.0\sigma(I)$)
observed reflections: 359
fitted parameters:9

Table 4.1 Room-temperature crystal structure of $Cs_2AgBiBr_6$, as refined from single crystal X-ray diffraction data. In $Fm\bar{3}m$ the atoms are located at the following Wyckoff positions. Cs: 8c (1/4, 1/4, 1/4) ; Bi: 4a (0, 0, 0); Ag: 4b (1/2, 1/2, 1/2); Br: 24e (x, 0, 0). $V_{f.u.}$ stands for volume per formula unit. The off-diagonal anisotropic displacement parameters $U_{12}=U_{13}=U_{23}$ are =0 by symmetry.

A real-space representation of the room-temperature crystal structure is shown in Figure 4.3, based on our structural refinement.

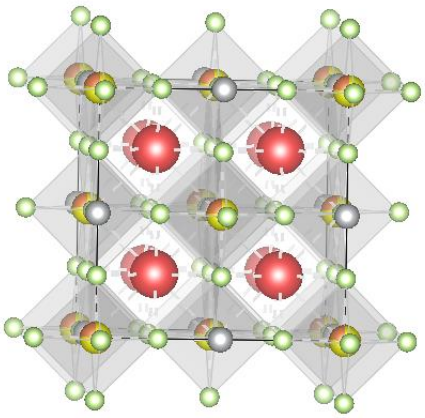


Figure 4.3 Representation of the $Cs_2AgBiBr_6$ crystal structure. The red circles represent the Cs atoms, the green ones the Br, and the yellow-orange ones represent the Bi atoms and the grey ones the Ag.

Powder samples were characterized with the use X-ray (presented here) and neutron (presented in sub-section 4.3.4) diffraction. Figure 4.4 shows the XRD pattern and the Rietveld refinement for the $Cs_2AgBiBr_6$ powder samples at room temperature. The fit with the same cubic structure model well reproduced the majority of peaks in the diffraction pattern. However, a ~20 wt % $CsAgBr_2$ impurity phase was also identified.

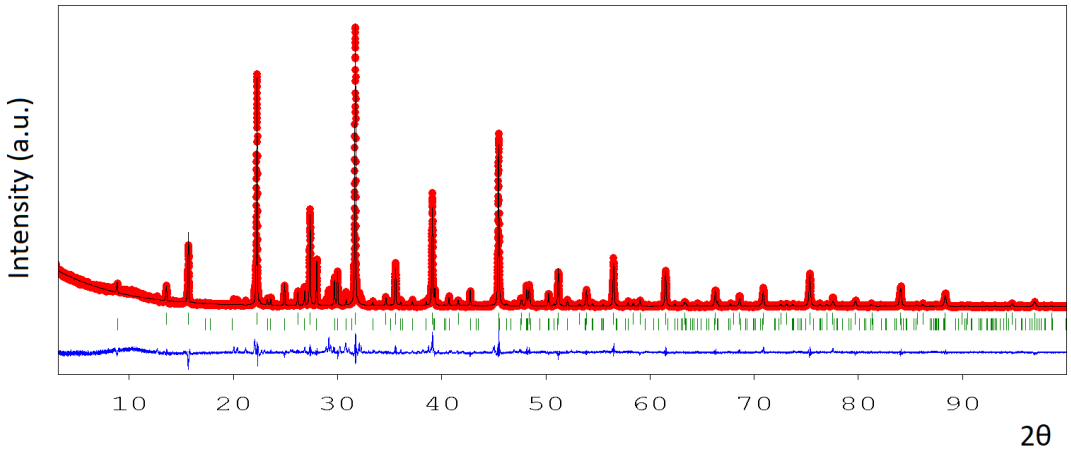


Figure 4.4 X-ray diffraction pattern with Rietveld refinement measured for $Cs_2AgBiBr_6$ powders. The red dots represent the experimental points, while the black pattern is the calculated one. The green vertical lines represent the main phase (upper) peak positions, and the impurities – secondary phases – (down) peak positions.

In both refinements, the B-site cations were found to be fully ordered within the sensitivity of the measurement (the occupancy of Ag and Bi was found to be 1.00±0.05). This is important to note because the optical properties may change with the degree of occupational disorder of the B-site [136].

4.3.2 Temperature dependent heat capacity

Temperature-dependent heat capacity measurements were performed to investigate the possibility of a phase transition at low temperatures. A 5.2 mg $Cs_2AgBiBr_6$ single crystal was used for this measurement. The data are shown in Figure 4.5a, where we observe a sharp anomaly at $T_s \simeq 122$ K, indicative of a second order or weakly first order phase transition. From detailed measurements on heating and cooling near this transition temperature T_s, as shown in Figure 4.6, we can observe the absence of thermal hysteresis.

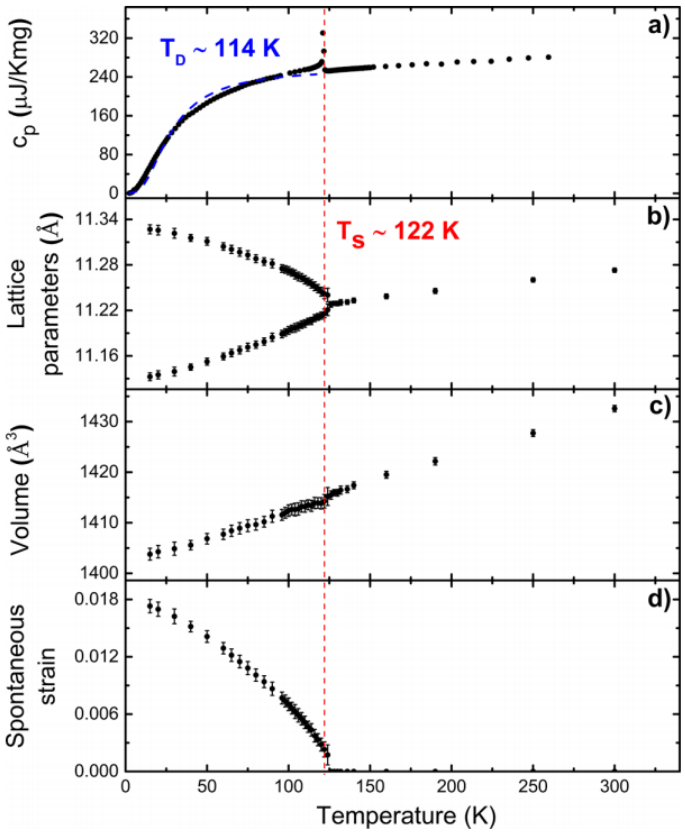


Figure 4.5 Temperature dependence of a) the heat capacity (error bars are smaller than the data points; the dashed line is a Debye fit to the data below the phase transition), b) lattice parameters, c) the unit cell volume, and d) the spontaneous strain. The red line marks the transition temperature at $T_s \simeq 122$ K.

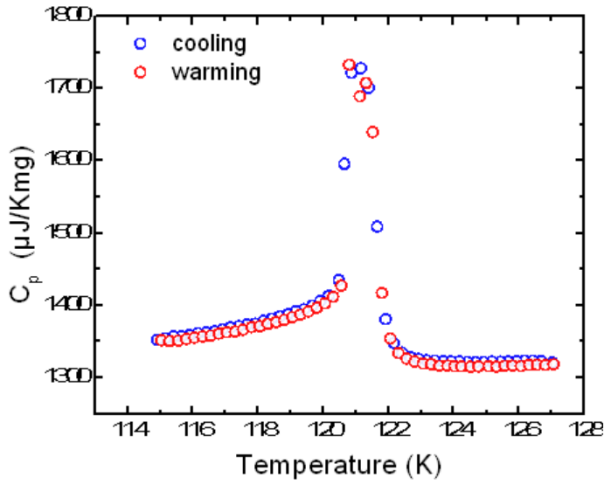


Figure 4.6 Specific heat capacity near the transition temperature T_s on both cooling (blue circles) and warming (red circles).

We fitted the $T<T_s$ heat capacity c_p range with a Debye model (Eq. 4.1), obtaining a Debye temperature of T_D=114(4) K. The factor N represents the number of modes, which has been

considered as a free parameter in the fit. The factor x is the temperature of the system. The fit curve is shown as a blue dashed line in Figure 4.5a. The small discrepancy between the fitting curve and the experimental data can be addressed considering that the density of states (DOS) of the phonons doesn't exactly follow the Debye law, and it is higher at lower frequencies.

$$c_p(x) = 9Nk_B\left(\frac{T}{T_D}\right)^3 \int x^4 \frac{e^x}{(e^x-1)^2}\,dx \tag{4.1}$$

The T_D value found for this material is lower than the most commonly known hybrid-halide perovskites [137]. The Debye temperature can be linked to the hardness or softness of a material.

$$T_D = \frac{\hbar\omega_D}{k_B} \tag{4.2}$$

In fact, in equation 4.2 ω_D is the Debye frequency, which can be thought as the maximum frequency the solid normal modes can stand and we can write:

$$\omega_D = \omega_{max} = v_s|\boldsymbol{k}_{max}| = \frac{2\pi v_s}{\lambda_{min}} \tag{4.3}$$

where v_s is the propagation velocity of sound in the solid [11]. Equations 4.2 and 4.3 combined tell us that the Debye temperature is proportional to the sound velocity in a solid. We can then conclude that $Cs_2AgBiBr_6$ double perovskite has lower values of the sound velocity and bulk modulus B ($T_D \propto \sqrt{B}$ [138]) if compared with other common hybrid perovskites. This results in a slightly softer material.

4.3.3 Temperature dependent X-ray diffraction

The presence of a structural phase transition was confirmed with the use of temperature dependent X-ray diffraction. The diffraction peaks become strongly split below T_S, as shown in Figure 4.7. The range ~[32-33]° in the Figure shows the $(400)_c$ peak (where the subscript "c" indicates the cubic phase) at room temperature (light blue curve) and at lower temperatures down to ~15K. We can notice a slight splitting starting at around 122K, which then increases for lower temperatures. The peak splitting is consistent with the lowering of the crystal symmetry to tetragonal with a unit cell elongation along the *c* axis.

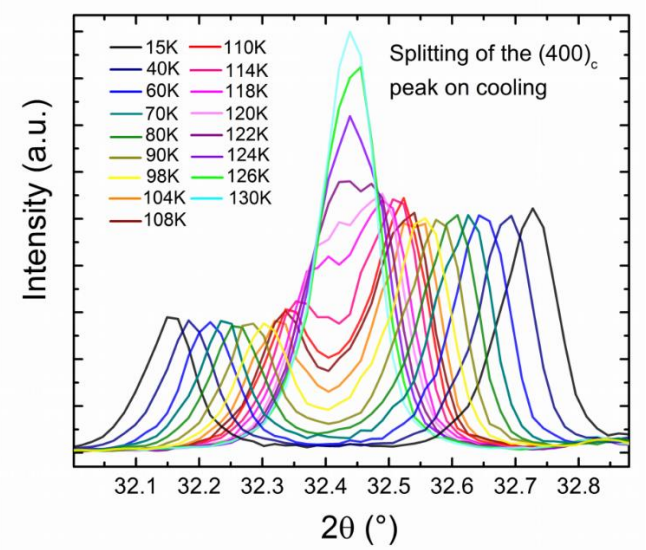


Figure 4.7 X-ray diffraction pattern plotted in the range ~[32-33]°, where the $(400)_c$ peak of the cubic room-temperature structure is present, in function of temperature.

This symmetry then persists down to the lowest measured temperature (15 K). We assumed tetragonal symmetry, which is the highest symmetry compatible with the $(400)_c$ splitting in two peaks, and we fitted the peaks at each temperature with a Gaussian shape. After extrapolating the peaks positions we calculated the corresponding lattice parameters and volume with the use of the Laue equation (Eq. 3.2 in Chapter 3). These are illustrated as a function of temperature in panels b and c of Figure 4.5.

4.3.4 Neutron powder diffraction

To determine the low-temperature tetragonal crystal structure of $Cs_2AgBiBr_6$, we collected neutron powder diffraction (NPD) data at room temperature and at 30 K. The cubic structure was refined against our room-temperature NPD data, as shown in panel a of Figure 4.8. We found an excellent agreement with our previous single crystal XRD refinement (illustrated in sub section 4.3.1). The list of the two sets of room-temperature structural information are listed in Table 4.2, in the room temperature neutron powder diffractions (NPD) and powders XRD columns.

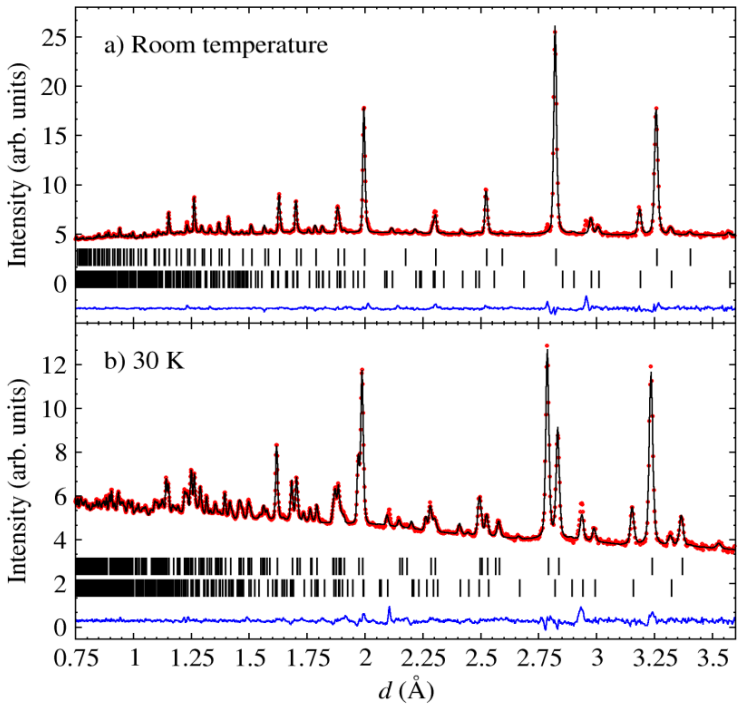


Figure 4.8 Neutron-diffraction patterns with Rietveld refinement for the time-of-flight neutron diffraction profiles measured for $Cs_2AgBiBr_6$ at a) room temperature and b) 30 K. The red dots represent the experimental points, while the black pattern is the calculated one. The black vertical lines represent the main phase (upper) peaks positions, and the impurities -secondary phases- (down) peaks positions.

	NPD 30K	NPD RT	XRD RT
	$I4/m$	$Fm\bar{3}m$	$Fm\bar{3}m$
Lattice Parameters [Å]			
$a_{t,c}$	7.8794(4)	11.2784(5)	11.27301(9)
$c_{t,c}$	11.3236(7)	11.2784(5)	11.27301(9)
$V_{f.u.}$ [Å^3]	351.51(3)	358.66(3)	358.145(5)
Refinable atomic fractional coordinates			
Br1 x	0.27976(2)	0.25072(1)	0.25143(2)
y	0.77941(2)	-	-
Br2 z	0.24959(2)	-	-
Atomic displacement parameters $100\times U_{iso}$ [Å^2]			
Cs	0.900(9)	4.517(1)	3.56(4)
Ag	0.204(5)	1.169(1)	0.55(4)
Bi	0.475(5)	2.229(2)	1.99(8)
Br1	0.966(7)	4.879(1)	4.05(4)
Br2	0.966(7)	-	-
Refinement reliability parameters [%]			
R_p	1.02	1.37	0.96
R_{wp}	1.04	1.41	2.59

Table 4.2 Refined crystal structure parameters for $Cs_2AgBiBr_6$. $a_c \approx \sqrt{2}a_t$; $c_c \approx c_t$, where subscripts c and t refer to the cubic and tetragonal unit cells, respectively. In $Fm\bar{3}m$, the atoms are located at the following Wyckoff positions. Cs: 8c (1/4, 1/4, 1/4) ; Bi: 4a (0, 0, 0); Ag: 4b (1/2, 1/2, 1/2); Br1: 24e (x, 0, 0). In the I4/m space group: Cs: 4d (1/2, 0, 1/4); Bi: 2a (0, 0, 0); Ag: 2b (0, 0, 1/2); Br1: 8h (x, y, 0); Br2: 4e (0, 0, z). $V_{f.u.}$ stands for volume per formula unit.

To find the low-temperature space group, we hypothesized a space group starting from the parent structure. Considering that we don't see any new peaks appear when lowering the temperature, no translational symmetry breaking occurs in this transition. Hence, there are just two candidate tetragonal subgroups of the $Fm\bar{3}m$ parent structure: I4/mmm (no. 189) and I4/m (no. 87). I4/mmm is reached by a tetragonal distortion of the MBr_6 octahedra, while I4/m in addition allows for a coherent rotation of the MBr_6 octahedra about the tetragonal axis, where $BiBr_6$ and $AgBr_6$ octahedra rotate in opposite senses. Therefore I4/m permits both deformations and rotations of the octahedra, while I4/mmm allows only the deformation of the octahedra. Because I4/m is a subgroup of I4/mmm, the atomic displacements allowed in I4/mmm are also allowed in I4/m; hence, we can refine the crystal structure using the I4/m space group, and assess a posteriori whether the additional symmetry lowering is justified. A Rietveld refinement was performed using a I4/m crystal structure model against neutron powder diffraction data at 30 K, obtaining an excellent agreement, as shown in panel b of Figure 4.8. The structural information are reported in the first column of Table 4.2.

With respect to the cubic phase, the $AgBr_6$ octahedra underwent a tetragonal distortion of r_x/r_{xy} = 1.009 ± 0.008, and the $BiBr_6$ octahedra one of 1.007 ± 0.009 (where r_{xy} and r_z represent the bond lengths between Ag/Bi and Br in the plane and along the c axis, respectively). At the same time, the octahedra in the tetragonal phase rotate by θ = (6.75 ± 0.15) ° in respect to the cubic one. From these results we deduce that the primary distortion below T_S is the octahedral rotation, and the tetragonal elongation is negligible, confirming the choice of the I4/m space group.

4.3.5 Tetragonal strain

It is well known that lattice parameters determined from the XRD data can be used to derive spontaneous strains. The strain arising at the phase transition is expected to provide insights into the nature and mechanisms of the phase transition. Therefore, the spontaneous tetragonal strain has been calculated from the XRD data, following the formula:

$$\sigma = \frac{2(a-c)}{(a+c)} \tag{4.4}$$

and is shown in Figure panel d of Figure 4.5. It obeys a linear relationship reasonably well near the phase transition, while departing from it markedly at low temperatures.

For octahedral tilting transitions in perovskites, the order parameter is represented by the tilt angle η, which is the octahedral rotation angle (the rotational degree of freedom). The tetragonal strain is expected to vary with η^2 for the $Fm\bar{3}m$ → I4/m octahedral tilting transition. In fact, the spontaneous strain is proportional to either η or η^2 depending on symmetry relations. $\sigma \propto \eta$ for symmetry-breaking strains when σ and η have the same symmetry, and $\sigma \propto \eta^2$ for all other strains [139]. A symmetry breaking strain is a strain which transforms as any irreducible representation of the point group of the high-symmetry phase, other than the identity representation. Non-symmetry breaking strains transform as the identity representation and are thus always permitted by symmetry. Landau theory provides a convenient theoretical framework for the quantitative thermodynamic analysis of materials. The excess free energy can be expressed (in systems in which the order parameter is not itself a strain) in terms of the Landau free energy with the addition of the Hooke's law elastic energy $\frac{1}{2}\sum_{i,k} C_{ik}^0 \sigma_i \sigma_k$ and the coupling energies due to interactions between the order parameter and the strain $\sum_{i,m,n} \lambda_{i,m,n} \sigma_i^m \eta^n$, where *m*, *n* are powers exponents. In our simplified case, where the strain σ is a scalar, the coupling energies will simply be $\lambda\sigma\eta^n$, and we can determine the power exponent n on the basis of symmetry considerations. In fact, the strain components in the energy must obey to symmetry rules: each term must be invariant with respect of all symmetry operations of the space group of the high-symmetry phase. In other words, every term should transform as the identity representation of the space-group of the high-symmetry phase. Then, the relationship between the strain and the order parameter is established by considering the conditions for equilibrium. For detailed calculations, the interested reader may refer to reference [140].

For a practical example considering our system, the high-temperature phase presents some two-fold axes, which are not present in the low-temperature phase. If we consider the transformations of σ and η by rotation by 180° around an in-plane axis, the order parameter η changes sign, while the sign of the strain σ doesn't change. Since all the expansion terms of the free energy have to be invariant under the application of the symmetry operators of the high-temperature phase, the lowest order in σ for the coupling energies has to be $\lambda\sigma\eta^2$.

In the mean-field approximation, η^2 should be linearly proportional to the reduced temperature $t=1-T/T_s$. More generally, the order parameter should follow the relation $\eta = t^\beta$, with the critical exponent $\beta = 1/2$ in the mean field. The $Fm\bar{3}m$ → I4/m phase transition is allowed to be second order, even though the possibility of a weak first-order phase transition cannot be completely excluded. In fact, it is in general very difficult to determine

β with any accuracy. With further data available, we will discover in Chapter 6 that the transition is actually close to a tricritical point.

4.4. Discussion

In this Chapter we explored the structural properties of $Cs_2AgBiBr_6$ double perovskite. The structure is cubic at room temperature, with space group $Fm\bar{3}m$, in agreement with previous reports [117]. The Ag-Bi cations are ordered on the B site, as in a rock-salt structure. Our fittings demonstrated excellent quality of the synthesized single crystals. Moreover, the solution-processed powder samples present high crystallinity with a ~20% amount of impurity phases.

With the use of temperature-dependent heat capacity, XRD and neutron diffraction measurements, we discovered and analysed the presence of a low-temperature phase. This phase is tetragonal, with space group I4/m.

5. Optical properties of $Cs_2AgBiBr_6$ double perovskite

The work presented in this chapter has been published in:

Schade, L.; Wright, A. D.; Johnson, R. D.; Dollmann, M.; Wenger, B.; Nayak, P. K.; Prabhakaran, D.; Herz, L. M.; Nicholas, R.; Snaith, H. J. and Radaelli, P. G "Structural and Optical Properties of $Cs_2AgBiBr_6$ Double Perovskite" *ACS Energy Lett.* **2019**, 4, 1, 299-305.

DOI: 10.1021/acsenergylett.8b02090

Direct link: https://doi.org/10.1021/acsenergylett.8b02090

Reproduced with permission from ACS Energy Lett. 2019, 4, 1, 299-305. Copyright 2019, American Chemical Society.

And in:

Zelewski, S. J.; Urban, J. M.; Surrente, A.; Maude, D. K.; Kuc, A.; Schade, L.; Johnson, R. D.; Dollmann, M.; Nayak, P. K.; Snaith, H. J.; Radaelli, P.; Kudrawiec, R.; Nicholas, R. J.; Plochocka, P. and Baranowski, M. "Revealing the Nature of Photoluminescence Emission in the Metal-Halide Double Perovskite $Cs_2AgBiBr_6$" *J. Mater. Chem. C* **2019**, 7, 8350-8356.

DOI: 10.1039/C9TC02402F

Direct link: https://doi.org/10.1039/C9TC02402F

Reproduced with permission from. J. Mater. Chem. C, 2019,7, 8350-8356. Copyright 2019, Journal of Materials Chemistry C.

5.1 Context and summary

In the previous Chapter we have described the structural properties of the $Cs_2AgBiBr_6$ double perovskite at room temperature and revealed the presence of a structural phase transition at $T_s \sim 122$ K between the room-temperature cubic structure ($Fm\bar{3}m$) and a new low temperature tetragonal one (I4/m). In this Chapter, we will focus on the optical properties of this material as a function of temperature, and particularly on how they relate to the structural properties.

$Cs_2AgBiBr_6$ is an indirect band gap semiconductor with an absorption edge in the range 1.8-2.2 eV [23], [117], [141]. When this work was performed, the charge carrier dynamics of this compound had already been explored with different techniques [142], [143]. In spite of these effort, very little was known about the relationship between the structural and optical properties and in particular about the direct band gap transition, which was originally predicted to be at the X-point and 0.7 eV higher than the indirect band gap [141] and it is visible as a sharp absorption peak at about 2.8 eV, typical of two-particle transitions. This is the dominant feature in the absorbance and reflectivity of thin films [143], nanocrystals [144], and bulk crystals [117].

Understanding structure-property relations in this model structure is highly relevant for materials that are already known to have higher efficiencies, as they have closely related crystal structures, and for guiding the design of future compounds. For example, the well-known $MAPbI_3$ compound undergoes ferro-elastic phase transitions that are closely related to $Cs_2AgBiBr_6$, and crystallizes in a distorted phase at room temperature [145]. Therefore, understanding structure-property relations is important to facilitate a rational design of better halide PV materials.

Reflectivity measurements allowed us to establish the temperature dependence of the excitonic transition at the direct band gap, which we then fitted to find a linear relationship with the tetragonal strain. This demonstrated that the direct gap is primarily controlled by MBr_6 octahedral rotations that characterize the tetragonal phase. On the base of photoluminescence measurements, we evidenced the presence an additional fast charge-carrier recombination mechanism at temperatures lower than the tetragonal phase transition, which is suppressed in the cubic phase and might be associated with strain at tetragonal boundaries.

The photoluminescence emission in $Cs_2AgBiBr_6$ is strongly influenced by the strong electron-phonon coupling present in this material. In a last Section, we describe how the PL emission can be related to a colour centre, rather than to a band-to-band transition. Nevertheless, there isn't clear consensus in the literature, and further studies need to be considered to gain a wider prospective on the topic. A brief analysis of the spread in research opinions is presented in the final Discussion.

5.2 Experimental details

Reflectivity measurements and analysis were performed by Dr. Markus Dollman. An Ocean Optics HL-2000-FHSA halogen white light source was directly coupled into a fibre leading to the sample. To account for the background in the signal caused by reflections due to the setup and the fibre, all reflectivity measurements were divided by a reference measurement. This method effectively removed all noise and left the reflectivity signal coming from the sample unchanged.

The temperature dependent PL measurements and analysis have been performed by Dr. Adam Wright. The samples were mounted in a gas-exchange helium cryostat, and PL spectra and transients were taken as the sample was heated over temperatures from 4 to 295 K in increments of between 5 and 25 K. A laser intensity of 62 W cm^{-2} was used when obtaining the PL spectra, and a fluence of 210 nJ cm^{-2} for the PL transients. To measure the reflectance and transmittance spectra, an FTIR spectrometer was used, configured with a tungsten halogen lamp illumination source, a CaF_2 beam-splitter and a silicon detector. The samples were mounted in a gas-exchange helium cryostat.

5.3 Results

5.3.1 Direct gap energy and bond angles

Reflectivity measurements were performed on single crystals of $Cs_2AgBiBr_6$ double perovskite as described in Section 5.2. As shown in panel a of Figure 5.1, we observe that the predominant feature in the spectrum is a dispersive edge, characteristic of a band-edge, free-carrier excitonic absorption, which strengthens rapidly and narrows with decreasing temperature.

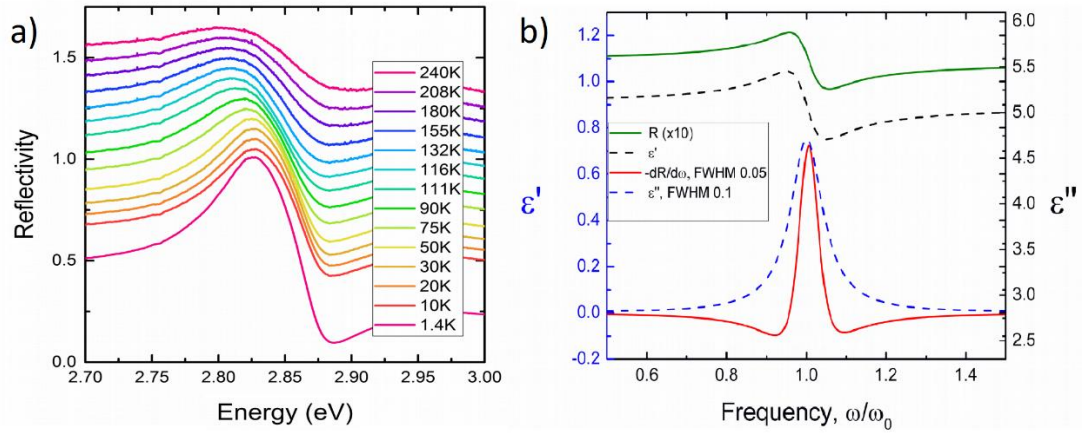


Figure 5.1 a) temperature-dependent reflectivity data and b) modelled frequency (Energy) response of a typical absorption resonance showing the dependence of the real and imaginary components of the dielectric function, the reflectivity, R and its derivative.

Panel b of Figure 5.1 shows the real and imaginary parts of the dielectric function as a function of reduced frequency. In the same graph, we plotted the reflectivity R and its derivative dR/dω of a thick crystal. The similarity between the plots demonstrates that the derivative plot shows a peak which is close to the original resonance, with a FWHM (full width at half maximum) of approximately half of the original dielectric function. This means that, using an approximation of the Kramers-Kronig relations, the negative energy derivative of the reflectivity (-dR/dE), produces peaks at almost exactly the energies of the resonant absorption and improves the spectral resolution.

For this reason, we fitted the peaks in Figure 5.1b) to the real part of the linear susceptibility χ using the relation:

$$R = \sum_j A_j \frac{E_j^2 - E^2}{\gamma_j^2 + \left(E^2 - E_j^2\right)^2} \tag{5.1}$$

where Aj, Ej, and γ_j are the amplitude, resonance energy and broadening parameter for any resonances present.

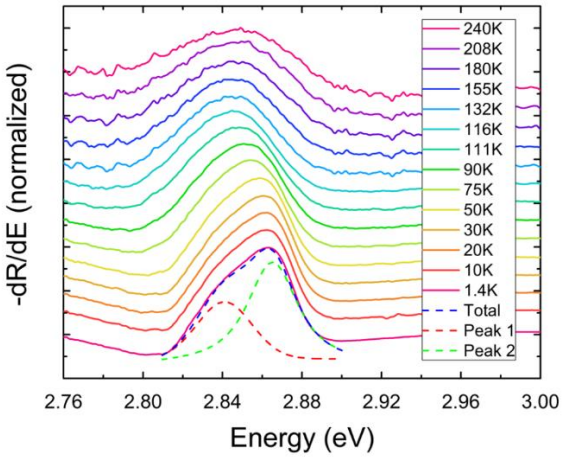


Figure 5.2 Temperature dependence of normalized differential reflectivity (−dR/dE). The data are scaled for a better visualization. The lowest-temperature spectrum has been fitted with two peaks shown by the dashed lines, which have the same line width, an intensity ratio of 2:1, and a splitting of 25 meV.

As shown in Figure 5.2, the peak narrows and shifts with temperature. By 1.5 K the full width at half maximum is only 30 meV (corresponding to a spectral broadening of 60 meV), allowing for a higher accuracy in the measurement of the interband excitonic transition energy E_{ex}. The analysis of these reflectivity peaks has been performed by Dr. Markus Dollman. We combined his extrapolated data with our calculated spontaneous strain values, and the findings are shown in Figure 5.3.

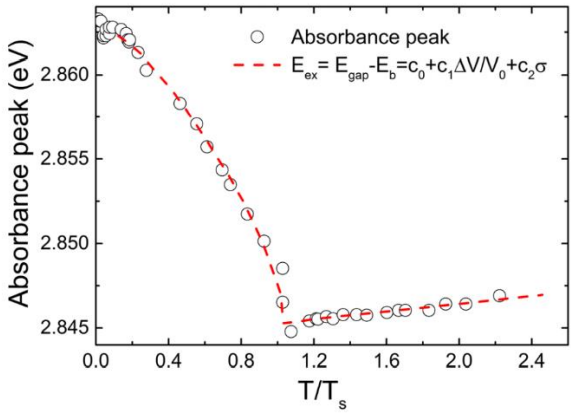


Figure 5.3 Absorbance peak values (empty circles) plotted as a function of the reduced temperature and fitted with Equation 5.2 (dashed line). The fit demonstrates the linear relationship between the increase in exciton energy in the tetragonal phase and the tetragonal strain.

The dashed line in the figure is a model constructed based on the strain data in Figure 1d and assuming the following functional relation:

$$E_{ex} = E_{gap} - E_b = c_0 + c_1 \frac{\Delta V}{V_0} + c_2 \sigma \tag{5.2}$$

where E_{ex} is the exciton energy, E_{gap} is the direct energy gap, E_b is the exciton binding energy, V is the unit cell volume, and σ is the spontaneous strain from the data in Figure 4.5. The model is in excellent agreement with the data, and it was constructed assuming that E_b is independent of temperature, while E_{gap} is controlled by and proportional to the electronic bandwidth W in the temperature range we probed. Two parameters are controlling the bandwidth: the B-X bond length d, which increases monotonically with temperature, and the B-X-B' bond angle θ, which is related to the octahedral rotation (the order parameter η) as $\theta + 2\eta = \pi$, as shown in Figure 5.4.

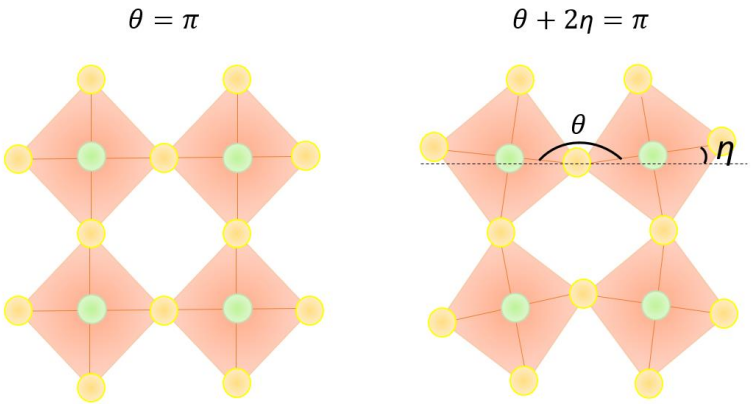


Figure 5.4 Schematic representation of the angles η and θ in the distorted perovskite structure.

We denote the gap energy ΔE_g as the change in gap energy from the hypothetical undistorted perovskite ($\theta = \pi$), d_0 and V_0 as the zero-temperature M-X bond length and volume respectively, and γ as the appropriate exponent for the bond length. The gap energy will then be:

$$\Delta E_g = \tilde{c}_1 \left(d^\gamma - d_0^\gamma\right) + \tilde{c}_2 (cos\theta + 1) \tag{5.3}$$

The first term of Equation 5.3 relates to the change in bond length M-X, while the second term is related to the octahedral rotation change. When we expand the two terms, we obtain:

$$\Delta E_g \approx \tilde{c}_1 d_0^\gamma \frac{\gamma}{3} \frac{\Delta V}{V_0} + 2\tilde{c}_2 \eta^2 \tag{5.3}$$

which is equivalent to equation 5.2.

From Figure 5.3, we can notice that changes in the exciton energy are largely dominated by bond angles rather than bond distances. In fact, determining the values of c_1 and c_2 from the fitting we obtain:

$$c_1 \approx 0.16\ eV, \qquad c_2 = 1.01 \pm 0.02\ eV \tag{4.4}$$

This demonstrates that c_1 is small in comparison with c_2, meaning that the octahedral tilting has the main influence on the energy. A change in band gap of ~1 eV has also been observed by Stoumpos and Kanatzidis [146] for the family of $APbI_3$ compounds where θ varies from π to π/2 in a sequence of different crystal structures, while the dominant role of the M-X-M' angle on the band gap changes has been discussed for the tin-iodide perovskites [147].

In Figure 5.2, we notice that at the lowest temperatures the spectra present an unresolved splitting of ~25 meV into two peaks with an intensity ratio 2:1. This could be consistent with a strain-induced lifting of the X band gap degeneracy. In fact, in case of degenerate bands, strain does not only shift the band as a whole, but may also split bands as a result of partial or complete removal of degeneracy upon reduction of symmetry.

5.3.2 Absorption and steady-state PL

Absorption and steady-state PL spectra of a $Cs_2AgBiBr_6$ single crystal are illustrated in Figure 5.5 at 275 K and 25 K. We notice a sharp rise in the absorbance at energies higher than 2.2 eV, which redshifts continuously with increasing temperature. The same rise has been previously associated with an indirect bandgap [141], [143]. The absorption spectrum has therefore been fitted with the functional form ~$(E-E^i_g)^2$, consistent with an indirect bandgap whose onset correlates well with the values of the PL peak maxima.

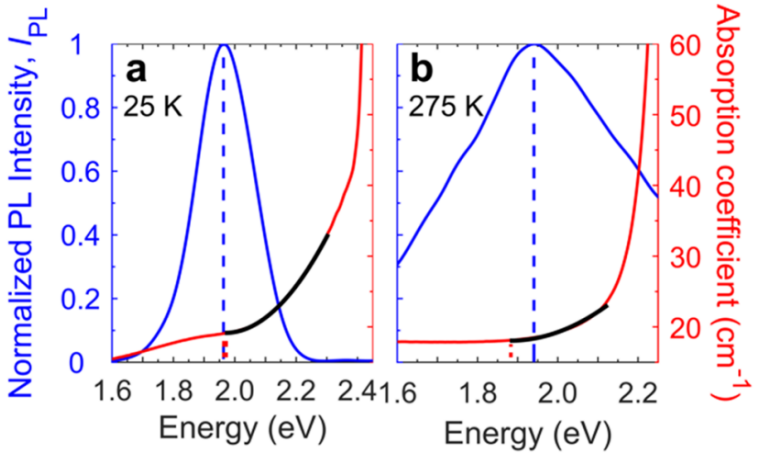


Figure 5.5 Photoluminescence and absorbance measurements. Steady-state PL (solid blue line) and absorption coefficient (solid red line) at 25 K (a) and 275 K.

This agrees with the consensus, at the time of this study, that the PL could be assigned to recombination across the indirect band gap, although a defect-assisted pathway was also proposed [142]. The value of the indirect gap at room temperature (1.87(3) eV) is within the range of those previously reported in the literature (between 1.83 and 2.25 eV) [148] and increases to ~1.97 eV at 25 K. We note that this direction of band gap change with temperature is opposite to that usually observed for lead and tin halide perovskites but the same as that observed for most conventional semiconductors, such as Si and GaAs [149].

Steady-state photoluminescence (PL) measurements were collected between room and low temperatures with an excitation wavelength of 398 nm. As shown in Figure 5.5, at 25 K, we observe the presence of a PL peak at ~1.97(1) eV, i.e., ~0.9 eV below the exciton energy, with a FWHM of ~0.2 eV. We observe only a weak dependence of the PL peak position with increasing temperature, while the peak width increases to ~0.6 eV at room temperature. Unsurprisingly, the indirect bandgap PL is weak, as observed already before [142]. The PL peak energies correlate well with the values of E^i_g estimated from the quadratic fits to the absorbance spectra.

5.3.3 Time-resolved photoluminescence

The PL transients at the peak PL emission energy were measured using TCSPC, as detailed in the experimental Section, to characterize the temperature dependence of charge-carrier recombination mechanisms in $Cs_2AgBiBr_6$ single crystals. The transients are shown in Figure 5.6. At temperatures up to the phase transition T_s, we can notice the presence of two different channels for the PL decay: a very fast component, labelled S for “short”, and a very long one, labelled “L”. We can notice that the short component of the decay is only present in the low-temperature tetragonal phase, while the long one is present throughout. At T = 4 K the short decay was modelled with a mono-exponential and has a very short time constant of $\tau_{short} \approx 1$ ns, while the “L” one has a very long time constant, such that it cannot be reliably measured at this temperature. Upon warming, the lifetime of the S component remains much lower than that of the L component, while its overall intensity decreases. By contrast, the decay of the L component becomes faster on warming. Above ~50 K, the L component can be fitted with a stretched exponential, yielding average lifetimes that vary between ~50 μs at 50 K to a few nanoseconds at 200 K and above.

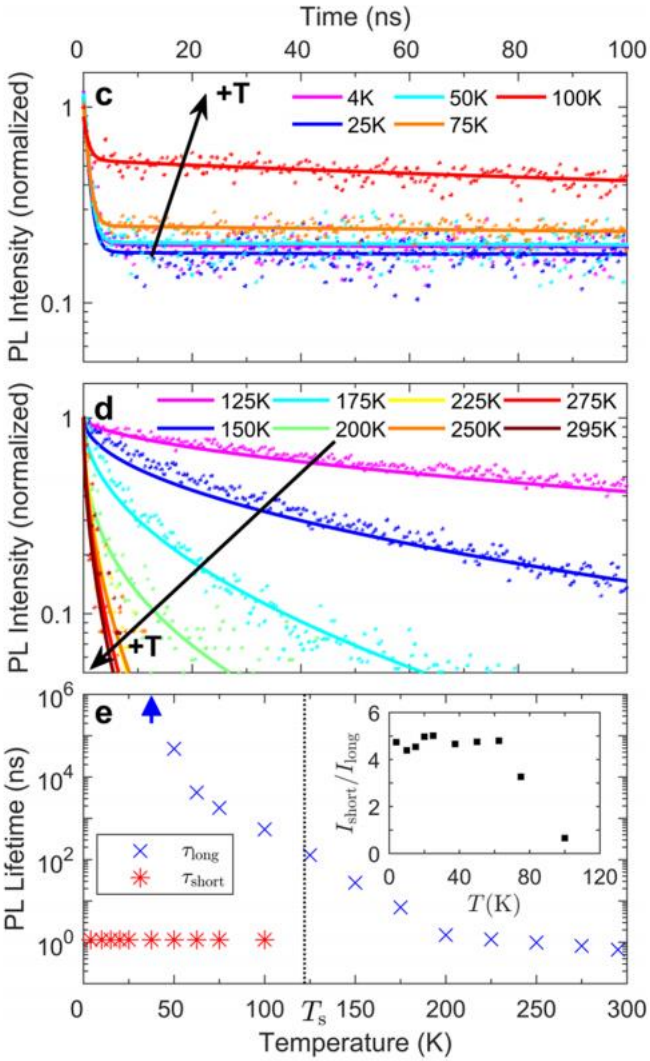


Figure 5.6 c) Dots: PL transients (excitation at 398 nm, fluence 210 nJ cm^{-2}) at temperatures between 4 and 100 K (tetragonal phase). Solid lines: global fits of the sum of a stretched exponential (long) and a monoexponential (short) component, with the lifetime of the latter common between the temperatures. d) Dots: PL transients at temperatures from 125 to 295 K (cubic phase). Solid lines: stretched exponential fits. Black arrows indicate the overall temperature trends. e) Lifetimes of the long (blue) and short (red) components, shown on both sides of the phase transition temperature T_s. Below 50 K, the fitted long component lifetimes exceed the measurement capability of the system, as indicated by the blue arrow. The inset shows the temperature dependence of the ratio between the intensities of the short and long components.

The intensity ratio between S and L is shown in the inset of panel e. When correlated with the structural and reflectivity measurements, these data demonstrate that the S decay channel is present only in the tetragonal phase and that it rapidly becomes weaker as the tetragonal distortion is reduced. Therefore, we can speculate that S is associated with defects concentrating at the twin boundaries, which spontaneously form on cooling through

the phase transition. In this scenario, the onset of the S component doesn't need to correlate precisely with T_s, because a minimum value of twin boundary strain is usually required for the formation of defects. This hypothesis could be verified by repeating the PL measurements on a single crystal cooled under biaxial compressive strain to promote the formation of a single tetragonal domain.

In Figure 5.6, we only show the early time decay (up to 100 ns), for approximately the first order of magnitude reduction in PL signal. Figure 5.7 illustrates a transient PL decay for a $Cs_2AgBiBr_6$ crystal measured at room temperature over a longer time period.

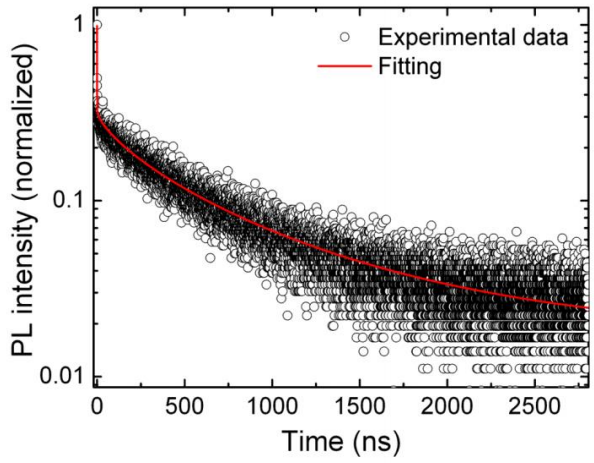


Figure 5.7 Time-resolved photoluminescence from $Cs_2AgBiBr_6$ single crystals. The excitation wavelength used was: 397.7nm, with a fluence of 46 nJ/cm^2.

We can indeed notice that there exists a much longer component of the PL decay at room temperature, in agreement with the literature [23]. This component has been assigned to incredibly long carrier lifetimes in $Cs_2AgBiBr_6$ [23]. However, these lifetimes have been derived from a tail of very low intensity, which can be assigned to trap states depopulation.

To summarize, it appears that there are three components to the PL dynamics. The very fast short decay S, at low temperature, which we interpret to be governed by charge trapping at twinning defects. The longer time decay L, at intermediate temperatures, which is sped up considerably as the temperature increases, likely because of charge trapping where the required emission of phonons becomes faster as the temperature is raised. The third component is the slow decay visible in the room-temperature PL dynamics at long times, which may be governed by the trap states depopulation time rather than the lifetime of the free carriers.

5.3.4 The nature of PL emission

In this Section, we investigate the nature of the photoluminescence emission process in the double-perovskite $Cs_2AgBiBr_6$. All measurements and analysis of data have been performed by our collaborators, we provided the samples for this work.

Since perovskites are ionic crystals [150]–[152], the carriers are expected to strongly couple to lattice vibrations [150]. In particular, the PL emission in $Cs_2AgBiBr_6$ is strongly influenced by a strong electron-phonon coupling. In this section, we will briefly demonstrate that the PL emission may be related to a colour centre, rather than a band-to-band transition.

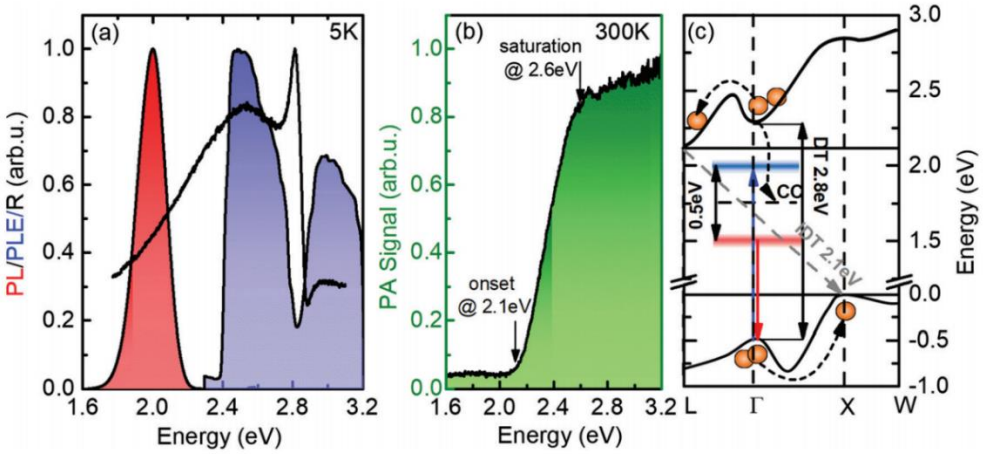


Figure 5.8 a) Low temperature (T=5K) photoluminescence spectrum (PL in red) and integrated PL intensity as a function of the energy of the exciting photons (PLE spectrum in blue) together with the reflectance spectrum (R in black). b) Photoacoustic signal (PAS) as a function of the excitation energy (equivalent to absorption) measured at 300 K. c) Schematic showing the band structure of $Cs_2AgBiBr_6$ with possible transitions and carrier relaxation pathways. The black dashed line indicates the position of colour centres. The blue and red bars represent absorption and emission bands of the colour centre which are broadened and shifted from the energy of equilibrium state of colour centre (dashed line) due to the strong electron-phonon coupling.

Panel a of Figure 5.8 shows the PL (red), photoluminescence excitation (PLE, blue) and reflectance (black line) spectra of $Cs_2AgBiBr_6$ single crystal taken at cryogenic temperature (T=5K). The broadened PL emission peaks has a full width at half maximum (FWHM) of ~190 meV. The PLE spectrum shows that the intensity of the PL emission strongly depends on the energy of the exciting photons. In fact, for excitation below 2.4 eV the PL emission is almost completely quenched, while above 2.4 eV it increases rapidly reaching a maximum at around 2.5 eV, before decreasing slowly at higher energies. The decrease of the PLE spectrum occurs at around 2.8 eV, which corresponds to the direct band gap exciton feature present in the

reflectance spectrum (black line in the same panel). Usually, band-to-band transitions show a monotonic increase [136], following the increase of the density of states of the bands, and eventually saturating for strong enough absorption. At the same time, panel b in Figure 5.8 shows the photoacoustic absorption spectrum, which presents a monotonic increase and saturation at about 2.6 eV. This monotonic increase in the absorption spectrum is also reported in [23], [24], [143]. Moreover, we highlight again the large Stokes shift between emission and absorption, which sets the onset of the PLE at hundreds of meV higher than the reported band gap of $Cs_2AgBiBr_6$.

The non-monotonic behaviour of the PLE signal indicates that the observed PL emission is not related to a band-to-band transition, but its origin can be attributed to a colour centre, which can be excited by 2.5 eV photons.

In ionic crystals colour centres are usually strongly coupled to the crystal lattice vibrations [150]. The occupation of the colour centre causes a local lattice deformation, which leads to an energy offset between the ground and excited state of the colour centre. When radiative recombination occurs, multiple photons are emitted [88], [150]. This causes the broadening of the absorption and emission bands, with a strong Strokes shift (in this case of ~500 meV). These features are indicative of a strong electron-phonon interaction. The Huang-Rhys factor, which is the average number of phonons emitted by the colours centre after photon absorption or emission, has been calculated to be ~11.7.

5.4 Discussion

The relationship between the structural and optical properties of the $Cs_2AgBiBr_6$ double perovskite has been highlighted in this Chapter. In particular, we found that some optical properties are quite dramatically affected by the structural phase transition at low temperature that we analysed in Chapter 3 (cubic $Fm\bar{3}m$ → tetragonal I4/m). In fact, the exciton energy extracted from our reflectance measurement, and the corresponding band gap energy, increase in the tetragonal phase by as much as 20 meV. Moreover, the excess energy scales linearly with the tetragonal strain, strongly suggesting that the direct band gap is controlled by the *B*Br_6 octahedral rotation. Our time-resolved PL measurements demonstrate that the charge carrier lifetimes are also affected by the structural transition, with a fast relaxation channel being present mainly in the tetragonal phase. We assigned this channel to be linked to defects at tetragonal twin boundaries. $Cs_2AgBiBr_6$-based solar cells show poorer photocurrent and photovoltage compared to the Pb-halide-based solar

cells, possibly because of the trapping of charge carriers and subsequent nonradiative recombination. Our findings suggest that the formation of twinning boundaries can reduce the charge carrier lifetime. It is likely, therefore, that grain boundaries in polycrystalline thin films could also affect the charge carrier behaviour. As a consequence, further device improvement could be expected via better management of grain boundaries.

We noticed that $Cs_2AgBiBr_6$ double perovskite presents a large Stokes-shift between absorption and emission spectra. In the collaborative work presented in the sub-Section 5.3.4, we demonstrated that the photoluminescence emission in this double perovskite is strongly influenced by a strong electron-phonon coupling, as a Franck-Condon model resulted in a Huang-Rhys factor of S=11.7. A combination of PLE, PL and reflectance measurements suggested that the PL emission is related to a colour centre rather than to a band-to-band transition. This conclusion might be of high importance in the study of these materials, since in literature there has been no homogeneous consensus on the origin of the PL. We will summarize here briefly some of the different findings on the topic.

Filip. et al. [141] assigned the photoluminescence peak in $Cs_2AgBiBr_6$ to a phonon-assisted recombination across the indirect band gap, and the leading edge of the optical absorption onset to a direct band gap. At the same time, they stated that defects or excitonic effects could play a role in the PL features. Bartesaghi et al. [143] excluded substantial exciton formation in this material, and they stated that free charges recombine via band-to-band recombination, or via surface states. Hoye et al. [142] suggested that the recombination process happens via sub-band gap states rather than across the indirect band gap.

Very recently (March 2021), Wright at al. [153] published a manuscript which strengthens the conclusions reported in sub-Section 5.3.4. In fact, their findings suggest that strong electron-phonon coupling in $Cs_2AgBiBr_6$ induces rapid charge-carrier localization. In particular, an ultrafast, barrier-free localization of free carriers to an intrinsic small polaronic state seems to be present. The self-trapped charge carriers diffuse to colour centres, causing a broad emission that is strongly red-shifted from a direct band gap edge. The intrinsic self-trapping of charge carriers might intuitively suggest that this material is not an ideal candidate for photovoltaic or optoelectronic applications, since these rely on the high mobilities of charge carriers. Nevertheless, Wright et al. note that the self-trapping is less severe at room temperature, because temperature-activated hopping processes lead to a relatively benign reduction in charge carrier mobilities. In fact, the mobilities of localized and delocalized states exceed about 1 $cm^2V^{-1}s^{-1}$. Other works [154], [155] have described

$Cs_2AgBiBr_6$ as an electronically quasi-0D perovskite. The lower electronic dimensionality leads to low energy barriers between free and self-trapped states, making the polaron formation very likely to happen [156].

6. Structural properties of $Cs_2AgBi_{1-x}In_xBr_6$ double perovskite

The work presented in this chapter has been published in:

Schade, L.; Mahesh, S.; Volonakis, G.; Zacharias, M.; Wenger, B.; Schmidt, F.; Kesava, S. V.; Prabhakaran, D.; Abdi-Jalebi, M.; Lenz, M. "Crystallographic, Optical, and Electronic Properties of the $Cs_2AgBi_{1-x}In_xBr_6$ Double Perovskite: Understanding the Fundamental Photovoltaic Efficiency Challenges." *ACS Energy Lett.* **2021**, *6*, 1073– 1081.

DOI: 10.1021/acsenergylett.0c02524

Direct link: https://pubs.acs.org/doi/10.1021/acsenergylett.0c02524

Reproduced with permission from ACS Energy Lett. 2021, 6, 1073-1081. Copyright 2021, American Chemical Society.

6.1 Context and summary

In the past Chapter, we have explored the structural and optical properties of the $Cs_2AgBiBr_6$ double perovskite. Despite some promising optoelectronic properties, the efficiency obtained to date for this material employed as the absorber layer in solar cells is still very low (2.2%) [25], and it is unclear if it will be able to match the efficiencies of lead halide perovskite solar cells. For this reason, the discovery of new materials with complementary and improved properties is essential for the field of perovskite solar cells. The optical properties and the stability of perovskite materials can be significantly influenced by external conditions, such as applying high temperature or pressure, but also via chemical alloying [157]. With this approach, Du et al. [158] engineered the band gap of the $Cs_2AgBiBr_6$ double perovskite using trivalent metal alloying with In^{III} and Sb^{III}, finding that the first enhances the PL intensity, while the second induces a substantial decrease of the PL emission. Furthermore, Luo et al. [159] have demonstrated extremely high photoluminescence quantum yield and electroluminescence efficiency for $Cs_2AgInCl_6$ when substituting Ag^{I} for Na^{I} and doping with small concentrations of bismuth. It is clear that the investigation of the properties of new materials is essential for the optimization of the absorber layer in solar cells. In this Chapter, we focus on the structural properties of

$Cs_2AgBi_{1-x}In_xBr_6$ double perovskite, which proves to be an interesting candidate for PV application.

We synthesized single crystals of $Cs_2AgBi_{1-x}In_xBr_6$ double perovskite for the first time with excellent quality, with compositions up to ~25% indium at the B' site. Polycrystalline powders were synthesized with up to ~60% indium content. In addition, we prepared high-quality double perovskite thin films with a range of indium content.

Using variable-temperature single-crystal/powder X-ray diffraction (XRD) and heat capacity measurements, we discover that the low-temperature cubic-to-tetragonal phase transition, described in Chapter 3 of this thesis, shifts to lower temperatures as indium is added to the structure. We determine the amount of indium present through XRD structural characterization and further confirm the values with inductively coupled plasma mass spectrometry (ICP-MS). The structural characterization of this material is an essential step to be able to fully investigate the nature of its optoelectronic properties.

6.2 Experimental details

Experimental details for the main measurements performed in this Chapter are described in Chapter 2. Inductively coupled plasma mass spectroscopy (ICP-MS) was performed by Dr. Marios Zacharias. For ICP-MS measurements, crystals (5-15 mg) were dissolved fully in concentrated HBr including 30min sonication treatment. Samples were then appropriately diluted with milliQ water (18.2 MΩcm). Quantification was carried out using an external calibration from single-element standards (Sigma-Aldrich) prepared in milliQ water (18.2 MΩcm) from 0-50 µg/L, matrix matched to the corresponding HBr amount. Analysis was carried out using an Agilent 8800 ICP-QQQ-MS system on 115In+ and 209Bi+ using helium as a collision gas (5 mL/min). 103Rh+ was used as an internal standard to account for possible matrix effects. We decided to use the ICP-MS values as our final percentages throughout this Thesis, as they are more precise.

6.3 Results

For clarity, in our figures we will present the data measured on single crystals in red, on polycrystalline powders in green, and on thin films in blue.

6.3.1 Samples and indium content

We synthesized the $Cs_2AgBi_{1-x}In_xBr_6$ single crystal, powders and thin film samples as described in the experimental Chapter (Chapter 2). We prepared 5 different alloyed crystals in addition to the neat Bi double perovskite (SC0): SC1, SC7, SC12, SC17 and SC25 with ~1%, 7%, 12%, 17% and 25% of indium, respectively. The percentages indicate the amount of indium on the bismuth site and refer to the compositions of the as-synthesized crystals, which we deduced from ICP-MS. The values have been compared with the percentages obtained with the use of XRD (the refinements are discussed in the next section) and are shown in Table 6.1.

%In in solution	%In (ICP-MS)	%In (XRD)
0	0.00208 ± 0.00388	0
1	1.18 ± 0.03	1 ± 4
5	7.25 ± 0.38	1± 2
10	12.1 ± 0.3	10 ± 3
15	17.0 ± 0.9	12 ± 2
20	25.4 ± 0.4	21 ± 3
50	25.1 ± 0.3	23 ± 2

Table 6.1 Indium percentage in single crystals determined by ICP-MS and XRD, in comparison with the starting percentage of indium that has been added to the starting solution.

We prepared five polycrystalline samples with different indium concentrations all the way up to 60% indium substitution, once again confirmed by ICP-MS (values in Table 6.2).

%In precursors	%In (ICP-MS)	%In (XRD)
0	0.0120 ± 0.0325	0
10	10.1 ± 0.2	0.31 ± 0.1
40	35.9 ± 0.5	40.4 ± 1.2
50	45.2 ± 0.5	53 ± 1.5
60	59.3 ± 0.9	70 ± 1.8

Table 6.2 Indium percentage in powders extrapolated by inductively coupled plasma mass spectroscopy (ICP-MS) and XRD, in comparison with the starting percentage of indium in the precursors powders.

Similarly to the single crystals, we will denote the powder samples according to their indium content: PW0, PW10, PW35, PW45 and PW60. We will also denote the thin films TF0, TF10, TF35, TF45 and TF60 in relation to the percentage of indium obtained from the ICP-MS measurement of the precursor powders. The thickness of the films was measured with the use of a DektakXT Stylus profiler and is reported in Table 6.3. The thickness decreases with increasing percentage of indium because the solubility of the starting solution decreases when indium is added, so the molarity was slightly different for each sample.

Thin film	Thickness (nm)
TF0	142 ± 10
TF10	167 ± 10
TF35	180 ± 10
TF45	200 ± 10
TF60	280 ± 10

Table 6.3 Thicknesses of each thin film of $Cs_2AgIn_xBi_{1-x}Br_6$ for each indium percentage.

6.3.2 Room temperature structural characterization

- Single crystals

The results of the XRD-fittings on $Cs_2AgBi_{1-x}In_xBr_6$ single crystals are shown in Figure 6.1. The F^2_{calc} parameters almost perfectly coincide with the F^2_{obs} ones, demonstrating the excellent quality of the crystals. The amount of indium in the labels on the panels refers to the amount of indium present in the starting solution (see Table 6.1 in the previous section). The amount

of indium effectively present in the single crystals has been extrapolated using the refined occupancy parameter, and is reported in the same table.

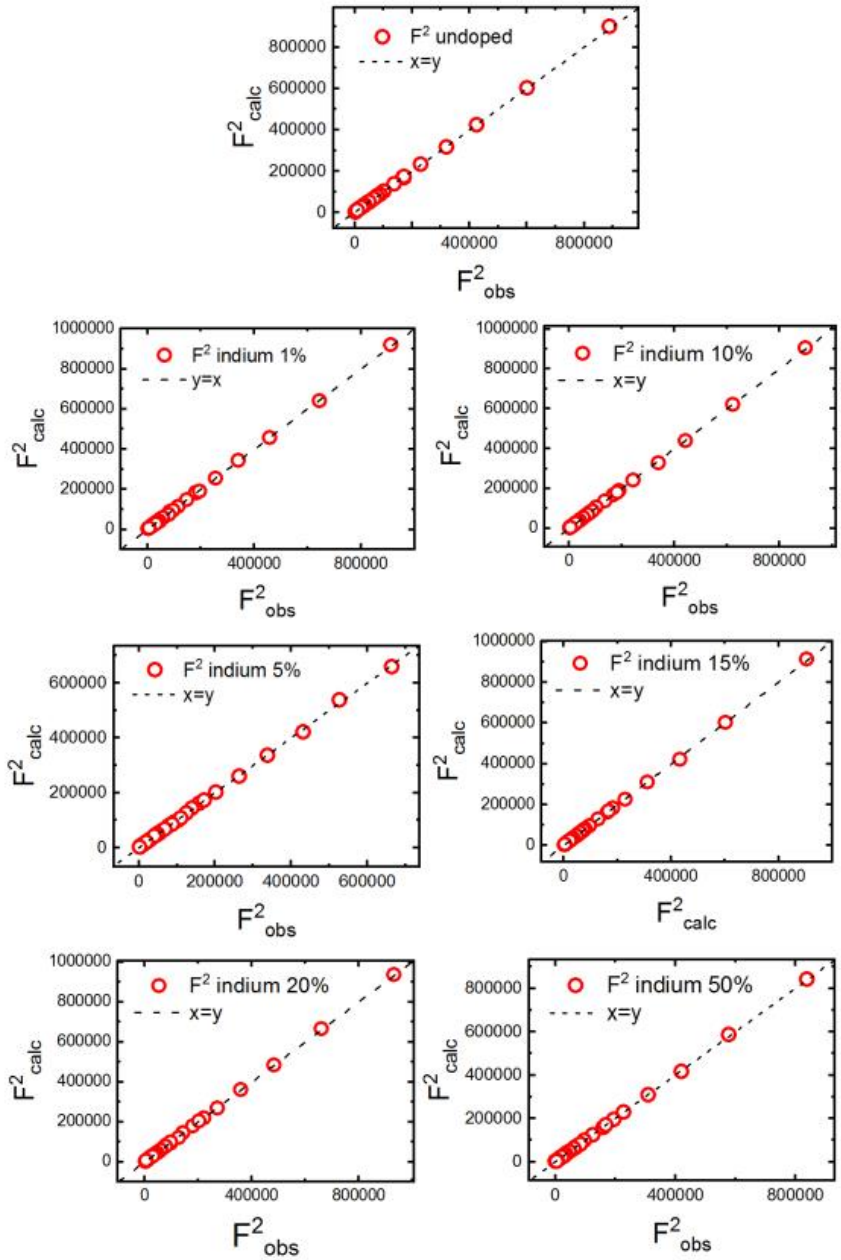


Figure 6.1 Plot of F^2 calc versus F^2_{obs} for the structural refinement of $Cs_2AgIn_xBi_{1-x}Br_6$ single crystals. The black line is a guide to the eye.

x	a (Å)	x(Br)	Occ(In)	R_{int}/R_w
0	11.2741(2)	0.25093(2)	-	5.33/5.07
1	11.26101(1)	0.2508(2)	0.01(4)	9.24/7.13
12	11.2375(3)	0.24988(2)	0.10(3)	7.25/5.82
17	11.2289(2)	0.24971(1)	0.12(2)	4.34/4.26
25	11.20772(1)	0.24885(1)	0.23(2)	4.62/4.54

Table 6.5 Lattice parameters and atomic coordinates from $Cs_2AgBi_{1-x}In_xBr_6$ single crystals fittings. Number in parentheses are statistical errors of the last significant digit. In $Fm\bar{3}m$, the atoms are located at the following Wyckoff positions Cs: 8c(1/4,1/4,1/4) , Bi/In: 4a(0,0,0) , Ag: 4b(1/2,1/2,1/2) , Br: 24e(x,0,0).

The fitting analysis reveals that all samples are cubic at room temperature, consistent with space group $Fm\bar{3}m$, the same as the neat $Cs_2AgBiBr_6$ double perovskite. Moreover, the lattice contracts as the indium cation replaces the smaller bismuth, as we can notice from the lattice parameters in Table 6.5.

- Polycrystalline powders

Powder X-ray diffraction has been performed with the use of Cu-Kα radiation, as described in Chapter 2. Figure 6.2 shows the Rietveld refinements for all the samples. Structural parameters are reported in Table 6.6. We notice the presence of impurity phases in the XRD patterns of PW10, PW35, PW45 and PW60 that we have not been able to characterize. The percentage of indium has been extrapolated using the occupancy of indium also in this case, and then it has been compared with the ICP-MS results as shown in Table 6.2 in the previous Section. Structural information from the Rietveld refinement are present in Table 6.6.

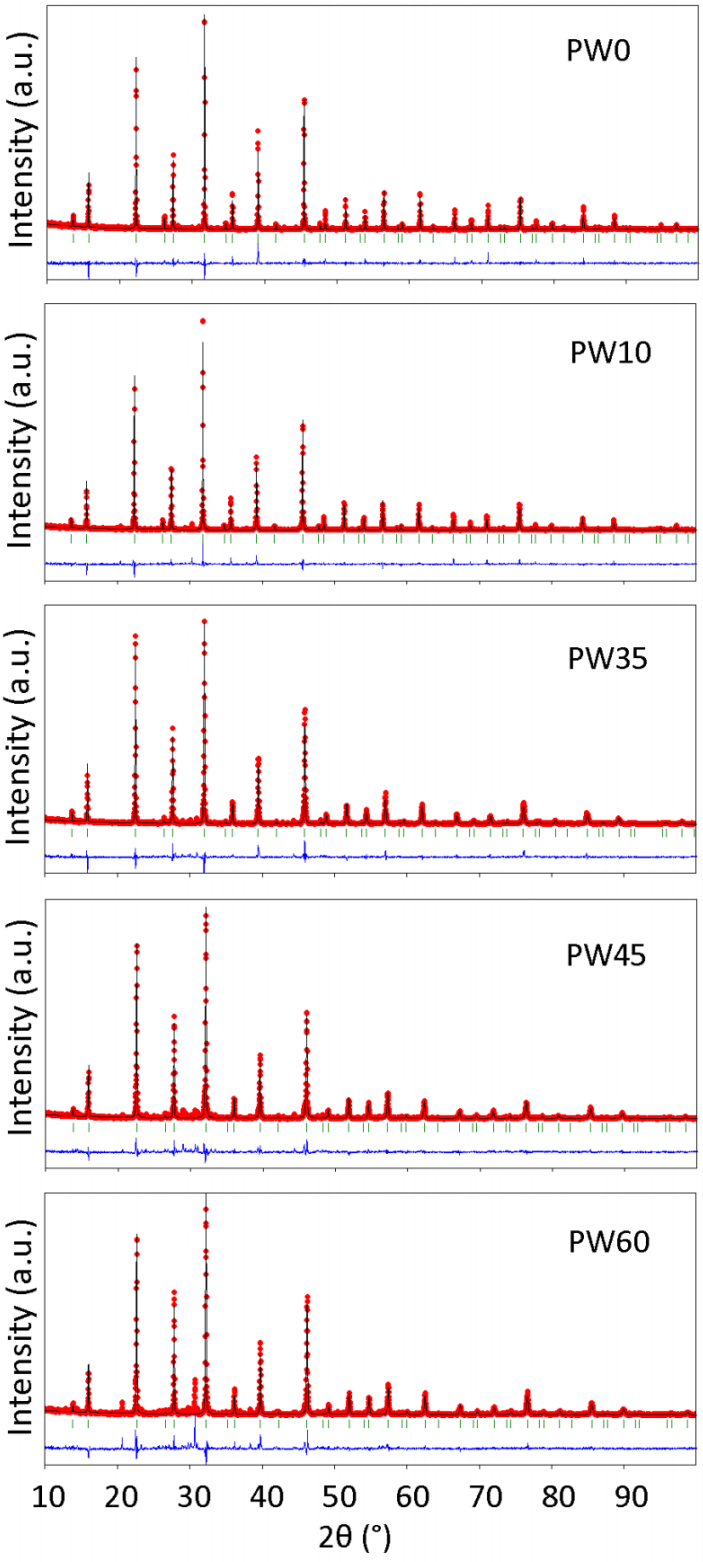


Figure 6.2 X-ray diffraction patterns with Rietveld refinement for the $Cs_2AgIn_xBi_{1-x}Br_6$ double perovskite polycrystalline powders for the different indium percentages. The percentages of indium in the plots refers to the amount of indium in the starting precursors. The red dots represent the experimental points, while the black pattern is the calculated one. The green vertical lines represent the peaks positions, and the blue line shows the residuals.

x	a (Å)	x(Br)	Occ(In)	R_p/R_{wp}
0	11.27245(16)	0.25154(54)	-	16.6/22.1
10	11.25002(14)	0.2510(4)	0.031(10)	14.0/17.9
35	11.1789(3)	0.2487(4)	0.404(12)	13.3/17.7
45	11.1450(3)	0.2473(6)	0.542(15)	13.8/19.6
60	11.1184(4)	0.2456(8)	0.678(18)	15.0/20.1

Table 6.6 Lattice parameters and atomic coordinates from Rietveld refinements of the XRD patterns of $Cs_2AgBi_{1-x}In_xBr_6$ polycrystalline samples. Number in parentheses are statistical errors of the last significant digit. In Fm $\bar{3}$ m, the atoms are located at the following Wyckoff positions Cs: 8c(1/4,1/4,1/4) , Bi/In: 4a(0,0,0) , Ag: 4b(1/2,1/2,1/2) , Br: 24e(x,0,0).

We can notice again that the space group remains invariant for all samples at room temperature, and that the lattice contracts when indium is substituted to the bismuth site. In fact, panel a of Figure 6.3 shows a zoom into the (400) peak for all the powder samples and we can notice a peak shift of all reflections towards higher angles.

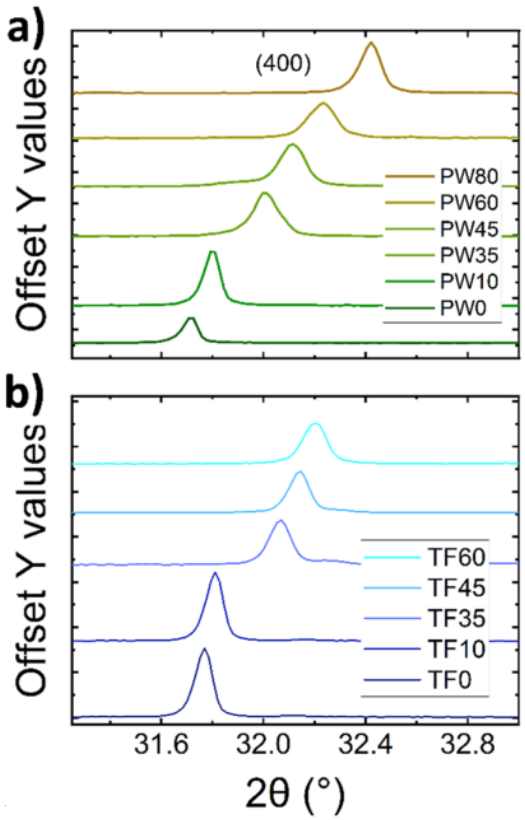


Figure 6.3 XRD patterns in the region of the (400) peak for (a) polycrystalline powders and (b) thin films of the Cs_2AgBi_{1-x}InxBr6 double-perovskite samples.

- Thin films

X-ray diffraction on thin films (deposited on quartz) has been measured using PANalytical X'Pert PRO Diffractometer with Cu-Kα radiation, as in the case of powders. The complete XRD patterns are shown in Figure 6.4. Also in this case, we can notice the shift in peak position (panel b of Figure 6.3) from the zoom on the (400) peak. Looking at Figure 6.3, we can notice a slight mismatch between the peak positions of the thin films and of the polycrystalline powders, which is due to experimental uncertainties in the powder diffractometer (e.g., the refined zero point and the height of the sample in the holder), while the peak positions in the patterns of the thin-film samples have been calibrated to the known peak positions of the quartz substrate. This discrepancy does not affect our conclusion because its effect on the lattice parameters is much smaller than the shift in peak position due to changes in composition.

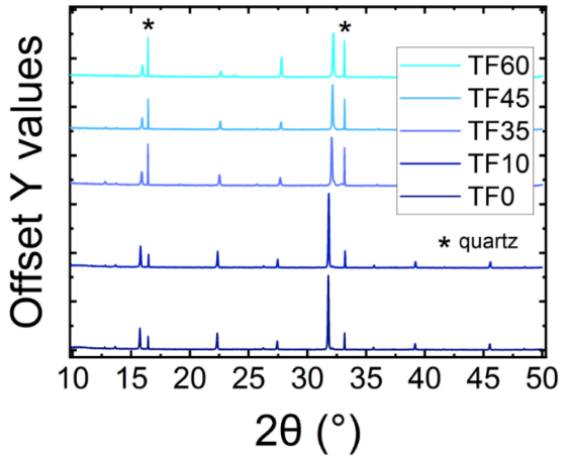


Figure 6.4 X-ray diffraction pattern for the $Cs_2AgIn_xBi_{1-x}Br_6$ thin films for the different indium percentages. The asterisks indicate the quartz peaks.

6.3.3 Phase transition and tricritical point

Temperature dependent heat capacity measurements and XRD were performed to further investigate the impact of alloying indium in the $Cs_2AgBiBr_6$ double perovskite. Figure 6.5 shows the specific heat capacity measured on single crystals SC0, SC17 and SC25. As we have shown in Chapter 3, for $Cs_2AgBiBr_6$ a cubic-to-tetragonal phase transition occurs at ~122 K, which is shown again in panel a of the figure. With the substitution of bismuth with indium, this phase transition temperature monotonically shifts to lower temperature, for instance being at ~110 K for S17 (panel b in Figure 6.5). It also appears that the specific heat anomaly at the transition temperature becomes smoother with increasing indium content, and disappears altogether in the case of SC25, as shown in panel c of Figure 6.5.

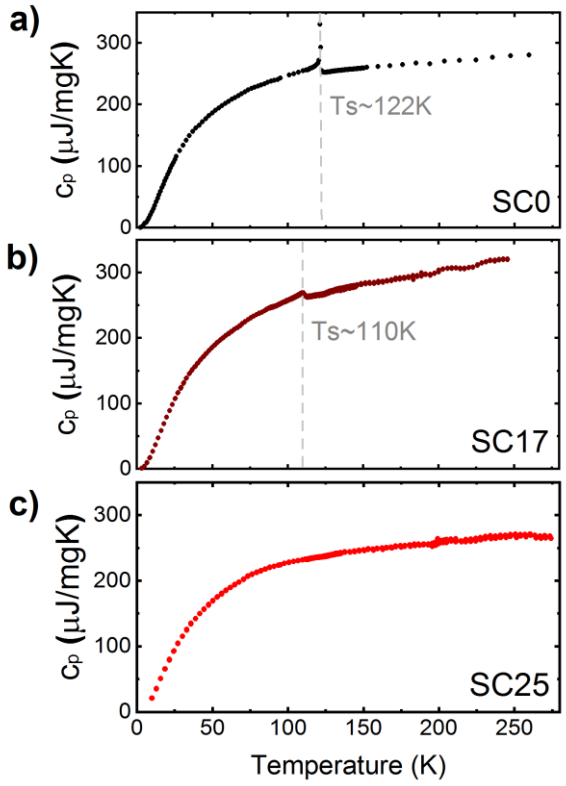


Figure 6.5 specific heat capacity measured on single crystals a) SC0, b) SC17 and c) SC25.

Figures 6.6, 6.7 and 6.8 show the X-ray diffraction pattern in the range of the (400)c peak for the samples PW10, PW35 and PW60 as a function of temperature. The peak splits in two peaks when the temperature decreases, similarly to the behaviour of $Cs_2AgBiBr_6$. The lattice parameters determined from the fit are reported in panels b of Figure 6.6 and 6.7.

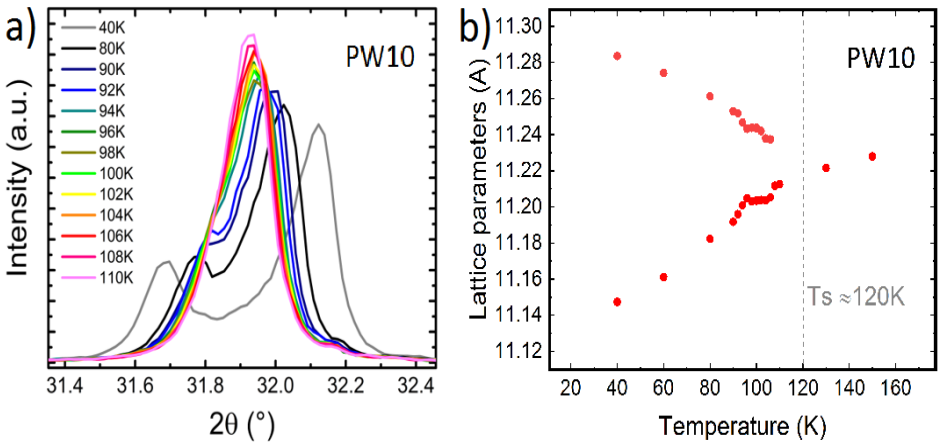


Figure 6.6 a) X-ray diffraction pattern of PWD10 plotted in the range ~ [31.3-32.5] °, where the $(400)_c$ peak of the cubic room-temperature structure is present, in function of temperature. b) Lattice parameters extrapolated from the peaks fitting in function of temperature.

The temperature-dependent X-ray diffraction measurements shown in Figure 6.7 clearly indicate that the transition is still present in the PW35 composition, only shifting to a lower temperature of 60 K.

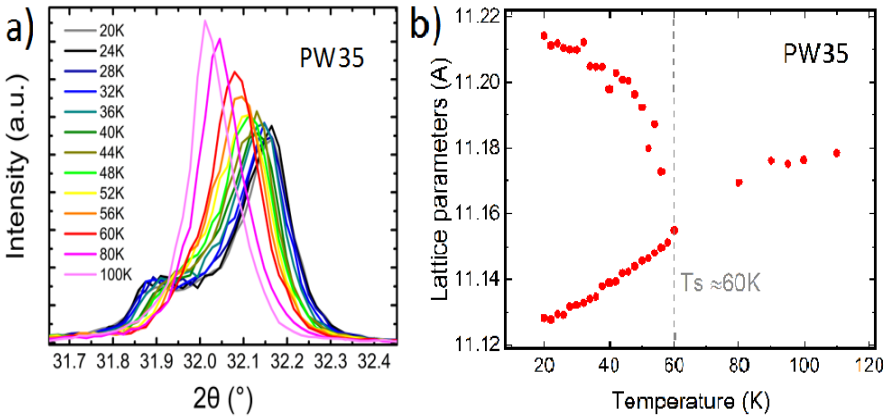


Figure 6.7 a) X-ray diffraction pattern of PWD35 plotted in the range ~ [31.3-32.5] °, where the $(400)_c$ peak of the cubic room-temperature structure is present, in function of temperature. b) Lattice parameters extrapolated from the peaks fitting in function of temperature.

We notice that, in the case of PWD60 (Figure 6.8), there is no sign of peak splitting in the temperature range investigated. This might be due to the fact that the transition might be present at lower temperatures. From our data, we can deduct that the presence of Indium makes the cubic phase more stable. Panel b of Figure 6.8 illustrates the dependence of the transition temperature on the indium concentration, confirming that T_c decreases when Indium is substituted on the Bismuth site.

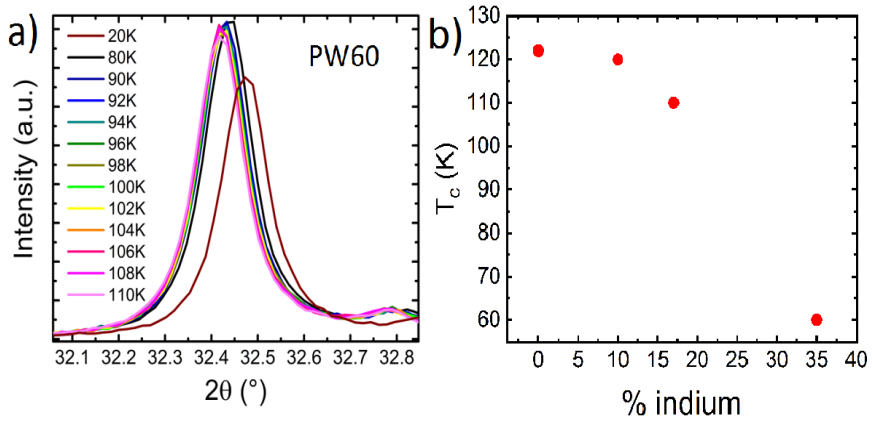


Figure 6.8 a) X-ray diffraction pattern of PWD60 plotted in the range ~ [31.3-32.5] °, where the $(400)_c$ peak of the cubic room-temperature structure is present, in function of temperature. b) Transition temperature T_c in function of indium concentrations. Values are also taken from heat capacity measurements.

The disappearance of the heat capacity singularity at the transition point for higher concentrations of indium can be explained if we classify the transition of the $Cs_2AgBiBr_6$ neat perovskite to be close to a tricritical point, i.e. to the crossover between a first-order and a second order transition. As first proposed by Wruck in 1986 for the $I\bar{1}$-$P\bar{1}$ transition in anorthite (shown in Figure 6.9) [160], disorder can change both the transition temperature and the order of the transition. This leads to the rapid disappearance of the lambda-anomaly in the heat capacity in anorthide samples that have been either heat-treated or contaminated with sodium [160], which instead display a smeared-out stepwise increase of excess heat capacity, as shown in panel b of Figure 6.9. In fact the transition, being initially close to a tricritical point, moves deeper into the second-order regime when sodium is added to the samples, leading to a crossover from a lambda-singularity to a step-singularity.

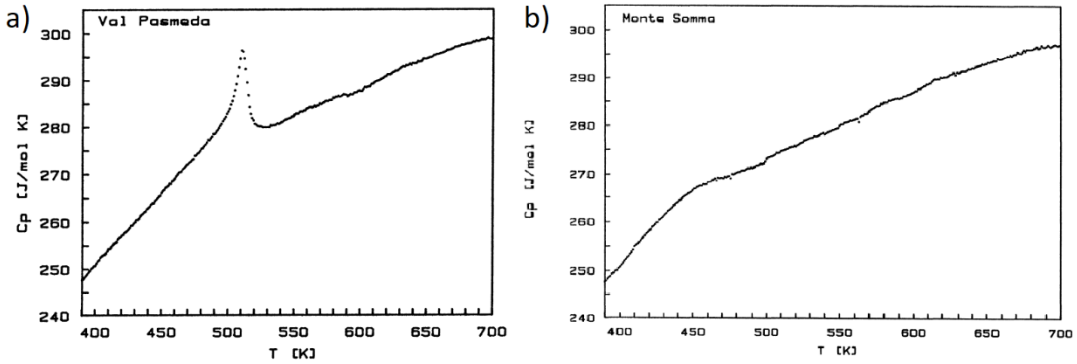


Figure 6.9 a) Specific heat anomaly of the $P\bar{1}$-$I\bar{1}$ phase transition in highly ordered anorthite (Val Pasmeda) and b) the effect of the $P\bar{1}$-$I\bar{1}$ phase transition near 480 K in anorthite. Reprinted from reference [161].

Following the steps detailed in reference [161], we can explain the heat capacity behaviour that we see experimentally in Figure 6.5. As we have seen in Chapter 2, the Landau free energy can be expanded in a polynomial with powers of a one-component, one dimensional order parameter η as:

$$\Delta F = F(P,T,\eta) - F_0(P,T) = b\eta^2 + \frac{1}{2}d\eta^4 + \frac{1}{3}f\eta^6 \qquad (6.1)$$

Where $b=b_0t$ and $t=(T-T_0)/T_0$ is the reduced temperature. We have $d>0$ or $d<0$ depending on the order of the phase transition. At $T=T_0$ the excess entropy will be zero in the case of a second order phase transition, and different from zero in the case of a first-order.

We have calculated the order parameter using the Landau free energy in Chapter 1, and with trivial calculation we find the excess entropy and specific heat:

$$\Delta S = \frac{b_0}{T_0}\eta^2 = \frac{b_0}{T_0}\left[\frac{-d + \sqrt{d^2 - 4bf}}{2f}\right] \tag{6.7}$$

$$\Delta C_p = T\frac{\partial \Delta S}{\partial T} = -T\frac{b_0^2}{T_0^2}\frac{1}{\sqrt{d^2 - 4bf}} \tag{6.8}$$

We will now name the temperature at which $d^2=4bf$ as T_1. T_1 is also the temperature at which $\frac{\partial}{\partial \eta}\frac{\partial \Delta \varphi}{\partial \eta} = 0$, the temperature at which the metastable phase becomes unstable, and at which the heat capacity diverges. With these considerations in mind, we have:

$$T_0 - T_1 = -\frac{T_0 d^2}{4b_0 f} \tag{6.9}$$

For small values of d (d<<f), Eq. 6.9 tends to zero as the square of d. Close to T_1 the singularity of c_p will then become:

$$\Delta c_p = T\frac{\partial \Delta S}{\partial T} = T\frac{1}{2}\left(\frac{b_0^3}{T_0^3 f^{1/2}}\right)^{1/2}\frac{1}{\sqrt{T_1 - T}} \tag{6.10}$$

It is clear from equation 6.10 that we have a divergence in the heat capacity that behaves as $\approx 1/\sqrt{T_0 - T}$. This causes a very pronounced anomaly close to T_0. When T_1 and T_0 are close, there is a sudden transformation with the presence of latent heat, causing a lambda-like behaviour in the heat capacity. In the presence of alloying, this behaviour undergoes some peculiar changes. In particular, there can be a shift from the tricritical point towards a second-order phase transition. In this case, the anomaly becomes a step-like singularity which appears as a smoother feature in the heat capacity. We observe an analogous behaviour for our samples, with the difference that in our measurements with high concentration of indium, the smeared-out step appears to be too small to be detected, particularly because it occurs in a rapidly changing region of the heat capacity curve.

6.4 Discussion

In this Chapter we discussed the role of the indium cations (In^{III}) addition in the $Cs_2AgBiBr_6$ double perovskite. From XRD refinements, we found that Indium sits on the Bismuth site. Moreover, the presence of indium contracts the unit cell and makes the cubic phase more stable, resulting in a reduction of the cubic to tetragonal transition temperature. The low-temperature phase transition in $Cs_2AgBiBr_6$ was demonstrated to be very close to a tri-critical point. When indium is added to the perovskite, the transition acquires second-order character, resulting in a smoother lambda-anomaly in the heat capacity. A similar behaviour

has been reported, for example, for the $KMn_{1-x}Ca_xF_3$ perovskite [162]. $KMnF_3$ is close to a tricritical point, and a small amount of substitution of Ca for Mn causes the transition to cross the tricritical point from first order to second order behaviour.

7.Optoelectronic properties of $Cs_2AgBi_{1-x}In_xBr_6$ and limitations

The work presented in this chapter has been published in:

Schade, L.; Mahesh, S.; Volonakis, G.; Zacharias, M.; Wenger, B.; Schmidt, F.; Kesava, S. V.; Prabhakaran, D.; Abdi-Jalebi, M.; Lenz, M. "Crystallographic, Optical, and Electronic Properties of the $Cs_2AgBi_{1-x}In_xBr_6$ Double Perovskite: Understanding the Fundamental Photovoltaic Efficiency Challenges." *ACS Energy Lett.* **2021**, *6*, 1073– 1081.

DOI: 10.1021/acsenergylett.0c02524

Direct link: https://pubs.acs.org/doi/10.1021/acsenergylett.0c02524

Reproduced with permission from ACS Energy Lett. 2021, 6, 1073-1081. Copyright @2021, American Chemical Society

7.1 Context and summary

In the previous Chapter we investigated the structural properties of the $Cs_2AgBi_{1-x}In_xBr_6$ double perovskite. In this Chapter, we focus on the optical and electronic properties of this compound. We find that a relatively small amount of indium at the B site enhances the photoluminescence intensity and shifts the bandgap to higher energies. To investigate the impact of indium addition in devices we prepared n-i-p solar cells with and without indium in the double-perovskite layer. We discovered that the presence of indium delivers improvements in device performance: the open-circuit voltage of devices with indium is higher than that of those without it, delivering a slightly higher power conversion efficiency (PCE). Further calculations show that the device open-circuit voltage can be severely affected by the shallow optical absorption edge whose Urbach energy exceeds k_BT (where k_B is the Boltzmann constant and T = 300 K).

7.2 Experimental details

The thermodynamic modelling was performed by Dr. Suhas Mahesh. Ellipsometry measurements and analysis were performed by Dr. Sameer Vajjala Kesava. The measurements were carried out using a J. A. Woollam RC2 ellipsometer. Due to the small size of the crystals, the maximum angle at which the data (from 210-1690 nm) could be measured off the surface of the crystals was 65° (along with 55°) using focussing lens. Cubic

spline fits to the data were carried out for the refractive indices and surface roughness of the crystals, which ranged from 3-8 nm. The fitting was performed with the CompleteEase software (J. A. Woollam company). The mean squared error of the fits ranged from 2.3 (for SC1) to 13.1 (for SC25).

Photothermal Deflection Spectroscopy (PDS) data were collected by Dr. Mojtaba Abdi-Jalebi. PDS is a scatter-free surface sensitive absorption measurement capable of measuring several orders of magnitude weaker absorbance than the band edge absorption. For the measurements, a monochromatic pump light beam is shone on the sample (double-perovskite thin film on quartz substrate), which upon absorption produces a thermal gradient near the sample surface via non-radiative relaxation induced heating. This results in a refractive index gradient in the area surrounding the sample surface. This refractive index gradient is further enhanced by immersing the sample in an inert liquid FC72 Fluorinert ® (3M Company) which has a high refractive index change per unit change in temperature. A fixed wavelength CW laser probe beam is passed through this refractive index gradient producing a deflection proportional to the absorbed light at that particular wavelength, which is detected by a photo-diode and lock-in amplifier combination. Scanning through different wavelengths provides the complete absorption spectra. All the PLQE measurements and analysis have been performed by visiting Master's student Marnix Wiechers, under my close supervision.

7.3 Results

For clarity, in our figures we will present the data measured on single crystals in red, on polycrystalline powders in green, and on thin films in blue.

7.3.1 Steady-state photoluminescence and absorption

Steady-state photoluminescence spectroscopy was performed to explore the influence of indium on the optoelectronic properties of the double-perovskite material. We measured the PL directly from the surface of both single crystals and polycrystalline powders samples. This was carried out by employing a fibre-coupled laser for excitation, with detection directly through a fibre bundle in close proximity to the excitation, as detailed in Chapter 3. UV-Vis absorption spectroscopy was measured on thin films, as described in Chapter 3. Panel a of Figure 7.1 shows the emission from single crystals with different indium contents and absorption of the thin films. The emission from polycrystalline powders is illustrated in panel b in the same Figure.

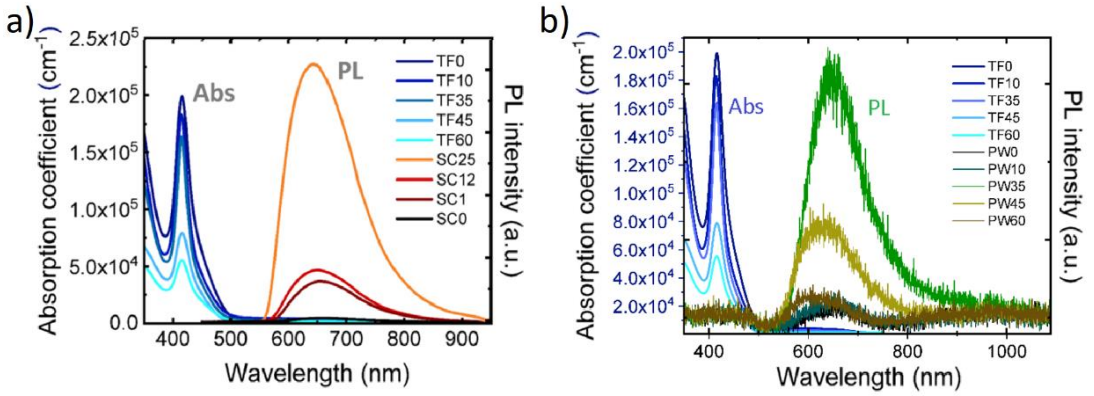


Figure 7.1 Absorption coefficient measured on $Cs_2AgBi_{1-x}In_xBr_6$ thin films from UV−vis measurements and steady-state photoluminescence of $Cs_2AgBi_{1-x}In_xBr_6$ a) single crystals and b) powders. The PL spectra of single crystals and powders have been measured as described in Section 3.5.1. Sample labels indicate: thin films TFx with x% indium on the bismuth site, single crystals SCx with x% indium, and powders PWx with x% indium.

The addition of indium clearly enhances the photoluminescence, with the PL intensity of SC25 being about 100 times greater in comparison with the net Bi crystal. The emission from polycrystalline powders was detectable but lower in intensity than the single crystals, presumably because of smaller crystallite size, increased surface area, and increased surface defect density. In panel b, we notice that the emission trend up to PW35 agrees with an increase in emission intensity and is consistent with the measurements on single crystals, while the PL starts to decrease gradually for higher indium content. In both single crystals and powders, it is noticeable that the PL peak maximum also shifts slightly towards higher energies when indium is added to the structure, as shown in Figure 7.2.

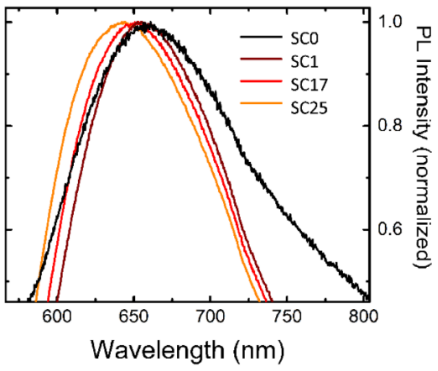


Figure 7.2 Normalized photoluminescence spectra of $Cs_2AgBi_{1-x}In_xBr_6$ single crystal samples, excited with a 405 nm laser. Sample labels indicate single crystals with 0% indium on the bismuth site (SC0), 1% (SC1), 12% (SC12) and 25% (SC25) respectively.

In Figure 7.1 we notice a pronounced resonant absorption peak centred at ~420 nm, as previously reported in literature [163], [164]. There is still debate about the origin of this feature, which has been associated with trapped excitonic transitions below the high-energy, direct band gap [163]–[166], or to intra-band transitions [167], [168].

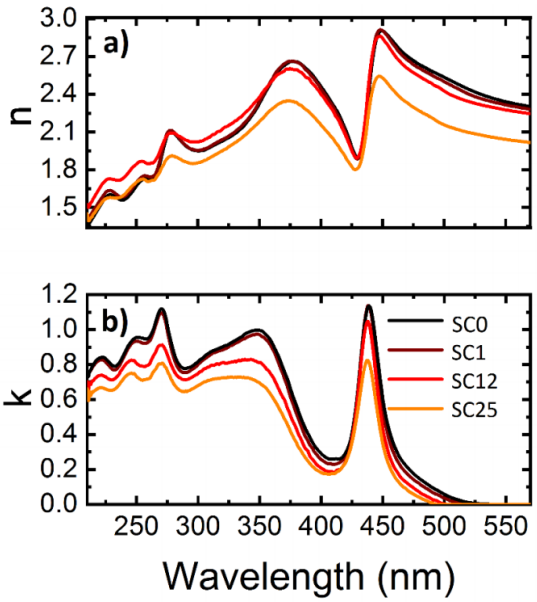


Figure 7.3 Optical constants a) n and b) k determined from spectroscopic ellipsometry measurements of $Cs_2AgBi_{1-x}In_xBr_6$ single crystals with a range of indium contents. Sample labels indicate single crystals with 0% indium on the bismuth site (SC0), 1% (SC1), 12% (SC12) and 25% (SC25) respectively.

The overall absorption strength decreases with increasing indium content. This decrease is further confirmed by the extinction coefficient obtained from spectroscopy ellipsometry measurements of the single crystals, as shown in Figure 7.3. The alloyed double perovskite maintains the same main features of neat $Cs_2AgBiBr_6$ in absorption and emission, with a decrease in absorption and an increase in the photoluminescence emission intensity for low indium content (<35%). The increased PL intensity indicates fewer, or less active, defect sites responsible for trap-assisted recombination, suggesting that the introduction of a small amount of indium may enhance the electronic properties of $Cs_2AgBi_{1-x}In_xBr_6$ for use as the photoactive layer in PV devices.

7.3.2 Sub-bandgap absorption

We expect these double perovskites to have a weakly absorbing indirect band gap and potentially a high density of sub-band gap defect states. Therefore, we performed photothermal deflection optical absorption spectroscopy on our thin films to investigate the region below the band gap. As shown in panel a of Figure 7.4, the PDS spectrum curves

clearly show panchromatic absorption below the band gap, indicating the presence of sub-band gap states. The Urbach energy, which represents the electronic disorder at the band edge, was calculated through a fitting of the PDS data. With the values reported in Table 7.1 we can observe that the Urbach energy ranges from 50 to 65 meV. These values are greater than those determined for lead and tin halide perovskites [169]–[171]. This difference in E_u is consistent with the lower performance of all-inorganic perovskites, especially in terms of the V_{oc} [172]. Table 7.1 also reports the band gap extrapolated from a Tauc plot analysis (as shown in panel b of Figure 7.4) and indicates a clear enlargement with increasing indium percentage, going from 2.23 eV for TF0 to 2.32 eV for TF60.

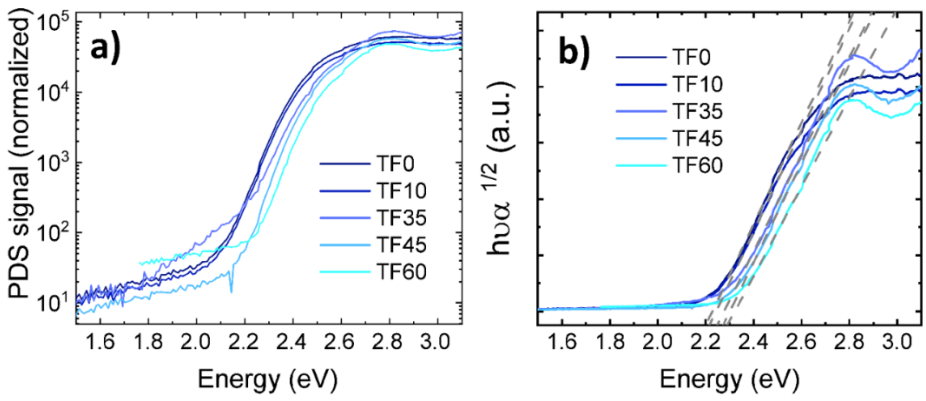


Figure 7.4 a) PDS absorption measurements on thin films and b) Tauc-plots measured on $Cs_2AgBi_{1-x}In_xBr_6$ for different concentrations of indium. Samples labels indicate thin films with 0% indium on the bismuth site (TF0), 10% (TF10), 35% (TF35), 45% (TF45) and 60% (TF60) respectively.

Thin film	Band gap (eV)	E_u (meV)
TF0	2.23	65.13 ± 0.77
TF10	2.24	63.22 ± 0.89
TF35	2.27	61.91 ± 0.55
TF45	2.30	54.03 ± 0.67
TF60	2.32	50.91 ± 0.76

Table 7.1 Values of the band gaps and Urbach energies (E_u) for $Cs_2AgIn_xBi_{1-x}Br_6$ thin films.

7.3.3 $Cs_2AgBi_{1-x}In_xBr_6$ devices

To assess the effects of indium alloying on the performance of photovoltaic devices, we prepared planar heterojunction photovoltaic devices in the n-i-p architecture, employing SnO_2 nanoparticles as the n-type charge extraction layer and doped spiro-OMeTAD as the p-type charge extraction layer, as detailed in Chaper 3. $Cs_2AgBiBr_6$ double perovskites have

been reported to cause a strong hysteresis between the forward (from V_{OC} to J_{SC}) and the reverse (from J_{SC} to V_{OC}) scan, as we can notice from the J-V curves in Figure 7.5.

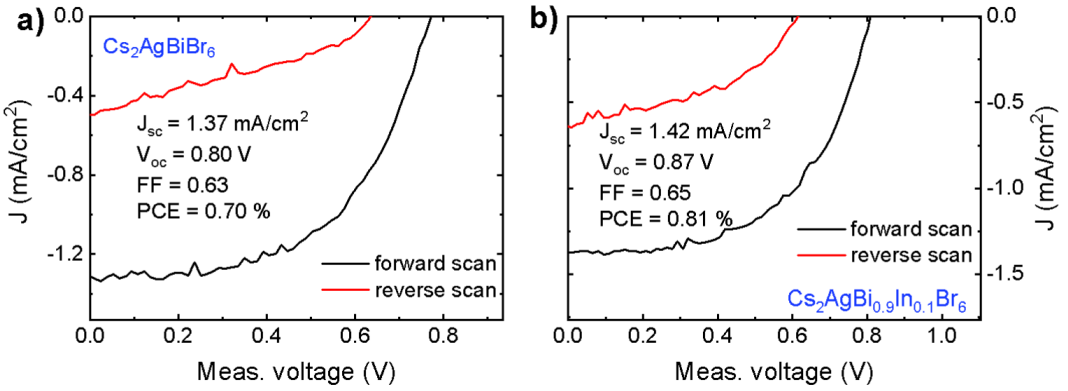


Figure 7.5 J-V scans for the best devices made with a) $Cs_2AgBiBr_6$ and b) $Cs_2AgBi_{0.9}In_{0.1}Br_6$ as absorbing layer. Devices have been prepared as described in Section 3.7.

The performance of these devices is poorly reproducible, varying from batch to batch. For this reason, it is more indicative and useful to observe the averaged current-density-voltage curve performance parameters, rather than the single J-V scans. In panel a of Figure 7.6 we show the short-circuit current for a single batch of cells comparing the neat bismuth to the 10% indium alloyed double perovskite, measured under AM1.5 simulated sunlight.

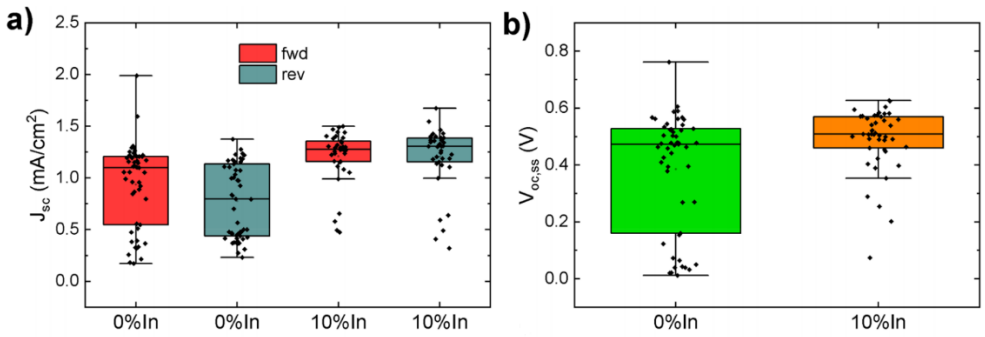


Figure 7.6 a) Short-circuit current and b) steady-state open-circuit voltage (box plot) for devices with $Cs_2AgBiBr_6$ and $Cs_2AgBi_{0.9}In_{0.1}Br_6$ used as absorber layer. Devices have been prepared as described in Section 3.7.

We notice from panel a that the addition of 10% indium improves the short-circuit current in both the reverse and forward scans, and this results in an overall improvement of the PCE, as shown in panel a of Figure 7.7. We notice that the spread in data decreases when measuring the cells with the indium-alloyed perovskite, and the steady-state open-circuit voltage is slightly higher (as shown in Figure 7.6b).

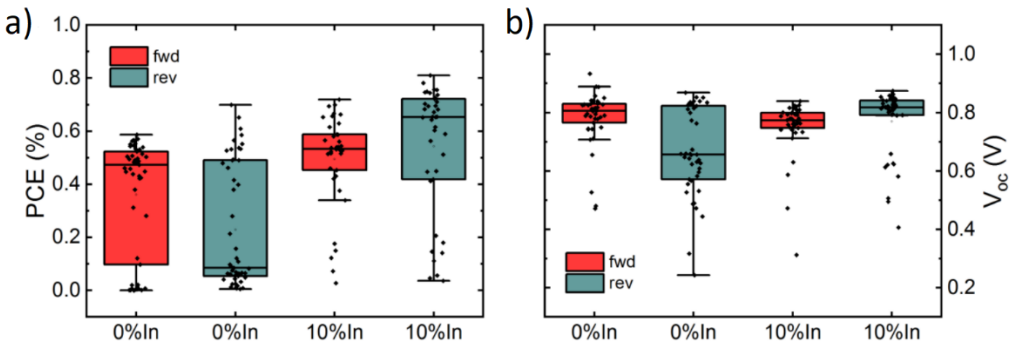


Figure 7.7 a) Power conversion efficiency (PCE) and b) open-circuit voltage (Voc) for $Cs_2AgIn_xBi_{1-x}Br_6$ devices with and without indium, for the forward and reverse scans. Devices have been prepared as described in Section 3.7.

Figure 7.8 shows the External Quantum Efficiency and integrated current measured on devices with and without indium in the perovskite absorber layer. We notice that the integrated current of devices containing indium has a slightly higher overall intensity in comparison with the current of control devices with the neat $Cs_2AgBiBr_6$ perovskite, in agreement with our measured J_{SC} current. Moreover, we observe that the peak at ~ 420 nm that we saw in the absorption spectra is present also in this measurement, for both the devices. We also notice a feature appearing at ~500 nm in the EQE spectra of both samples. We tentatively assign this to a photo-response from light absorption into the indirect band gap. However, further investigation is needed to understand its origin.

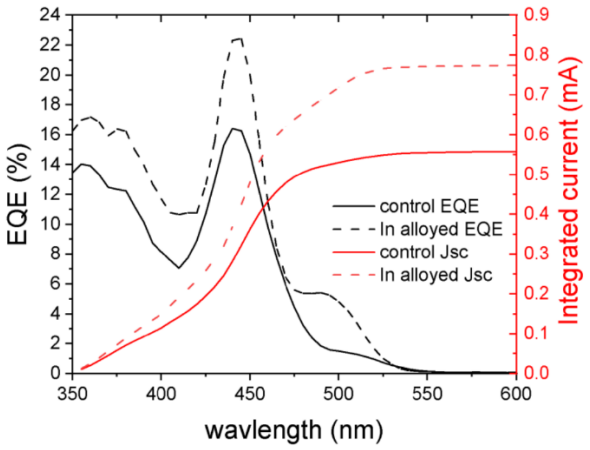


Figure 7.8 External Quantum Efficiency (EQE) and Integrated current measured on $Cs_2AgIn_xBi_{1-x}Br_6$ devices with (dotted lines) and without (continuous lines) 10% indium. Devices have been prepared as described in Section 3.7.

7.3.4 The detailed balance

It is important to notice that the calculations in this Section constitute an ideal upper-limit for the case in which the recombination is a band-to-band recombination, as they were calculated without clear consensus about the origin of the PL emission. As we have described in Chapter 5, the emission can actually be well explained with a Huang-Rhys model which indicates strong electron-phonon interaction in this material.

For a band gap of 2.23 eV, the Shockley–Quiesser formalism [131], [173] predicts a limiting PCE of 18% with V_{OC} = 1.91 V, J_{SC} = 10.14 mA/cm^2, and FF = 0.93. However, the best $Cs_2AgBiBr_6$-based cells today reach only 2.8% PCE (V_{OC} = 1.06 V, J_{SC} = 5.13 mA/cm^2, and FF = 0.52) [174]. Longo et al. have shown that the large current deficit is due to poor electron diffusion length (tens of nanometers) [129]. This is likely to be true for the indium alloyed material as well. The difference between the band gap energy and the open-circuit voltage a cell can generate is a good measure of the minimum energy loss in the photovoltaic cell, which is often termed a voltage deficit or loss-in-potential. For a material with a band gap of 2.23 eV, the minimum voltage deficit for an ideal cell is 320 mV. However, our best experimental cell shows a maximum V_{OC} of only 0.93 V and hence a voltage deficit of over 1400 mV, as shown in Figure 7.7.

To understand this result we need to assess what causes this voltage deficit, whether it is a fundamental barrier for this material ever being efficient or if there are potential solutions to overcoming a large fraction of these deficiencies. The voltage deficit may originate from a combination of factors, including high dark recombination current densities (due to the fundamental optical properties of the material), a significant fraction of nonradiative recombination (resulting from high defect densities in the bulk of the absorber material), high surface recombination velocities on the surface of the absorber layer, and high surface recombination at the absorber layer/charge extraction layer interfaces. Furthermore, poor charge carrier selectivity of the transport layers may also inhibit open-circuit voltage [175], [176]. From a fundamental standpoint, even in the absence of defects and interfaces responsible for nonradiative recombination, the sub-band gap optical properties of a solar absorber layer can strongly influence the maximum open-circuit voltage a material can achieve when integrated into a solar cell. This is because the dark-recombination current density (J_0) can be calculated by taking the overlap integral of the blackbody radiation at the background temperature (T ≈ 300 K) with the external quantum efficiency spectra of the solar cell. Because the blackbody radiation spectra at ambient temperature increase

exponentially toward lower energies, the overall J_0 is most strongly influenced by absorption properties in the sub-band gap region of the absorber layer. In the first instance, this can be quantified by the steepness of the absorption onset just below the band gaps, as with the aforementioned Urbach energy. If the Urbach energy is less than the thermal energy at the operation temperature ($k_BT \approx 25$ meV at 300 K, where k_B is the Boltzmann constant), then the additional voltage deficit, beyond that calculated via the Shockley–Queisser (SQ) treatment (which assumes a step function absorption onset), is close to negligible (a few tens of millielectronvolts). However, once the Urbarch energy increases beyond k_BT, then the voltage deficit becomes increasingly significant [172].

We quantified this loss for our $Cs_2AgBi_{0.9}In_{0.1}Br_6$ material using the principle of detailed balance. This calculation takes the absorber's absorptance as input and then predicts the V_{OC} assuming that all the recombination is radiative, i.e. in the radiative limit [177], [178]. This in principle provides a lower-bound for the V_{OC} loss, which would be the voltage expected if all other nonradiative recombination paths were eliminated. We performed this calculation under different assumptions to illustrate a range of possibilities, because the properties of this material are not yet entirely understood.

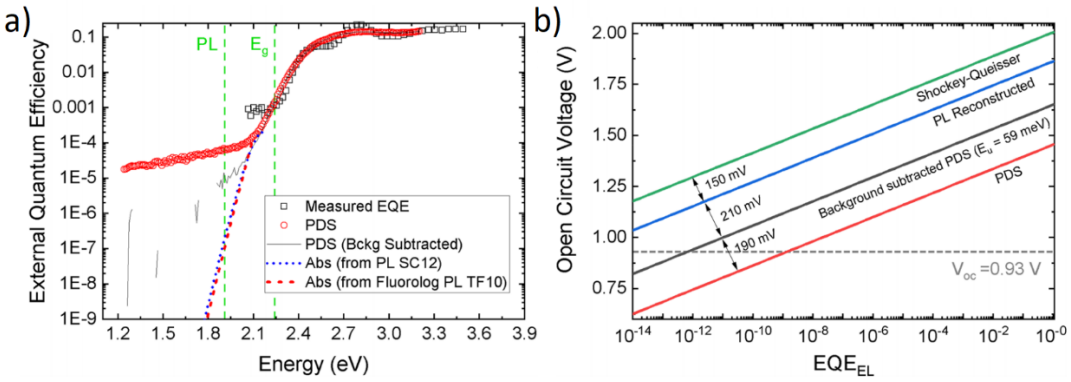


Figure 7.9 a) The black squares represent the measured external quantum efficiency; the red circles and black line the measured PDS without and with a linear background subtraction, respectively; and the blue and red dashed lines the reconstructed absorption from the PL measured on SC12 and TF10, respectively. b) Open-circuit voltage calculated using detailed balance for spectra shown in panel a. The dashed line in this panel indicates the highest open-circuit voltage measured on our devices.

Using the measured PDS absorption as input for the detailed balance calculation, we estimate the voltage deficit in the radiative limit to be at least 870 mV, which is 550 mV greater than the SQ limit Voc. We note that if the tail extends below 1.3 eV (the limit of our detector), the loss is expected to be even greater. However, we also consider the possibility that the PDS absorption plateau below 2.1 eV is due to free carrier absorption, or sub-band

gap defects which are not part of the continuum of states, and not a fundamental property of the material [179]. When we subtract this panchromatic sub-band gap absorption feature, the resulting ~59 meV Urbach tail results in a V_{OC} deficit of 680 mV from band gap and a 360 mV greater loss than in the SQ limit.

As we mentioned before, there is no clear consensus on the mechanism of PL emission in this material. In the case that it is band-to-band recombination, the radiative states can be reconstructed, often to extremely low values, using emission−absorption reciprocity [180], [181]. We follow the reciprocity approach and use these reconstructed states to extend our measured absorption spectra down to lower energies.

Using this "PL reconstructed absorption spectra" we estimate the V_{OC} deficit to be 470 mV from the band gap, which is only 150 mV greater than the SQ limit.

By definition, the external radiative efficiency (ERE) is below 1. To put this into context, the highest-performing Si, GaAs, CdTe, and lead-halide perovskite cells have EREs of ~0.01, 0.3, 0.00008, and 0.06, respectively [182], [183]. In Figure 7.9, we show the open-circuit voltage for our $Cs_2AgBi_{0.9}In_{0.1}Br_6$ cell, which we calculate following the detailed balance principle, as a function of ERE. As is clearly apparent, the fundamental offset from the SQ voltage, related to shallow absorption onset and sub-band gap absorptions, remains constant across all values of ERE. As inferred by comparing our achieved open-circuit voltage to the calculated values, the maximum ERE of our cell will range from 10^{-10} to 10^{-15}, depending upon what is the truest reflection of the absorption edge in this material. This indicates that the primary target for immediate improvement in the $Cs_2AgBi_{0.9}In_{0.1}Br_6$ PV cells is to focus upon enhancing ERE.

7.3.5 Photoluminescence quenching

To investigate losses at the device interfaces, we monitored the PLQE of the $Cs_2AgBiBr_6$ double perovskite in contact with different transport-layers. The PLQE in this case is a good indicator of which interface causes the most non-radiative losses [184], [185]. The substrates preparation has been descripted in the Experimental Chapter. Figure 7.10 shows the PLQE of the $Cs_2AgBiBr_6$ perovskite on ITO with a diverse range of transport layers. The error bars indicate the standard deviation, and the measurement of the perovskite layer on quartz is included for reference. The perovskite on quartz resulted in the highest PLQY value (0.081%), which is multiple orders of magnitudes lower than in lead-halide perovskites [185], but compatible with the value reported by Longo et al. [102].

Nickel Oxide (NiO_x) is included as a possible HTL to be used in a p-i-n architecture, which is an important addition as it shows the poor performance for HTL-containing stacks does not depend on deposition order. The NiO_x solution was prepared by dissolving 29 mg/mL $Ni(NO_3)_2 \cdot H_2O$ in 2-methoxyethanol with 10 µL/mL acetylacetone, was dynamically spin coated in a dry air environment at 1500 rpm for 30 s, then annealed at 300 °C for 45 minutes.

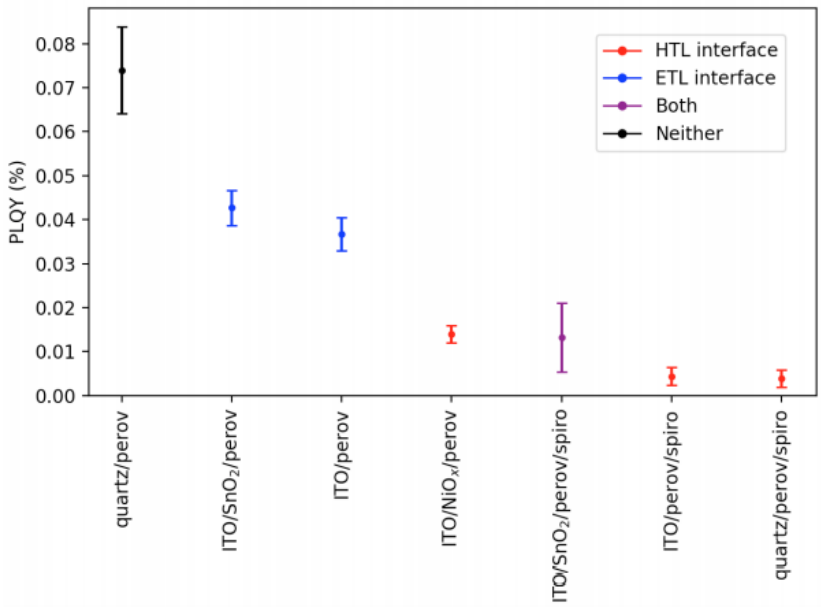


Figure 7.10 The PLQE of different stacks with a $Cs_2AgBiBr_6$ perovskite absorber/emitter with varying neighbouring layers and interfaces.

As we saw in the previous sub-section, the open-circuit voltage of the devices is far below the expected 1.68 V from Shockley-Queisser limit. In fact, every order-of-magnitude decrease in PLQE corresponds to a 60 mV loss in V_{OC} compared to the Shockley-Queisser limit [178]. It is clear from Figure 7.10 that the hole-transport layers (HTL) cause more non-radiative recombination than the electron-transport-layers (ETL) at V_{OC}, which might be associated with the energetic band offset at the interface. We observe that all the transport materials used in the study quench the PLQE and further effort has to be put into exploring how the $Cs_2AgBiBr_6$ absorber layer interfaces with charge-selective contacts.

7.4 Discussion

We found that a small percentage of indium enhances the photoluminescence intensity and improves the photovoltaic performances of devices, showing almost doubled J_{SC} and PCE when 10% of indium is added to the structure. Nevertheless, these devices remain considerably less efficient than lead halide perovskite PV cells, leading us to assess the losses in the material from a fundamental perspective. We determine that significant losses in open-circuit voltage are present because of a shallow onset of the absorption edge, combined with significant sub-band gap absorption. However, if improvements can be made to "clean up" the panchromatic sub-band gap absorption, and if the emission mechanism is regulated by band-to-band recombination, in an ideal upper limit case the additional losses beyond those of the SQ limit would only be 150 mV. Nevertheless, as we have seen in Chapter 5, the emission process in this material seems likely to be related to emission from a colour centre, and further effort would be required to get a more detailed picture of the non-radiative losses' pathways.

At present, the majority of the losses originate from low radiative efficiency. Immediate attention is required to understand and mitigate the role and presence of non-radiative defect sites in the absorber material, and the nature of nonradiative recombination and non-selectivity at the charge extraction layer/absorber layer heterojunctions.

Concerning the absorber material itself, the band-gap is non-ideal for use in PV cells, being too wide at 2.23 eV for optimum use as a top cell in both tandem ($E_g \approx 1.65$ eV required) and even triple-junction cells ($E_g \approx 2.05$ eV required) [186]. Therefore, strategies to reduce the band gap are likely to lead to improved performance and utility. These should probably focus upon strategies to stabilize iodide in the Cs_2AgBiX_6 framework or explore the broader Ag-Bi halide materials space [114]. It is likely that indium substitution will be broadly applicable for enhancing the luminescence of this family of materials. For light emission applications, green and red emission would be favourable for the use of these compounds as phosphors. For that purpose, chlorine doping is likely to prove useful.

Conclusions and Outlook

The work presented in this Thesis has been primarily been focused on the structural, optical and electronic properties of the candidate $Cs_2AgBi_{1-x}In_xBr_6$ double perovskite for optoelectronic applications. The motivation behind this study relies on the fact that the commercialization of lead-halide perovskite photovoltaics is hindered by the presence of lead and by the instability of the absorber. Attempts at homovalent substitution of the lead cation, for example with Sn^{2+} or Ge^{2+}, are compromised by the high chance of oxidation [29]. For this reason, heterovalent substitution with monovalent and trivalent cations has been investigated, offering a larger compositional space of possible materials. In this scenario, $Cs_2AgBiBr_6$ proved to be an interesting candidate as it is highly stable and non-toxic. Nevertheless, the power conversion efficiencies obtained so far only reached 2.84% at best. Despite a long-lived component to the charge-carrier lifetime this double-perovskite possess an indirect band-gap that hinders its photovoltaic performance. Moreover, the strong presence of non-radiative recombination is not favourable for PV applications. A deeper understanding of the structural and optical properties was needed to explore possibilities for improvement, and to find out if this material could ever match the optoelectronic performances of the more widely studied lead-halide perovskites.

In Chapter 4, we investigated the structural properties of $Cs_2AgBiBr_6$ double perovskite, discovering a phase transition at $T_s \approx 122$ K from the room-temperature cubic structure with space group $Fm\bar{3}m$, to a tetragonal structure with space group I4/m. In Chapter 5 we demonstrate that the optical properties of this material strongly correlate with the structural phase transition. In fact, we found that the exciton energy at the direct gap is mainly dependent on the rotational degree of freedom that arises in the tetragonal phase. Moreover, we discovered that an additional TRPL decay channel arises in the tetragonal phase, which we link to the presence of defects at the twinning boundaries. This means that the presence of twinning boundaries can potentially reduce the charge carrier lifetime. Therefore, an optimization of the deposition method for this material would likely prove useful, in order to reduce grain boundaries in polycrystalline thin films that could affect the charge carrier behaviour.

In Chapter 6, we investigated the potential of inclusion of the indium cation in the double perovskite structure. The substitution of indium on the bismuth site caused the lattice to shrink. Moreover, we found that the transition in $Cs_2AgBiBr_6$ is very close to a tricritical point, and the presence of indium moves the transition point towards a second-order phase

transition. Chapter 7 focused on the optoelectronic properties of $Cs_2AgBi_{1-x}In_xBr_6$, and in particular, the influence of indium on these properties. We noticed that the addition of a small percentage of indium increases the PL intensity quite dramatically, which would encourage the use of this cation in the absorber for photovoltaics applications. At the same time, this improvement seems to result in a slightly higher V_{OC}, J_{SC} and P_{CE} when the absorber includes 10% of indium on the bismuth site.

From the perspective of the intrinsic properties of the absorber itself, these materials present an Urbach energy that is quite high (≈ 60 meV) and higher than k_BT at room temperature. For this reason, the sub-band gap absorption that we see from PDS measurements might have a central role when calculating the losses in the device. The dark recombination current density is strongly influenced by absorption properties below the band-gap, and it is more dominant when the Urbach energy is high. Our thermodynamic calculations, considering an ideal case in which all the recombination is radiative and the charge carrier processes are only dominated by band-to-band recombination, gave us 550 mV more losses than in the SQ limit, when calculated using the PDS absorption. Further improvement to decrease the amount of non-radiative recombination is needed to be able to optimize this material for use in photovoltaic devices.

The assumption that band-to-band recombination processes are the only recombination processes happening in the material represents an ideal, possibly un-realistic “upper” limit case for our calculations. In fact, the emission processes in this material are yet to be fully understood. In one of our collaborative works we stated that the emission could be related to a colour centre more than to band-to-band recombination (as explained in Chapter 7), as this material presents a very strong electron-phonon coupling. Very recently the emission has been related to a self-trapped, small polaronic state that exhibits temperature-activated mobilities. The self-trapped charge carriers diffuse to colour centres, causing a broad emission that is strongly red-shifted from the direct band edge.

Regardless of whether $Cs_2AgBi_{1-x}In_xBr_6$ can be optimized, this compound is an interesting model system for understanding the physics of the wider family of halide perovskites. All these materials have closely related crystal structures, and understanding structure-property relations is highly relevant for materials that are already known to have higher efficiency and for guiding the design of future compounds. Moreover, the broad Ag-Bi space allows for a high tunability of the optical and electronic properties of this absorber, and it is

likely that this study will prove useful to discover and understand other materials in the same family that show complementary or improved functionality.

References

[1] NASA, “2020 Tied for Warmest Year on Record, NASA Analysis Shows,” 2021. https://www.nasa.gov/press-release/2020-tied-for-warmest-year-on-record-nasa-analysis-shows.

[2] M. Lockwood, “Solar change and climate: An update in the light of the current exceptional solar minimum,” *Proc. R. Soc. A Math. Phys. Eng. Sci.*, vol. 466, no. 2114, pp. 303–329, 2010, doi: 10.1098/rspa.2009.0519.

[3] J. L. Lean, “Cycles and trends in solar irradiance and climate,” *Wiley Interdiscip. Rev. Clim. Chang.*, vol. 1, no. 1, pp. 111–122, 2010, doi: 10.1002/wcc.18.

[4] A. Witze, “Dramatic sea-ice melt caps tough Arctic summer,” *Nature*, vol. 573, no. 7774, pp. 320–321, 2019, doi: 10.1038/d41586-019-02653-x.

[5] N. Mimura, “Sea-level rise caused by climate change and its implications for society,” *Proc. Japan Acad. Ser. B Phys. Biol. Sci.*, vol. 89, no. 7, pp. 281–301, 2013, doi: 10.2183/pjab.89.281.

[6] O. Hoegh-Guldberg, E. S. Poloczanska, W. Skirving, and S. Dove, “Coral reef ecosystems under climate change and ocean acidification,” *Front. Mar. Sci.*, vol. 4, no. MAY, 2017, doi: 10.3389/fmars.2017.00158.

[7] M. K. Tippett, “Extreme weather and climate,” *npj Clim. Atmos. Sci.*, vol. 1, no. 1, pp. 3–4, 2018, doi: 10.1038/s41612-018-0057-1.

[8] G. Lanzani, *The Photophysics behind Photovoltaics and Photonics*. 2012.

[9] R. F. Service, “Is it time to shoot for the sun?,” *Science (80-.).*, vol. 309, no. 5734, pp. 548–551, 2005, doi: 10.1126/science.309.5734.548.

[10] International Energy Agency, “World Energy Statistics 2017,” *Statistics (Ber).*, p. 80, 2017.

[11] Charles Kittel and C. Kittel, *Introduction to Solid State Physics*, 8th ed. 2004.

[12] J. P. Correa-Baena *et al.*, “Promises and challenges of perovskite solar cells,” *Science (80-.).*, vol. 358, no. 6364, pp. 739–744, 2017, doi: 10.1126/science.aam6323.

[13] A. Kojima, K. Teshima, Y. Shirai, and T. Miyasaka, “Organometal halide perovskites as visible-light sensitizers for photovoltaic cells,” *J. Am. Chem. Soc.*, vol. 131, no. 17, pp. 6050–6051, 2009, doi: 10.1021/ja809598r.

[14] NREL, “Best Research-Cell Efficiency Chart,” 2021. https://www.nrel.gov/pv/cell-efficiency.html (accessed Sep. 26, 2021).

[15] G. Schileo and G. Grancini, “Halide perovskites: current issues and new strategies to push material and device stability,” *JPhys Energy*, vol. 2, no. 2, 2020, doi: 10.1088/2515-7655/ab6cc4.

[16] G. Schileo and G. Grancini, “Lead or no lead? Availability, toxicity, sustainability and environmental impact of lead-free perovskite solar cells,” *J. Mater. Chem. C*, vol. 9, no. 1, pp. 67–76, 2021, doi: 10.1039/d0tc04552g.

[17] J. Li *et al.*, “Biological impact of lead from halide perovskites reveals the risk of

introducing a safe threshold," *Nat. Commun.*, vol. 11, no. 1, pp. 1–5, 2020, doi: 10.1038/s41467-019-13910-y.

[18] S. Gu, R. Lin, Q. Han, Y. Gao, H. Tan, and J. Zhu, "Tin and Mixed Lead–Tin Halide Perovskite Solar Cells: Progress and their Application in Tandem Solar Cells," *Adv. Mater.*, vol. 32, no. 27, pp. 1–16, 2020, doi: 10.1002/adma.201907392.

[19] T. Leijtens, R. Prasanna, A. Gold-parker, and M. F. Toney, "Mechanism of Tin Oxidation and Stabilization," 2017, doi: 10.1021/acsenergylett.7b00636.

[20] H. Yao, F. Zhou, Z. Li, Z. Ci, L. Ding, and Z. Jin, "Strategies for Improving the Stability of Tin-Based Perovskite (ASnX3) Solar Cells," *Adv. Sci.*, vol. 7, no. 10, 2020, doi: 10.1002/advs.201903540.

[21] G. Volonakis *et al.*, "Lead-Free Halide Double Perovskites via Heterovalent Substitution of Noble Metals," *J. Phys. Chem. Lett.*, vol. 7, no. 7, pp. 1254–1259, Apr. 2016, doi: 10.1021/acs.jpclett.6b00376.

[22] C. Wu *et al.*, "The Dawn of Lead-Free Perovskite Solar Cell: Highly Stable Double Perovskite Cs 2 AgBiBr 6 Film," *Adv. Sci.*, vol. 5, no. 3, p. 1700759, Mar. 2018, doi: 10.1002/advs.201700759.

[23] A. H. Slavney, T. Hu, A. M. Lindenberg, and H. I. Karunadasa, "A Bismuth-Halide Double Perovskite with Long Carrier Recombination Lifetime for Photovoltaic Applications," *J. Am. Chem. Soc.*, vol. 138, no. 7, pp. 2138–2141, Feb. 2016, doi: 10.1021/jacs.5b13294.

[24] E. Greul, M. L. Petrus, A. Binek, P. Docampo, and T. Bein, "Highly stable, phase pure Cs2AgBiBr6 double perovskite thin films for optoelectronic applications," *J. Mater. Chem. A*, vol. 5, no. 37, pp. 19972–19981, 2017, doi: 10.1039/c7ta06816f.

[25] W. Gao *et al.*, "High-Quality Cs2AgBiBr6Double Perovskite Film for Lead-Free Inverted Planar Heterojunction Solar Cells with 2.2% Efficiency," *ChemPhysChem*, pp. 1–6, 2018, doi: 10.1002/cphc.201800346.

[26] E. T. McClure, M. R. Ball, W. Windl, and P. M. Woodward, "Cs2AgBiX6(X = Br, Cl): New Visible Light Absorbing, Lead-Free Halide Perovskite Semiconductors," *Chem. Mater.*, vol. 28, no. 5, pp. 1348–1354, 2016, doi: 10.1021/acs.chemmater.5b04231.

[27] M. R. Filip, S. Hillman, A. A. Haghighirad, H. J. Snaith, and F. Giustino, "Band Gaps of the Lead-Free Halide Double Perovskites $Cs_2BiAgCl_6$ and $Cs_2BiAgBr_6$ from Theory and Experiment," *J. Phys. Chem. Lett.*, vol. 7, no. 13, pp. 2579–2585, 2016, doi: 10.1021/acs.jpclett.6b01041.

[28] W. Shockley and H. J. Queisser, "Detailed balance limit of efficiency of p-n junction solar cells," *J. Appl. Phys.*, vol. 32, no. 3, pp. 510–519, 1961, doi: 10.1063/1.1736034.

[29] S. F. Hoefler, G. Trimmel, and T. Rath, "Progress on lead-free metal halide perovskites for photovoltaic applications: a review," *Monatshefte fur Chemie*, vol. 148, no. 5, pp. 795–826, 2017, doi: 10.1007/s00706-017-1933-9.

[30] Z. Cheng and J. Lin, "Layered organic-inorganic hybrid perovskites: Structure, optical properties, film preparation, patterning and templating engineering," *CrystEngComm*, vol. 12, no. 10, pp. 2646–2662, 2010, doi: 10.1039/c001929a.

[31] Goldschmidt V.M., "Krystallbau und chemische Zusammensetzung (Crystal structure

and chemical correlation)," *Ber. Dtsch. Chem. Ges.*, vol. 60, pp. 1263–1296, 1927.

[32] Q. Chen *et al.*, "Under the spotlight: The organic–inorganic hybrid halide perovskite for optoelectronic applications," *Nano Today*, vol. 10, no. 3, pp. 355–396, Jun. 2015, doi: 10.1016/j.nantod.2015.04.009.

[33] N. Song, J. M. Rondinelli, and B. G. Kim, "Noncentrosymmetric structural transitions in ultrashort ferroelectric AGa O3/A'Ga O3 superlattices," *Phys. Rev. B - Condens. Matter Mater. Phys.*, vol. 91, no. 13, pp. 1–7, 2015, doi: 10.1103/PhysRevB.91.134104.

[34] M. Helen D, "Crystal Structures: A Working Approach.," *W.B. Saunders Co.*, 1973.

[35] A. M. Glazer, "The classification of tilted octahedra in perovskites," *Acta Crystallogr. Sect. B Struct. Crystallogr. Cryst. Chem.*, vol. 28, no. 11, pp. 3384–3392, 1972, doi: 10.1107/s0567740872007976.

[36] E. A. R. Assirey, "Perovskite synthesis, properties and their related biochemical and industrial application," *Saudi Pharm. J.*, vol. 27, no. 6, pp. 817–829, 2019, doi: 10.1016/j.jsps.2019.05.003.

[37] F. Panzer, C. Li, T. Meier, A. Köhler, and S. Huettner, "Impact of Structural Dynamics on the Optical Properties of Methylammonium Lead Iodide Perovskites," *Adv. Energy Mater.*, vol. 7, no. 16, pp. 1–11, 2017, doi: 10.1002/aenm.201700286.

[38] A. Jaffe, Y. Lin, and H. I. Karunadasa, "Halide Perovskites under Pressure: Accessing New Properties through Lattice Compression," *ACS Energy Lett.*, vol. 2, no. 7, pp. 1549–1555, 2017, doi: 10.1021/acsenergylett.7b00284.

[39] C. J. Howard and H. T. Stokes, "Group-Theoretical Analysis of Octahedral Tilting in Perovskites," *Acta Crystallogr. Sect. B Struct. Sci.*, vol. 54, no. 6, pp. 782–789, 1998, doi: 10.1107/S0108768198004200.

[40] P. S. Whitfield *et al.*, "Structures, Phase Transitions and Tricritical Behavior of the Hybrid Perovskite Methyl Ammonium Lead Iodide," *Sci. Rep.*, vol. 6, no. October, pp. 1–16, 2016, doi: 10.1038/srep35685.

[41] M. R. Linaburg, E. T. McClure, J. D. Majher, and P. M. Woodward, "Cs1-xRbxPbCl3 and Cs1-xRbxPbBr3 Solid Solutions: Understanding Octahedral Tilting in Lead Halide Perovskites," *Chem. Mater.*, vol. 29, no. 8, pp. 3507–3514, 2017, doi: 10.1021/acs.chemmater.6b05372.

[42] C. J. Howard, B. J. Kennedy, and P. M. Woodward, "Ordered double perovskites - A group-theoretical analysis," *Acta Crystallogr. Sect. B Struct. Sci.*, vol. 59, no. 4, pp. 463–471, 2003, doi: 10.1107/S0108768103010073.

[43] G. Jaeger, "The ehrenfest classification of phase transitions: Introduction and evolution," *Arch. Hist. Exact Sci.*, vol. 53, no. 1, pp. 51–81, 1998, doi: 10.1007/s004070050021.

[44] Stephen J. Blundell and Katherine M. Blundell, *Concepts in Thermal Physics*. Oxford Scholarship Online, 2010.

[45] Landau L., "On the theory of phase transitions," *Landau L.D. "Collected Pap. (Nauka, Moscow)*, vol. 1, pp. 234–252, 1969.

[46] P. Chaikin M. and T. C. Lubensky, *Principles of condensed matter physics*, 4th print. Cambridge University Press, 2007.

[47] M. A. Green, Y. Jiang, A. M. Soufiani, and A. Ho-Baillie, “Optical Properties of Photovoltaic Organic-Inorganic Lead Halide Perovskites,” *J. Phys. Chem. Lett.*, vol. 6, no. 23, pp. 4774–4785, 2015, doi: 10.1021/acs.jpclett.5b01865.

[48] M. B. Johnston and L. M. Herz, “Hybrid Perovskites for Photovoltaics: Charge-Carrier Recombination, Diffusion, and Radiative Efficiencies,” *Acc. Chem. Res.*, vol. 49, no. 1, pp. 146–154, 2016, doi: 10.1021/acs.accounts.5b00411.

[49] S. De Wolf *et al.*, “Organometallic halide perovskites: Sharp optical absorption edge and its relation to photovoltaic performance,” *J. Phys. Chem. Lett.*, vol. 5, no. 6, pp. 1035–1039, 2014, doi: 10.1021/jz500279b.

[50] M. Saba, F. Quochi, A. Mura, and G. Bongiovanni, “Excited State Properties of Hybrid Perovskites,” *Acc. Chem. Res.*, vol. 49, no. 1, pp. 166–173, 2016, doi: 10.1021/acs.accounts.5b00445.

[51] X. C. Tong, *Advanced Materials for Integrated Optical Waveguides*. Springer Series in Advanced Microelectronics, 2014.

[52] G. E. Eperon, S. D. Stranks, C. Menelaou, M. B. Johnston, L. M. Herz, and H. J. Snaith, “Formamidinium lead trihalide: A broadly tunable perovskite for efficient planar heterojunction solar cells,” *Energy Environ. Sci.*, vol. 7, no. 3, pp. 982–988, 2014, doi: 10.1039/c3ee43822h.

[53] F. Urbach, “The long-wavelength edge of photographic sensitivity and of the electronic Absorption of Solids [8],” *Phys. Rev.*, vol. 92, no. 5, p. 1324, 1953, doi: 10.1103/PhysRev.92.1324.

[54] M. V. Kubik, “Urbach Rule,” *phys. stat. sol.*, vol. 9, no. 8, 1971.

[55] D. G. Thomas, J. J. Hopfield, and M. Power, “Excitons and the absorption edge of cadmium sulfide,” *Phys. Rev.*, vol. 119, no. 2, pp. 570–574, 1960, doi: 10.1103/PhysRev.119.570.

[56] G. D. Cody, T. Tiedje, B. Abeles, T. D. Moustakas, B. Brooks, and Y. Goldstein, “Disorder and the Optical Absorption Edge of Hydrogenated Amorphous Silicon,” *Le J. Phys. Colloq.*, vol. 42, no. C4, pp. C4-301-C4-304, 1981, doi: 10.1051/jphyscol:1981463.

[57] G. D. Cody, “The Optical Absorption Edge of a-Si: H,” in *Semiconductors and Semimetals*, Elsevier, 1984, pp. 11–82.

[58] M. Kranjčec, I. P. Studenyak, and M. V. Kurik, “On the Urbach rule in non-crystalline solids,” *J. Non. Cryst. Solids*, vol. 355, no. 1, pp. 54–57, 2009, doi: 10.1016/j.jnoncrysol.2008.03.051.

[59] A. Skumanich, A. Frova, and N. M. Amer, “Urbach tail and gap states in hydrogenated a-SiC and a-SiGe alloys,” *Solid State Commun.*, vol. 54, no. 7, pp. 597–601, 1985, doi: 10.1016/0038-1098(85)90086-9.

[60] I. P. Studenyak *et al.*, “Temperature and compositional behaviour of electrical conductivity and optical absorption edge in Cu7Ge(S1 - XSe x)5I mixed superionic crystals,” *Solid State Ionics*, vol. 181, no. 35–36, pp. 1596–1600, 2010, doi: 10.1016/j.ssi.2010.09.021.

[61] K. X. Steirer *et al.*, “Defect Tolerance in Methylammonium Lead Triiodide Perovskite,” *ACS Energy Lett.*, vol. 1, no. 2, pp. 360–366, 2016, doi:

10.1021/acsenergylett.6b00196.

[62] J. Kang and L. W. Wang, “High Defect Tolerance in Lead Halide Perovskite CsPbBr3,” *J. Phys. Chem. Lett.*, vol. 8, no. 2, pp. 489–493, 2017, doi: 10.1021/acs.jpclett.6b02800.

[63] K. Tvingstedt, K. Vandewal, A. Gadisa, F. Zhang, J. Manca, and O. Inganäs, “Electroluminescence from charge transfer states in polymer solar cells,” *J. Am. Chem. Soc.*, vol. 131, no. 33, pp. 11819–11824, 2009, doi: 10.1021/ja903100p.

[64] C. Wehrenfennig, M. Liu, H. J. Snaith, M. B. Johnston, and L. M. Herz, “Homogeneous emission line broadening in the organo lead halide perovskite CH3NH3PbI3- xClx,” *J. Phys. Chem. Lett.*, vol. 5, no. 8, pp. 1300–1306, 2014, doi: 10.1021/jz500434p.

[65] R. L. Milot, G. E. Eperon, H. J. Snaith, M. B. Johnston, and L. M. Herz, “Temperature-Dependent Charge-Carrier Dynamics in CH3NH3PbI3 Perovskite Thin Films,” *Adv. Funct. Mater.*, vol. 25, no. 39, pp. 6218–6227, 2015, doi: 10.1002/adfm.201502340.

[66] M. J. P. Alcocer, T. Leijtens, L. M. Herz, A. Petrozza, and H. J. Snaith, “Electron-Hole Diffusion Lengths Exceeding Trihalide Perovskite Absorber,” *Science (80-.).*, vol. 342, no. October, pp. 341–344, 2013, doi: 10.1126/science.1243982.

[67] Y. Bi, E. M. Hutter, Y. Fang, Q. Dong, J. Huang, and T. J. Savenije, “Charge Carrier Lifetimes Exceeding 15 μs in Methylammonium Lead Iodide Single Crystals,” *J. Phys. Chem. Lett.*, vol. 7, no. 5, pp. 923–928, 2016, doi: 10.1021/acs.jpclett.6b00269.

[68] L. M. Herz, “Charge-Carrier Dynamics in Organic-Inorganic Metal Halide Perovskites,” *Annu. Rev. Phys. Chem.*, vol. 67, pp. 65–89, 2016, doi: 10.1146/annurev-physchem-040215-112222.

[69] C. L. Davies *et al.*, “Bimolecular recombination in methylammonium lead triiodide perovskite is an inverse absorption process,” *Nat. Commun.*, vol. 9, no. 1, pp. 1–9, 2018, doi: 10.1038/s41467-017-02670-2.

[70] R. L. Milot, G. E. Eperon, T. Green, H. J. Snaith, M. B. Johnston, and L. M. Herz, “Radiative Monomolecular Recombination Boosts Amplified Spontaneous Emission in HC(NH2)2SnI3 Perovskite Films,” *J. Phys. Chem. Lett.*, vol. 7, no. 20, pp. 4178–4184, 2016, doi: 10.1021/acs.jpclett.6b02030.

[71] J. M. Richter *et al.*, “Enhancing photoluminescence yields in lead halide perovskites by photon recycling and light out-coupling,” *Nat. Commun.*, vol. 7, 2016, doi: 10.1038/ncomms13941.

[72] M. A. Green, “Improved value for the silicon free exciton binding energy,” *AIP Adv.*, vol. 3, no. 11, 2013, doi: 10.1063/1.4828730.

[73] S. Singh *et al.*, “Effect of Thermal and Structural Disorder on the Electronic Structure of Hybrid Perovskite Semiconductor CH3NH3PbI3,” *J. Phys. Chem. Lett.*, vol. 7, no. 15, pp. 3014–3021, 2016, doi: 10.1021/acs.jpclett.6b01207.

[74] F. Ruf *et al.*, “Temperature-dependent studies of exciton binding energy and phase-transition suppression in (Cs,FA,MA)Pb(I,Br)3 perovskites,” *APL Mater.*, vol. 7, no. 3, 2019, doi: 10.1063/1.5083792.

[75] S. Sun *et al.*, “The origin of high efficiency in low-temperature solution-processable bilayer organometal halide hybrid solar cells,” *Energy Environ. Sci.*, vol. 7, no. 1, pp.

399–407, 2014, doi: 10.1039/c3ee43161d.

[76] T. J. Savenije *et al.*, “Thermally activated exciton dissociation and recombination control the carrier dynamics in organometal halide perovskite,” *J. Phys. Chem. Lett.*, vol. 5, no. 13, pp. 2189–2194, 2014, doi: 10.1021/jz500858a.

[77] D. A. Valverde-Chávez *et al.*, “Intrinsic femtosecond charge generation dynamics in single crystal CH3NH3PbI3,” *Energy Environ. Sci.*, vol. 8, no. 12, pp. 3700–3707, 2015, doi: 10.1039/c5ee02503f.

[78] P. Piatkowski *et al.*, “Unraveling Charge Carriers Generation, Diffusion, and Recombination in Formamidinium Lead Triiodide Perovskite Polycrystalline Thin Film,” *J. Phys. Chem. Lett.*, vol. 7, no. 1, pp. 204–210, 2016, doi: 10.1021/acs.jpclett.5b02648.

[79] K. Tanaka, T. Takahashi, T. Ban, T. Kondo, K. Uchida, and N. Miura, “Comparative study on the excitons in lead-halide-based perovskite-type crystals CH3NH3PbBr3 CH3NH 3PbI3,” *Solid State Commun.*, vol. 127, no. 9–10, pp. 619–623, 2003, doi: 10.1016/S0038-1098(03)00566-0.

[80] M. Baranowski and P. Plochocka, “Excitons in Metal-Halide Perovskites,” *Adv. Energy Mater.*, vol. 10, no. 26, 2020, doi: 10.1002/aenm.201903659.

[81] R. J. Elliott, “Intensity of optical absorption by excitons,” *Phys. Rev.*, vol. 108, no. 6, pp. 1384–1389, 1957, doi: 10.1103/PhysRev.108.1384.

[82] K. Miyata, T. L. Atallah, and X. Y. Zhu, “Lead halide perovskites: Crystal-liquid duality, phonon glass electron crystals, and large polaron formation,” *Sci. Adv.*, vol. 3, no. 10, pp. 1–11, 2017, doi: 10.1126/sciadv.1701469.

[83] H. Zhu *et al.*, “Screening in crystalline liquids protects energetic carriers in hybrid perovskites,” *Science (80-.).*, vol. 353, no. 6306, pp. 1409–1413, 2016, doi: 10.1126/science.aaf9570.

[84] R. T. Williams, K. S. Song, W. L. Faust, and C. H. Leung, “Off-center self-trapped excitons and creation of lattice defects in alkali halide crystals,” *Phys. Rev. B*, vol. 33, no. 10, pp. 7232–7240, 1986, doi: 10.1103/PhysRevB.33.7232.

[85] L. R. V. Buizza and L. M. Herz, “Polarons and Charge Localization in Metal-Halide Semiconductors for Photovoltaic and Light-Emitting Devices,” *Adv. Mater.*, vol. 33, no. 24, pp. 1–19, 2021, doi: 10.1002/adma.202007057.

[86] بررسی فلور و پراکنش جغرافیایی گیاهان در ارتباط با اقلیم در مراتع“No Title, س .ن .ع .س .و .ح .بارانی ,منطقه ایرانشهر استان” vol. 148, pp. 148–162.

[87] B. Henderson and G. Francis Imbush, *Optical Spectroscopy of Inorganic Solids*. Oxford University Press, 2006.

[88] M. De Jong, L. Seijo, A. Meijerink, and F. T. Rabouw, “Resolving the ambiguity in the relation between Stokes shift and Huang-Rhys parameter,” *Phys. Chem. Chem. Phys.*, vol. 17, no. 26, pp. 16959–16969, 2015, doi: 10.1039/c5cp02093j.

[89] T. Leijtens, G. E. Eperon, N. K. Noel, S. N. Habisreutinger, A. Petrozza, and H. J. Snaith, “Stability of metal halide perovskite solar cells,” *Adv. Energy Mater.*, vol. 5, no. 20, pp. 1–23, 2015, doi: 10.1002/aenm.201500963.

[90] L. Meng, J. You, and Y. Yang, “Addressing the stability issue of perovskite solar cells for commercial applications,” *Nat. Commun.*, vol. 9, no. 1, pp. 1–4, 2018, doi:

10.1038/s41467-018-07255-1.

[91] W. Xiang, S. Liu, and W. Tress, “A review on the stability of inorganic metal halide perovskites: Challenges and opportunities for stable solar cells,” *Energy Environ. Sci.*, vol. 14, no. 4, pp. 2090–2113, 2021, doi: 10.1039/d1ee00157d.

[92] Y. Li, M. Dailey, P. J. Lohr, and A. D. Printz, “Performance and stability improvements in metal halide perovskite with intralayer incorporation of organic additives,” *J. Mater. Chem. A*, vol. 9, no. 30, pp. 16281–16338, 2021, doi: 10.1039/d1ta05252g.

[93] Y. Wu, D. Wang, J. Liu, and H. Cai, “Review of interface passivation of perovskite layer,” *Nanomaterials*, vol. 11, no. 3, pp. 1–19, 2021, doi: 10.3390/nano11030775.

[94] S. Rühle, “Tabulated values of the Shockley-Queisser limit for single junction solar cells,” *Sol. Energy*, vol. 130, pp. 139–147, 2016, doi: 10.1016/j.solener.2016.02.015.

[95] M. Green, *Third Generation Photovoltaics*. Springer Series in Photonics.

[96] P. Würfel, S. Finkbeiner, and E. Daub, “Generalized Planck’s radiation law for luminescence via indirect transitions,” *Appl. Phys. A Mater. Sci. Process.*, vol. 60, no. 1, pp. 67–70, 1995, doi: 10.1007/BF01577615.

[97] B. Ehrler, E. Alarcón-Lladó, S. W. Tabernig, T. Veeken, E. C. Garnett, and A. Polman, “Photovoltaics reaching for the shockley-queisser limit,” *ACS Energy Lett.*, vol. 5, no. 9, pp. 3029–3033, 2020, doi: 10.1021/acsenergylett.0c01790.

[98] U. Bach *et al.*, “Solid-State Dye-Sensitized Mesoporous TiO2 Solar Cells With High Photon-to-Electron Conversion Efficiencies,” *Nature*, vol. 395, 1998, doi: 10.1246/cl.1997.471.

[99] K. Murakoshi, R. Kogure, Y. Wada, and S. Yanagida, “Solid State Dye-Sensitized TiO 2 Solar Cell with Polypyrrole as Hole Transport Layer,” *Chem. Lett.*, vol. 26, no. 5, pp. 471–472, May 1997, doi: 10.1246/cl.1997.471.

[100] B. Podolsky *et al.*, “References and Notes 1.,” vol. 338, no. November, pp. 643–648, 2012.

[101] S. D. Stranks *et al.*, “Electron-Hole Diffusion Lengths Exceeding 1 Micrometer in an Organometal Trihalide Perovskite Absorber,” *Science (80-.).*, vol. 342, no. 6156, pp. 341–344, Oct. 2013, doi: 10.1126/science.1243982.

[102] P. Caprioglio *et al.*, “On the Relation between the Open-Circuit Voltage and Quasi-Fermi Level Splitting in Efficient Perovskite Solar Cells,” *Adv. Energy Mater.*, vol. 9, no. 33, p. 1901631, Sep. 2019, doi: 10.1002/aenm.201901631.

[103] “Solar Power Europe.” https://www.solarpowereurope.org/.

[104] A. Richter, M. Hermle, and S. W. Glunz, “Reassessment of the Limiting Efficiency for Crystalline Silicon Solar Cells,” *IEEE J. Photovoltaics*, vol. 3, no. 4, pp. 1184–1191, Oct. 2013, doi: 10.1109/JPHOTOV.2013.2270351.

[105] K. Yoshikawa *et al.*, “Silicon heterojunction solar cell with interdigitated back contacts for a photoconversion efficiency over 26%,” *Nat. Energy*, vol. 2, no. 5, 2017, doi: 10.1038/nenergy.2017.32.

[106] T. S. Sherkar *et al.*, “Recombination in Perovskite Solar Cells: Significance of Grain Boundaries, Interface Traps, and Defect Ions,” *ACS Energy Lett.*, vol. 2, no. 5, pp.

1214–1222, 2017, doi: 10.1021/acsenergylett.7b00236.

[107] J. M. Ball and A. Petrozza, “Defects in perovskite-halides and their effects in solar cells,” *Nat. Energy*, vol. 1, no. 11, 2016, doi: 10.1038/nenergy.2016.149.

[108] M. Wierzbowska, “Deprotonation and vacancies at the CH3NH3PbI3/ZnO and CH3NH3PbI3/GaN interfaces, detected in their theoretical XANES,” *J. Mater. Chem. C*, vol. 7, no. 18, pp. 5307–5313, 2019, doi: 10.1039/c9tc01152h.

[109] C. Pereyra, H. Xie, and M. Lira-Cantu, “Additive engineering for stable halide perovskite solar cells,” *J. Energy Chem.*, vol. 60, pp. 599–634, Sep. 2021, doi: 10.1016/j.jechem.2021.01.037.

[110] P. Billen *et al.*, “Comparative evaluation of lead emissions and toxicity potential in the life cycle of lead halide perovskite photovoltaics,” *Energy*, vol. 166, pp. 1089–1096, Jan. 2019, doi: 10.1016/j.energy.2018.10.141.

[111] S. E. Creutz, H. Liu, M. E. Kaiser, X. Li, and D. R. Gamelin, “Structural Diversity in Cesium Bismuth Halide Nanocrystals,” *Chem. Mater.*, vol. 31, no. 13, pp. 4685–4697, Jul. 2019, doi: 10.1021/acs.chemmater.9b00640.

[112] M. N. Tran, I. J. Cleveland, and E. S. Aydil, “Resolving the discrepancies in the reported optical absorption of low-dimensional non-toxic perovskites, Cs3Bi2Br9and Cs3BiBr6,” *J. Mater. Chem. C*, vol. 8, no. 30, pp. 10456–10463, 2020, doi: 10.1039/d0tc02783a.

[113] M. N. Tran, I. J. Cleveland, and E. S. Aydil, “Physical vapor deposition of the halide perovskite CsBi 2 Br 7,” *J. Vac. Sci. Technol. A*, vol. 39, no. 1, p. 013409, Jan. 2021, doi: 10.1116/6.0000604.

[114] Z. Jin, Z. Zhang, J. Xiu, H. Song, T. Gatti, and Z. He, “A critical review on bismuth and antimony halide based perovskites and their derivatives for photovoltaic applications: Recent advances and challenges,” *J. Mater. Chem. A*, vol. 8, no. 32, pp. 16166–16188, 2020, doi: 10.1039/d0ta05433j.

[115] X. Liu *et al.*, “Antimony-doping induced highly efficient warm-white emission in indium-based zero-dimensional perovskites,” *CCS Chem.*, vol. 2, no. 2, pp. 216–224, 2020, doi: 10.31635/ccschem.020.202000159.

[116] Y. He and G. Galli, “Perovskites for solar thermoelectric applications: A first principle study of CH3NH3AI3 (A = Pb and Sn),” *Chem. Mater.*, vol. 26, no. 18, pp. 5394–5400, 2014, doi: 10.1021/cm5026766.

[117] E. T. McClure, M. R. Ball, W. Windl, and P. M. Woodward, “Cs 2 AgBiX 6 (X = Br, Cl): New Visible Light Absorbing, Lead-Free Halide Perovskite Semiconductors,” *Chem. Mater.*, vol. 28, no. 5, pp. 1348–1354, Mar. 2016, doi: 10.1021/acs.chemmater.5b04231.

[118] O. Stroyuk, “Lead-free hybrid perovskites for photovoltaics,” *Beilstein J. Nanotechnol.*, vol. 9, pp. 2209–2235, Aug. 2018, doi: 10.3762/bjnano.9.207.

[119] G. Volonakis *et al.*, “Cs 2 InAgCl 6 : A New Lead-Free Halide Double Perovskite with Direct Band Gap,” *J. Phys. Chem. Lett.*, vol. 8, no. 4, pp. 772–778, Feb. 2017, doi: 10.1021/acs.jpclett.6b02682.

[120] D. Shi *et al.*, “Low trap-state density and long carrier diffusion in organolead trihalide perovskite single crystals,” *Science (80-.).*, vol. 347, no. 6221, pp. 519–522,

Jan. 2015, doi: 10.1126/science.aaa2725.

[121] "The reflection of X-rays by crystals," *Proc. R. Soc. London. Ser. A, Contain. Pap. a Math. Phys. Character*, vol. 88, no. 605, pp. 428–438, Jul. 1913, doi: 10.1098/rspa.1913.0040.

[122] J. Rodríguez-Carvajal, "Recent advances in magnetic structure determination by neutron powder diffraction," *Phys. B Condens. Matter*, vol. 192, no. 1–2, pp. 55–69, Oct. 1993, doi: 10.1016/0921-4526(93)90108-I.

[123] "ISIS Neutron and Muon Source." https://www.isis.stfc.ac.uk/Pages/home.aspx.

[124] N. K. Noel *et al.*, "Enhanced Photoluminescence and Solar Cell Performance via Lewis Base Passivation of Organic–Inorganic Lead Halide Perovskites," *ACS Nano*, vol. 8, no. 10, pp. 9815–9821, Oct. 2014, doi: 10.1021/nn5036476.

[125] G. Xing *et al.*, "Long-Range Balanced Electron- and Hole-Transport Lengths in Organic-Inorganic CH3NH3PbI3," *Science (80-.).*, vol. 342, no. 6156, pp. 344–347, Oct. 2013, doi: 10.1126/science.1243167.

[126] W. Li *et al.*, "Anomalous temperature-dependent photoluminescence peak energy in InAlN alloys," *J. Semicond.*, vol. 35, no. 9, p. 093001, Sep. 2014, doi: 10.1088/1674-4926/35/9/093001.

[127] D. W. de Quilettes *et al.*, "Impact of microstructure on local carrier lifetime in perovskite solar cells," *Science (80-.).*, vol. 348, no. 6235, pp. 683–686, May 2015, doi: 10.1126/science.aaa5333.

[128] C. P. Lindsey and G. D. Patterson, "Detailed comparison of the Williams–Watts and Cole–Davidson functions," *J. Chem. Phys.*, vol. 73, no. 7, pp. 3348–3357, Oct. 1980, doi: 10.1063/1.440530.

[129] G. Longo *et al.*, "Understanding the Performance-Limiting Factors of Cs 2 AgBiBr 6 Double-Perovskite Solar Cells," *ACS Energy Lett.*, vol. 5, no. 7, pp. 2200–2207, Jul. 2020, doi: 10.1021/acsenergylett.0c01020.

[130] J. C. de Mello, H. F. Wittmann, and R. H. Friend, "An improved experimental determination of external photoluminescence quantum efficiency," *Adv. Mater.*, vol. 9, no. 3, pp. 230–232, Mar. 1997, doi: 10.1002/adma.19970090308.

[131] T. Kirchartz and U. Rau, "Detailed balance and reciprocity in solar cells," *Phys. status solidi*, vol. 205, no. 12, pp. 2737–2751, Dec. 2008, doi: 10.1002/pssa.200880458.

[132] S. Mahesh *et al.*, "Revealing the origin of voltage loss in mixed-halide perovskite solar cells," *Energy Environ. Sci.*, vol. 13, no. 1, pp. 258–267, 2020, doi: 10.1039/C9EE02162K.

[133] T. Kirchartz and U. Rau, "Decreasing Radiative Recombination Coefficients via an Indirect Band Gap in Lead Halide Perovskites," *J. Phys. Chem. Lett.*, vol. 8, no. 6, pp. 1265–1271, Mar. 2017, doi: 10.1021/acs.jpclett.7b00236.

[134] G. E. Eperon *et al.*, "Inorganic caesium lead iodide perovskite solar cells," *J. Mater. Chem. A*, vol. 3, no. 39, pp. 19688–19695, 2015, doi: 10.1039/C5TA06398A.

[135] B. Park and S. Il Seok, "Intrinsic Instability of Inorganic–Organic Hybrid Halide Perovskite Materials," *Adv. Mater.*, vol. 31, no. 20, p. 1805337, May 2019, doi: 10.1002/adma.201805337.

[136] J. Yang, P. Zhang, and S.-H. Wei, “Band Structure Engineering of Cs 2 AgBiBr 6 Perovskite through Order–Disordered Transition: A First-Principle Study,” *J. Phys. Chem. Lett.*, vol. 9, no. 1, pp. 31–35, Jan. 2018, doi: 10.1021/acs.jpclett.7b02992.

[137] J. Feng, “Mechanical properties of hybrid organic-inorganic CH 3 NH 3 BX 3 (B = Sn, Pb; X = Br, I) perovskites for solar cell absorbers,” *APL Mater.*, vol. 2, no. 8, p. 081801, Aug. 2014, doi: 10.1063/1.4885256.

[138] H. Siethoff and K. Ahlborn, “Debye-temperature-elastic-constants relationship for materials with hexagonal and tetragonal symmetry,” *J. Appl. Phys.*, vol. 79, no. 6, pp. 2968–2974, 1996, doi: 10.1063/1.361293.

[139] M. A. Carpenter, E. K. H. Salje, and A. Graeme-Barber, “Spontaneous strain as a determinant of thermodynamic properties for phase transitions in minerals,” *Eur. J. Mineral.*, vol. 10, no. 4, pp. 621–691, Jul. 1998, doi: 10.1127/ejm/10/4/0621.

[140] “Coupling between the spontaneous strain and the order parameter,” in *Phase Transitions in Ferroelastic and Co-elastic Crystals*, Cambridge University Press, 1991, pp. 28–43.

[141] M. R. Filip, S. Hillman, A. A. Haghighirad, H. J. Snaith, and F. Giustino, “Band Gaps of the Lead-Free Halide Double Perovskites Cs2BiAgCl6 and Cs2BiAgBr6 from Theory and Experiment,” *J. Phys. Chem. Lett.*, vol. 7, no. 13, pp. 2579–2585, 2016, doi: 10.1021/acs.jpclett.6b01041.

[142] R. L. Z. Hoye *et al.*, “Fundamental Carrier Lifetime Exceeding 1 {\textmu}s in {Cs$_{2}$AgBiBr$_{6}$} Double Perovskite,” *Adv. Mater. Interfaces*, p. doi: 10.1002/admi.201800464, 2018, doi: 10.1002/admi.201800464.

[143] D. Bartesaghi *et al.*, “Charge Carrier Dynamics in Cs 2 AgBiBr 6 Double Perovskite,” *J. Phys. Chem. C*, vol. 122, no. 9, pp. 4809–4816, Mar. 2018, doi: 10.1021/acs.jpcc.8b00572.

[144] S. E. Creutz, E. N. Crites, M. C. De Siena, and D. R. Gamelin, “Colloidal Nanocrystals of Lead-Free Double-Perovskite (Elpasolite) Semiconductors: Synthesis and Anion Exchange To Access New Materials,” *Nano Lett.*, vol. 18, no. 2, pp. 1118–1123, Feb. 2018, doi: 10.1021/acs.nanolett.7b04659.

[145] C. C. Stoumpos, C. D. Malliakas, and M. G. Kanatzidis, “Semiconducting Tin and Lead Iodide Perovskites with Organic Cations: Phase Transitions, High Mobilities, and Near-Infrared Photoluminescent Properties,” *Inorg. Chem.*, vol. 52, no. 15, pp. 9019–9038, Aug. 2013, doi: 10.1021/ic401215x.

[146] C. C. Stoumpos and M. G. Kanatzidis, “The Renaissance of Halide Perovskites and Their Evolution as Emerging Semiconductors,” *Acc. Chem. Res.*, vol. 48, no. 10, pp. 2791–2802, Oct. 2015, doi: 10.1021/acs.accounts.5b00229.

[147] J. L. Knutson, J. D. Martin, and D. B. Mitzi, “Tuning the Band Gap in Hybrid Tin Iodide Perovskite Semiconductors Using Structural Templating,” *Inorg. Chem.*, vol. 44, no. 13, pp. 4699–4705, Jun. 2005, doi: 10.1021/ic050244q.

[148] J. A. Steele *et al.*, “Giant Electron–Phonon Coupling and Deep Conduction Band Resonance in Metal Halide Double Perovskite,” *ACS Nano*, vol. 12, no. 8, pp. 8081–8090, Aug. 2018, doi: 10.1021/acsnano.8b02936.

[149] V. D’Innocenzo *et al.*, “Excitons versus free charges in organo-lead tri-halide perovskites,” *Nat. Commun.*, vol. 5, pp. 1–6, 2014, doi: 10.1038/ncomms4586.

[150] I. Pelant and J. Valenta, *Luminescence Spectroscopy of Semiconductors*. Oxford University Press, 2012.

[151] H. Kanzaki, S. Sakuragi, and K. Sakamoto, “Excitons in AgBr1-æClæ - transition of relaxed state between free and self-traffed exciton,” *Solid State Commun.*, vol. 9, no. 13, pp. 999–1002, Jul. 1971, doi: 10.1016/0038-1098(71)90448-0.

[152] R. T. Williams and K. S. Song, “The self-trapped exciton,” *J. Phys. Chem. Solids*, vol. 51, no. 7, pp. 679–716, Jan. 1990, doi: 10.1016/0022-3697(90)90144-5.

[153] A. D. Wright *et al.*, “Ultrafast Excited-State Localization in Cs 2 AgBiBr 6 Double Perovskite,” *J. Phys. Chem. Lett.*, vol. 12, no. 13, pp. 3352–3360, Apr. 2021, doi: 10.1021/acs.jpclett.1c00653.

[154] X.-G. Zhao, D. Yang, J.-C. Ren, Y. Sun, Z. Xiao, and L. Zhang, “Rational Design of Halide Double Perovskites for Optoelectronic Applications,” *Joule*, vol. 2, no. 9, pp. 1662–1673, Sep. 2018, doi: 10.1016/j.joule.2018.06.017.

[155] Z. Xiao, W. Meng, J. Wang, D. B. Mitzi, and Y. Yan, “Searching for promising new perovskite-based photovoltaic absorbers: the importance of electronic dimensionality,” *Mater. Horizons*, vol. 4, no. 2, pp. 206–216, 2017, doi: 10.1039/C6MH00519E.

[156] L. R. V. Buizza and L. M. Herz, “Polarons and Charge Localization in Metal-Halide Semiconductors for Photovoltaic and Light-Emitting Devices,” *Adv. Mater.*, vol. 33, no. 24, p. 2007057, Jun. 2021, doi: 10.1002/adma.202007057.

[157] M.-H. Shang *et al.*, “Stable Bandgap-Tunable Hybrid Perovskites with Alloyed Pb–Ba Cations for High-Performance Photovoltaic Applications,” *J. Phys. Chem. Lett.*, vol. 10, no. 1, pp. 59–66, Jan. 2019, doi: 10.1021/acs.jpclett.8b03352.

[158] K. Du, W. Meng, X. Wang, Y. Yan, and D. B. Mitzi, “Bandgap Engineering of Lead-Free Double Perovskite Cs 2 AgBiBr 6 through Trivalent Metal Alloying,” *Angew. Chemie Int. Ed.*, vol. 56, no. 28, pp. 8158–8162, Jul. 2017, doi: 10.1002/anie.201703970.

[159] J. Luo *et al.*, “Efficient and stable emission of warm-white light from lead-free halide double perovskites,” *Nature*, vol. 563, no. 7732, pp. 541–545, Nov. 2018, doi: 10.1038/s41586-018-0691-0.

[160] B. Wruck, “Einfluβ des Na-Gehaltes und der A1, Si-Fehlordnung auf das thermodynamische Verhalten der Phasenumwandlung P1−15 in Anorthit,” University of Hannover, 1986.

[161] E. K. H. Salje, Ed., *Physical Properties and Thermodynamic Behaviour of Minerals*. Dordrecht: Springer Netherlands, 1988.

[162] M. C. Gallardo, F. J. Romero, S. A. Hayward, E. K. H. Salje, and J. del Cerro, “Phase transitions in perovskites near the tricritical point: an experimental study of KMn 1–x Ca x F 3 and SrTiO 3,” *Mineral. Mag.*, vol. 64, no. 6, pp. 971–982, Dec. 2000, doi: 10.1180/002646100549878.

[163] S. J. Zelewski *et al.*, “Revealing the nature of photoluminescence emission in the metal-halide double perovskite Cs2AgBiBr6,” *J. Mater. Chem. C*, vol. 7, no. 27, pp. 8350–8356, 2019, doi: 10.1039/c9tc02402f.

[164] A. Schmitz *et al.*, “Fine structure of the optical absorption resonance in Cs2AgBiBr6

double perovskite thin films," *ACS Energy Lett.*, vol. 5, no. 2, pp. 559–565, 2020, doi: 10.1021/acsenergylett.9b02781.

[165] R. Kentsch, M. Scholz, J. Horn, D. Schlettwein, K. Oum, and T. Lenzer, "Exciton Dynamics and Electron-Phonon Coupling Affect the Photovoltaic Performance of the Cs2AgBiBr6 Double Perovskite," *J. Phys. Chem. C*, vol. 122, no. 45, pp. 25940–25947, 2018, doi: 10.1021/acs.jpcc.8b09911.

[166] B. Yang *et al.*, "Lead-Free Silver-Bismuth Halide Double Perovskite Nanocrystals," *Angew. Chemie Int. Ed.*, vol. 57, no. 19, pp. 5359–5363, May 2018, doi: 10.1002/anie.201800660.

[167] B. A. Connor, L. Leppert, M. D. Smith, J. B. Neaton, and H. I. Karunadasa, "Layered halide double perovskites: Dimensional reduction of Cs2AgBiBr6," *J. Am. Chem. Soc.*, vol. 140, no. 15, pp. 5235–5240, 2018, doi: 10.1021/jacs.8b01543.

[168] Y. Bekenstein *et al.*, "The Making and Breaking of Lead-Free Double Perovskite Nanocrystals of Cesium Silver-Bismuth Halide Compositions," *Nano Lett.*, vol. 18, no. 6, pp. 3502–3508, 2018, doi: 10.1021/acs.nanolett.8b00560.

[169] S. De Wolf *et al.*, "Organometallic Halide Perovskites: Sharp Optical Absorption Edge and Its Relation to Photovoltaic Performance," *J. Phys. Chem. Lett.*, vol. 5, no. 6, pp. 1035–1039, Mar. 2014, doi: 10.1021/jz500279b.

[170] D. Luo *et al.*, "Enhanced photovoltage for inverted planar heterojunction perovskite solar cells," *Science (80-.).*, vol. 360, no. 6396, pp. 1442–1446, Jun. 2018, doi: 10.1126/science.aap9282.

[171] M. Abdi-Jalebi *et al.*, "Impact of Monovalent Cation Halide Additives on the Structural and Optoelectronic Properties of CH 3 NH 3 PbI 3 Perovskite," *Adv. Energy Mater.*, vol. 6, no. 10, p. 1502472, May 2016, doi: 10.1002/aenm.201502472.

[172] P. K. Nayak, S. Mahesh, H. J. Snaith, and D. Cahen, "Photovoltaic solar cell technologies: analysing the state of the art," *Nat. Rev. Mater.*, vol. 4, no. 4, pp. 269–285, Apr. 2019, doi: 10.1038/s41578-019-0097-0.

[173] J. F. Guillemoles, T. Kirchartz, D. Cahen, and U. Rau, "Guide for the perplexed to the Shockley–Queisser model for solar cells," *Nat. Photonics*, vol. 13, no. 8, pp. 501–505, 2019, doi: 10.1038/s41566-019-0479-2.

[174] X. Yang *et al.*, "Simultaneous Power Conversion Efficiency and Stability Enhancement of Cs 2 AgBiBr 6 Lead-Free Inorganic Perovskite Solar Cell through Adopting a Multifunctional Dye Interlayer," *Adv. Funct. Mater.*, vol. 30, no. 23, p. 2001557, Jun. 2020, doi: 10.1002/adfm.202001557.

[175] A. Onno, C. Chen, and Z. C. Holman, "Electron and hole partial specific resistances: a framework to understand contacts to solar cells," in *2019 IEEE 46th Photovoltaic Specialists Conference (PVSC)*, Jun. 2019, pp. 2329–2333, doi: 10.1109/PVSC40753.2019.8980762.

[176] V. M. Le Corre *et al.*, "Charge Transport Layers Limiting the Efficiency of Perovskite Solar Cells: How To Optimize Conductivity, Doping, and Thickness," *ACS Appl. Energy Mater.*, vol. 2, no. 9, pp. 6280–6287, Sep. 2019, doi: 10.1021/acsaem.9b00856.

[177] U. Rau, "Reciprocity relation between photovoltaic quantum efficiency and

electroluminescent emission of solar cells," *Phys. Rev. B*, vol. 76, no. 8, p. 085303, Aug. 2007, doi: 10.1103/PhysRevB.76.085303.

[178] S. Mahesh *et al.*, "Revealing the origin of voltage loss in mixed-halide perovskite solar cells," *Energy Environ. Sci.*, vol. 13, no. 1, pp. 258–267, 2020, doi: 10.1039/c9ee02162k.

[179] B. Zhao *et al.*, "High Open-Circuit Voltages in Tin-Rich Low-Bandgap Perovskite-Based Planar Heterojunction Photovoltaics," *Adv. Mater.*, vol. 29, no. 2, p. 1604744, Jan. 2017, doi: 10.1002/adma.201604744.

[180] E. Daub and P. Würfel, "Ultralow Values of the Absorption Coefficient of Si Obtained from Luminescence," *Phys. Rev. Lett.*, vol. 74, no. 6, pp. 1020–1023, Feb. 1995, doi: 10.1103/PhysRevLett.74.1020.

[181] P. Wurfel, "The chemical potential of radiation," *J. Phys. C Solid State Phys.*, vol. 15, no. 18, pp. 3967–3985, Jun. 1982, doi: 10.1088/0022-3719/15/18/012.

[182] D. W. deQuilettes *et al.*, "Maximizing the external radiative efficiency of hybrid perovskite solar cells," *Pure Appl. Chem.*, vol. 92, no. 5, pp. 697–706, May 2020, doi: 10.1515/pac-2019-0505.

[183] M. A. Green and A. W. Y. Ho-Baillie, "Pushing to the Limit: Radiative Efficiencies of Recent Mainstream and Emerging Solar Cells," *ACS Energy Lett.*, vol. 4, no. 7, pp. 1639–1644, Jul. 2019, doi: 10.1021/acsenergylett.9b01128.

[184] M. Abdi-Jalebi *et al.*, "Charge extraction via graded doping of hole transport layers gives highly luminescent and stable metal halide perovskite devices," *Sci. Adv.*, vol. 5, no. 2, p. eaav2012, Feb. 2019, doi: 10.1126/sciadv.aav2012.

[185] M. Chrzanowski, M. Kuchowicz, R. Szukiewicz, P. Sitarek, J. Misiewicz, and A. Podhorodecki, "Enhanced efficiency of quantum dot light-emitting diode by sol-gel derived Zn1-xMgxO electron transport layer," *Org. Electron.*, vol. 80, p. 105656, May 2020, doi: 10.1016/j.orgel.2020.105656.

[186] M. T. Hörantner *et al.*, "The Potential of Multijunction Perovskite Solar Cells," *ACS Energy Lett.*, vol. 2, no. 10, pp. 2506–2513, Oct. 2017, doi: 10.1021/acsenergylett.7b00647.